SEARCHING FOR $X(3872)$ ON THE LATTICE

by

Song-haeng Lee

A dissertation submitted to the faculty of
The University of Utah
in partial fulfillment of the requirements for the degree of

Doctor of Philosophy

in

Physics

Department of Physics and Astronomy

The University of Utah

August 2016

The University of Utah Graduate School

STATEMENT OF DISSERTATION APPROVAL

The dissertation of Song-haeng Lee
has been approved by the following supervisory committee members:

Carleton DeTar , Chair	4/29/2016
	Date Approved
Douglas Bergman , Member	5/2/2016
	Date Approved
Eugene Mishchenko , Member	4/29/2016
	Date Approved
Pearl Sandick , Member	5/5/2016
	Date Approved
Robert Michael Kirby II , Member	5/3/2016
	Date Approved

and by Carleton DeTar, Chair of The Department of Physics and Astronomy and by David B. Kieda, Dean of The Graduate School.

ABSTRACT

The purpose of this dissertation is to provide high-precision lattice quantum chromodynamics (QCD) simulation results for the mass splittings of low-lying charmonium states as the test of the Standard Model, and, further, to study the nature of a higher mass charmonium-like state called $X(3872)$. Since the discovery of charmonium, it has played an important role in the study of QCD. However, it had been impossible to study charmonium energy levels at a low energy regime in QCD perturbative theory due to color confinement, which is the consequence of the SU(3) nonabelian gauge theory in QCD. From this point of view, numerical simulation with lattice QCD is a unique method that provides a nonperturbative, *ab initio* approach for studying hadronic states governed by the strong interactions. In this dissertation, I describe a high-precision study of the splittings of the low-lying charmonium states, particularly the $1S$ and $1P$ states, including a chiral-continuum extrapolation. The highly excited charmonium states, discovered in the past decade, are much more challenging to study because their energy levels lie near or above the $D^0\bar{D}^0$ threshold, so they cannot be explained within the conventional quark model. Among those, we are interested in the narrow charmonium-like state, $X(3872)$, due to its closeness to the $D\bar{D}^*$ threshold and its possible four-quark nature. Since the $X(3872)$ mass is within 1 MeV of the $D\bar{D}^*$ threshold, it is a strong candidate for a $D\bar{D}^*$ molecular state. Therefore, we use interpolating operators including both the conventional, excited P-wave charmonium state, χ_{c1}, and the $D\bar{D}^*$ open charm state for the isospin 0 channel. I provide the theoretical background for the lattice calculation and the corresponding methodologies, report on our high-precision results for the mass splittings of low-lying charmonium states, I introduce a new methodology called the "staggered variational method", which is a variational method applied to the staggered fermion formalism, and finally, I present the simulation results for the $X(3872)$ with quantum numbers $J^{\mathrm{PC}} = 1^{++}$ and isospin 0, using lattice QCD, as well as the detailed analysis and our interpretation to reveal the physical nature of $X(3872)$.

"Nature is trying very hard to make us succeed, but nature does not depend on us. We are not the only experiment."

– R. Buckminster Fuller

CONTENTS

LIST OF FIGURES

LIST OF TABLES

ACKNOWLEDGMENTS

I thank my advisor, Carleton DeTar. Also I thank Daniel Mohler and Heechang Na for useful discussions, and my colleagues in the Fermilab Lattice and MILC collaborations. This work was supported by the U.S. National Science Foundation under grant NSF PHY10-034278 and the U.S. Department of Energy under grant DE-FC02-12ER41879. Computations were carried out on the LQCD clusters at Fermilab, the National Energy Resources Supercomputing Center (NERSC), the Texas Advanced Computing Center (TACC), and at the Utah Center for High Performance Computing.

CHAPTER 1

INTRODUCTION

The standard model (SM) of particle physics is a field theoretical description of the elementary particles and their interactions. Essentially all results of particle physics experiments have been well explained within the SM up to energy scales of 1 TeV. The exceptions, although tantalizing, are not strong enough to suggest revisions. In the standard model, elementary particles are divided into fermions and gauge bosons, and there are four types of fundamental interactions – gravitational, electromagnetic, weak, and strong. The quarks (fermions) interact through the strong interactions as a consequence of their color-charge together with the gluons, which are the gauge bosons mediating strong forces. The name "strong interactions" is due to their greater strength compared with other interactions, *e.g.,* the electroweak interaction. The strength of the strong force is governed by the size of strong coupling constant α_S (analogous to the hyperfine constant α in electromagnetic interaction). It varies from large to low values, namely $\alpha_S \approx 1$ at scales of order one fermi and decreases to zero at very short distances. This property allows one to use perturbation theory for hard processes that probe short distances (momentum transfer $Q \to \infty$). On the other hand, in the regime $Q \to m_{\rm hadron}$ where α_S becomes of order unity, the perturbative method fails.

Charmonium is a meson consisting of a charm and an anti-charm quark pair. Charmonium spectroscopy is a good probe of QCD hadronic physics. Early calculations based on the nonrelativistic potential model have been fairly successful in predicting the charmonium spectrum by treating the charmonium system as a bound state of a charm and anti-charm quark pair. However, in this approach, there are two clear limitations. First, as mentioned above, in the low energy regime, the potential in the nonrelativistic quark model is *ad hoc* and v/c is not so small so relativistic corrections are needed. Second, above the open-charm threshold, where the energy level is higher than $M(D) + M(\overline{D})$, [1] the states cannot be

[1] D is a meson containing a charm quark and an anti-up quark. $\overline{D}$ is the anti-meson of D.

explained by the conventional quark model. Two examples of such unexpected states are the $X(3872)$ and $Z_c^{\pm}(3900)$, which have been confirmed by many experiments. The mass of the $X(3872)$ is very closed to the $D\bar{D}^*$ threshold. Although many theoretical models have been suggested, such as a hybrid meson, in which a gluon is excited, a hadronic molecular state, in which two mesons form a bound state, and so on, its nature of structure still remains unclear. Another state $Z_c^{\pm}(3900)$ is a charged charmonium state which obviously must contain at least four quark components, so it would be a tetraquark or molecular state, which is not the conventional quark state. In other words, the hadronic states described above cannot be directly studied by perturbative QCD in such a low energy regime where the interaction of the colored quarks and gluons is very strong.

A crucial test of understanding QCD is to make a precise accounting of the hadron spectrum as measured in experiment, regardless of the energy regime. From this point of view, lattice QCD is the preferred choice of method. Numerical simulation with lattice QCD uses a lattice version of quantum chromodynamics, which is a nonperturbative *ab initio* method, and capable of giving accurate predictions of QCD, *e.g.,* the mechanism for confinement, chiral symmetry breaking, and the equilibrium properties of QCD at finite temperature.

The purpose of this dissertation is to present our lattice-QCD simulation results of the various charmonium states, namely the low-lying charmonium spectrum and the $X(3872)$. Our calculations are model-independent, nonperturbative and based on first principles. I also provide a new lattice method for extracting highly excited hadron energies from the lattice. This dissertation is organized as follows: In Chapter 2, I give some background about the standard model of particle physics. In Chapter 3, I give an introduction to lattice gauge theory. In Chapter 4, I briefly give an idea how the nonrelativistic method works to study the charmonium spectrum and discuss its limitations. Next, I describe the lattice methodology and report on simulation result for the low-lying charmonium spectrum on the lattice. These results were obtained in collaboration with Fermilab Lattice and MILC collaborations. In Chapter 5, I introduce a new methodology called "staggered variational method" and the corresponding simulation results of the D_s spectrum. In Chapter 6, I give a brief introduction to the $X(3872)$ state. This state is usually considered to be a multiquark state containing at least four quarks - two charm and two light quarks. I give a brief summary of the experimental status and theoretical description of the state. Finally, I present our analysis of the simulation results and report the result of $X(3872)$ simulation.

CHAPTER 2

STANDARD MODEL

In this chapter, I give a brief description of the standard model with an introduction to the gauge theories of quantum electrodynamics and quantum chromodynamics. Concerning quantum chromodynamics, first, I introduce the "quark model" proposed by Gell-Mann [13] and Zweig [14] in 1963 to explain the spectrum of strongly interacting particles phenomenologically. Next, I describe why quantum chromodynamics had to be formulated, despite the phenomenological success of the quark model. Finally, I give an introduction to quantum chromodynamics.

2.1 Introduction

The standard model (SM) [15] of particle physics is the theoretical framework describing the matter constituents in nature and their interactions at the $10^{-15} \sim 10^{-19}$ m scale. All known elementary particles and their interactions can be well described within the SM. In the SM, there are two types of elementary particles – one, called "fermion", carries half-integer spin and is governed by Fermi-Dirac statistics, and the other, "boson", carries integer spin and is governed by Bose-Einstein statistics.

Fermions can be divided into two families according to their interaction types - quarks and leptons. Each family can be further grouped into three generations according to their masses. The quarks are of six different flavors, grouped into three generations as (up, down), (charm, strange) and (top, bottom). The generations for the leptons are (electron, electron neutrino), (muon, muon neutrino) and (tau, tau neutrino). See Fig. 2.1 for a graphical representation and their abbreviations.

On the other hand, bosons, or gauge bosons, can be classified by the force types they are carrying. In nature, there are four types of fundamental forces - gravitational, electromagnetic, weak, and the strong forces. Their corresponding carriers are the graviton, the photon, the weak bosons, and the gluons, respectively. However in the SM, the

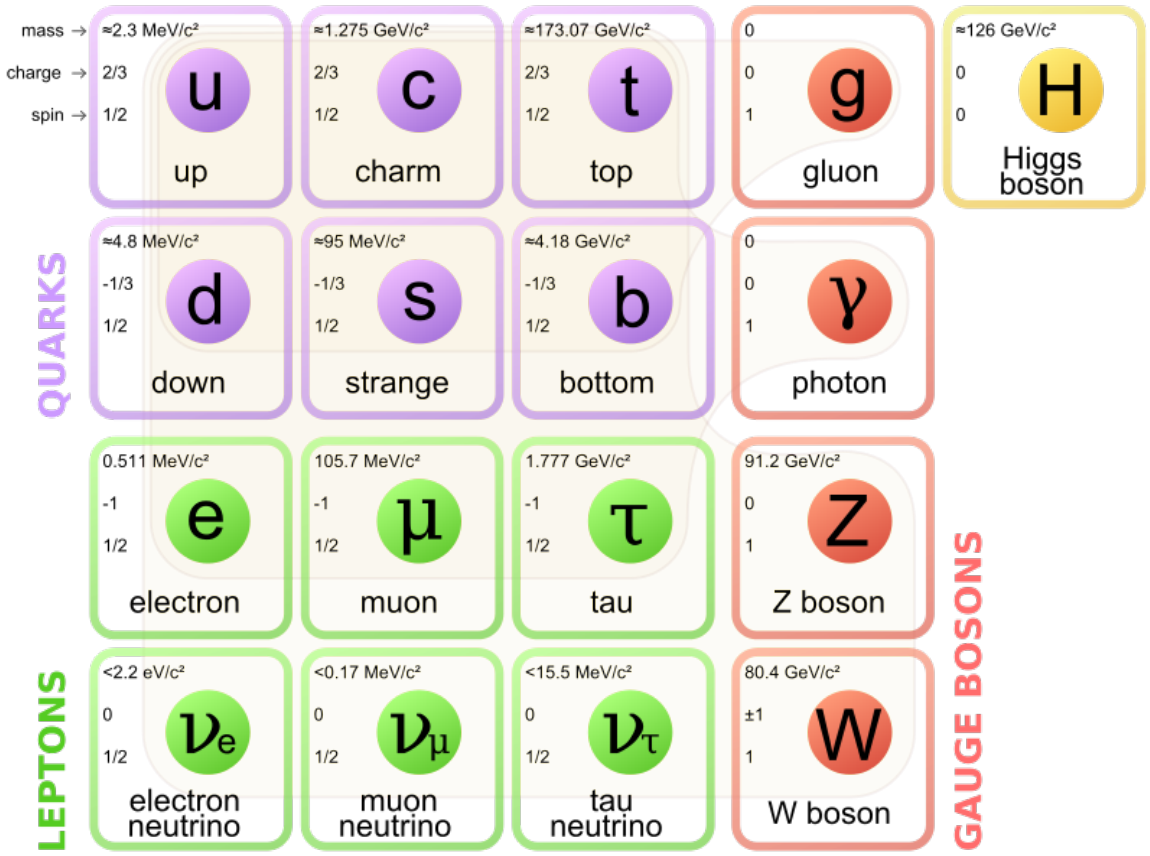

Figure 2.1. Elementary particles in the standard model [1]. The figure lists 12 fermions, 4 gauge bosons, and the Higgs boson. Fermions can be divided into two types - quarks and leptons. Each has 6 different flavors.

gravitational force, so also the graviton, is excluded, because it is too weak to be observed at the quantum level scale, and we do not know how to quantize gravity.

The quarks have fractional electric charges and interact through strong, electromagnetic, and weak forces. They have charge $Q = \frac{2}{3}$ for up-quark, $-\frac{1}{3}$ for down-quark, $-\frac{1}{3}$ for strange-quark, $\frac{2}{3}$ for charm-quark, $-\frac{1}{3}$ for bottom-quark, and $\frac{2}{3}$ for top-quark, in the units of the electron's charge e, respectively. In addition, quarks carry an additional degree of freedom called color. Color charges affect how quarks interact with gluons through the strong force. QCD (quantum chromodynamics) is the theory that describes strong interactions of quarks and gluons.

On the other hand, the leptons are the electron, e^-, the muon, μ^-, and the τ^- with electric charge $Q = -1$, in units of the elementary charge e. There are corresponding neutral, $Q = 0$, neutrinos, ν_e, ν_μ, and ν_τ. These leptons interact with other fermions through the electromagnetic and weak forces.

The second type of particle, the bosons, have spin $s = 1$. The photon, γ, is the particle exchanged in the electromagnetic interactions. Eight gluons g_α, $\alpha = 1, ...8$ mediate the strong interactions between quarks, and finally, the three weak bosons, $W^\pm, Z$, are the intermediate bosons of the weak interactions.

Concerning the range of the three types of interactions, first, the range of electromagnetic interactions is infinite as it corresponds to an interaction mediated by a massless gauge boson, γ. On the other extreme, the weak interactions have an interaction range about 10^{-18} m corresponding to the exchange of a massive gauge particle, $W^\pm$ or Z, with a mass of the order of $M_V \approx 100$ GeV/c^2. Finally, the strong interaction range is not infinite although the intermediate particle gluon, g_α, is massless. In fact, QCD does not allow the quarks to be free. Instead, the strong force between two quarks stays constant as the distance between them increases. This is the consequence of the nonabelian gauge theory describing the $SU(3)$ color forces. Unlike $U(1)$ gauge theory with uncharged photons, the gluons carry color charges so they can interact with themselves. This results in so-called anti-screening. In other words, at large inter-quark distances, it becomes energetically favorable for a new quark-antiquark pair to be created out of the vacuum, rather than allowing the distance between the quarks to grow. The effective range of pair creation via the strong interaction is about 10^{-15} m. Thus, all observed hadrons consist of two or more quarks in a color-neutral configuration, not as free quarks. These colorless composite particles are classified into baryons and mesons, or combinations thereof. For example, the baryons are fermions made of three quarks, qqq, and the mesons, bosons made of a quark-antiquark pair, $q\bar{q}$.

As for the strength of the three interactions, the electromagnetic interactions are governed by the size of the electromagnetic coupling constant e or equivalently the hyperfine structure constant $\alpha = e^2/4\pi$. The weak interactions have an effective weak strength given by the dimensionful Fermi constant $G_F = 1.167 \times 10^{-5}$ GeV^{-2}, so they are weak at energies much less than 100 GeV and comparable to the electromagnetic interaction at higher energies. Finally, as the name suggests, the strong interaction is comparatively stronger than the others. It is governed by the size of the strong coupling constant g_S or equivalently $\alpha_S = g_s^2/4\pi$, varying from ≈ 1 at low energy to ≈ 0 at high energy.

In the following sections, we will briefly discuss these elementary particles and their interactions via group and gauge theory.

2.2 Symmetries in particle physics

One can classify the symmetry in physics in two ways, *discrete symmetries* and *continuous symmetries* [16]. Discrete symmetries are characterized by a finite symmetry group. The

most relevant symmetries are transformations of parity (P), charge conjugation (C), and time reversal (T). The CPT theorem states that all interactions must be invariant under the total transformation given by the product of C, P, and T, regardless of their order. The electromagnetic and strong interactions are invariant under the separate transformation P, C, and T, whereas the weak interactions can violate, P, C, and PC.

Continuous symmetries can be further classified by two types - *space-time symmetries* and *internal symmetries*. Space-time symmetries act on the space-time coordinates; they are translations, rotations, and boosts. Such transformations are called the Poincaré transformations. All interactions are invariant under the Poincaré transformations.

On the other hand, the internal symmetries act on the internal quantum numbers. These symmetries can be further classified in two distinct classes. One type are *global symmetries*, in which the continuous parameters of the transformation do not depend on the space-time coordinate, such as $SU(2)$ isospin symmetry, $SU(3)$ flavor symmetry, etc. The other type are *local gauge symmetries* in which the continuous parameters of the transformation depend on the space-time coordinates. For example, the $U(1)$ local gauge transformation in electromagnetism can be performed as

$$\psi(x) \to e^{i\theta(x)}\psi(x)\,, \qquad A_\mu(x) \to A_\mu(x) + e^{-1}\partial_\mu\theta(x)\,, \tag{2.1}$$

where $\psi(x)$ is a Dirac field, $A_\mu(x)$ is a gauge field for electromagnetism, and e is the electric charge for ψ. The phase θ depends on the space-time point $x \equiv x_\mu$, and has one associated gauge boson field, $A_\mu(x)$.

These gauge symmetries are very important features of particle physics and play a crucial role in the building of the SM. The quantum field theories that are based on the existence of some gauge symmetry are called gauge theories. The gauge theory based on $U(1)_{\rm em}$ is quantum electrodynamics (QED), $SU(3)_C$, quantum chromodynamics (QCD), and $SU(2)_L \times U(1)_Y$, electroweak theory. The SM is the gauge theory based on the total gauge symmetry of the fundamental interactions in particle physics, $SU(3)_C \times SU(2)_L \times U(1)_Y$.

2.3 Quantum electrodynamics (QED)

QED is the most successful gauge theory in particle physics and has been tested up to a high level of precision [17]. One starts by considering a spin-1/2, mass m, a fermion of charge e represented by a field $\psi(x)$, and a gauge field $A_\mu(x)$. The QED Lagrangian, which is invariant under a $U(1)$ local gauge transformation, Eq. (2.1), is

$$\mathcal{L}_{\rm QED} = \bar{\psi}(i\not{D} - m)\psi - \frac{1}{4}F^2\,, \tag{2.2}$$

where $\not{D} \equiv \gamma_\mu D^\mu$, and D is the gauge-covariant derivative defined through $D_\mu\psi = (\partial_\mu + ieA_\mu)\psi$. $F^2 \equiv F^{\mu\nu}F_{\mu\nu}$ and $F_{\mu\nu}$ is the field strength tensor,

$$F_{\mu\nu} = \partial_\mu A_\nu - \partial_\nu A_\mu \,, \tag{2.3}$$

which is also gauge invariant.

Note that the Euler-Lagrange equation of motion for a field ϕ in a given Lagrangian $\mathcal{L}$ is

$$\partial_\mu \left(\frac{\partial \mathcal{L}}{\partial(\partial_\mu \phi)} \right) - \frac{\partial \mathcal{L}}{\partial \phi} = 0 \,. \tag{2.4}$$

The equation of motion for ψ and A_μ reduce to the Dirac and Maxwell equations,

$$(i\not{D} - m)\psi(x) \;=\; 0 \,, \tag{2.5}$$

$$\partial_\mu F^{\mu\nu} \;=\; e\bar{\psi}\gamma^\nu\psi \;=\; ej^\nu \,, \tag{2.6}$$

respectively.

2.4 Quantum chromodynamics (QCD)

The critical difference between QCD and QED is the phenomenon of asymptotic freedom [18, 19], briefly introduced in Chap. 1. In this section, first, I discuss the quark model and introduce the additional quantum number called "color". Next, I give a brief introduction to QCD.

2.4.1 Quark model

In 1963, Gell-Mann [13] and Zweig [14] proposed a "quark model" that explains the spectrum of hadrons in terms of quarks. According to the quark model, all hadrons are made up of quarks, bound together in different ways. Each quark is assigned spin $\frac{1}{2}$ and baryon number, $B = \frac{1}{3}$. The mesons are composed of a quark-antiquark pair ($q\bar{q}$) and baryons, three quarks (qqq).

One of the important features of the quark model is that it incorporates the symmetry of the strong interactions between quarks based on their masses. If one assumes that u and d have the same masses and interactions, then the following $SU(2)$ group with the unitary transformation matrix U,

$$\begin{pmatrix} u \\ d \end{pmatrix} \longrightarrow U \begin{pmatrix} u \\ d \end{pmatrix} \,, \tag{2.7}$$

must be a symmetry group of the strong interactions. In fact, the quantum number associated with the $SU(2)$ symmetry is called "isospin" and often represented by T. Similarly, because the strange quark, s, has mass fairly close to u and d, one can extend the

$SU(2)$ multiplet to the $SU(3)$ flavor symmetry group multiplet (u, d, s). This requires one additional quantum number, the strangeness, S, which is 0 for u and d, and -1 for s quarks. Or else, one can define an additional quantum number that coincides with the center of charge of a multiplet, called "hypercharge", Y, [13, 20]

$$Y \equiv Q_{min} + Q_{max} = B + S\,. \tag{2.8}$$

The basic quark multiplet is shown in Figs. 2.2 (A) and (B). Within an $SU(3)$ multiplet, one can classify mesons and baryons in $T_3 - Y$ plane. Since the mesons appear as composite states of a $q\bar{q}$, we can represent its flavor content as

$$q\bar{q} = 3 \otimes \bar{3} = 1 \oplus 8 \tag{2.9}$$

where the 1 is the $SU(3)$ meson singlet. It is the $\eta' \sim (u\bar{u} + d\bar{d} + s\bar{s})$ for $J^P = 0^-$, where J is total angular momentum and P is the parity quantum number. The 8 is the $SU(3)$ meson octet. For example, for 0^- mesons, they are $\pi^+ \sim u\bar{d}$, $K^+ \sim u\bar{s}$ ... and so on. On the other hand, the baryon is made up of qqq, so we can decompose it as

$$qqq = 3 \otimes 3 \otimes 3 = 1 \oplus 8 \oplus 8 \oplus 10\,, \tag{2.10}$$

where the 1 is the $SU(3)$ baryon singlet. It is the $\Lambda(1115)$. The 8 is the $SU(3)$ baryon octet. For the $\frac{1}{2}^+$ baryons, they are $n \sim udd$, $p \sim uud$ ... and so on (see Fig 2.2 (D)). The decuplet 10 contains the $\frac{3}{2}^+$ baryons (not shown in the figure), $N^{*+} \sim uud$, $\Sigma^{*+} \sim suu$,... and so on.

Now, analogous to the extension from the $SU(2)$ to the $SU(3)$ multiplets, we can extend further by including the charm quark, c, and introduce an additional quantum number, called "charm" so that charm quark has $C = 1$, $T = 0$ and $Y = \frac{1}{3}$. Fig. 2.3 shows the $SU(4)$ multiplets. Note that the two mesons located at the singlets in Fig. 2.3 (A) and (B), respectively, labeled by η_c and J/ψ are called charmonium whose quark constituents are $c\bar{c}$.

Despite the success of the original quark model to predict new hadrons, it has critical contradictions. First, no free particle with fractional charge has been found. Second, the total wave function of baryons must be symmetric under the interchange of the quark spin and flavor quantum number, which contradicts Fermi-Dirac statistics. For example, consider the Δ^{++} particles whose quark components are (u, u, u), shown in Fig. 2.3 (D). For the spin quadruplet states ($S = 3/2$), all four states are symmetric under the interchange of any two quarks. Thus, for the spin quadruplet states having zero orbital angular momentum, their total wave function becomes symmetric, which contradicts Fermi-Dirac statistics.

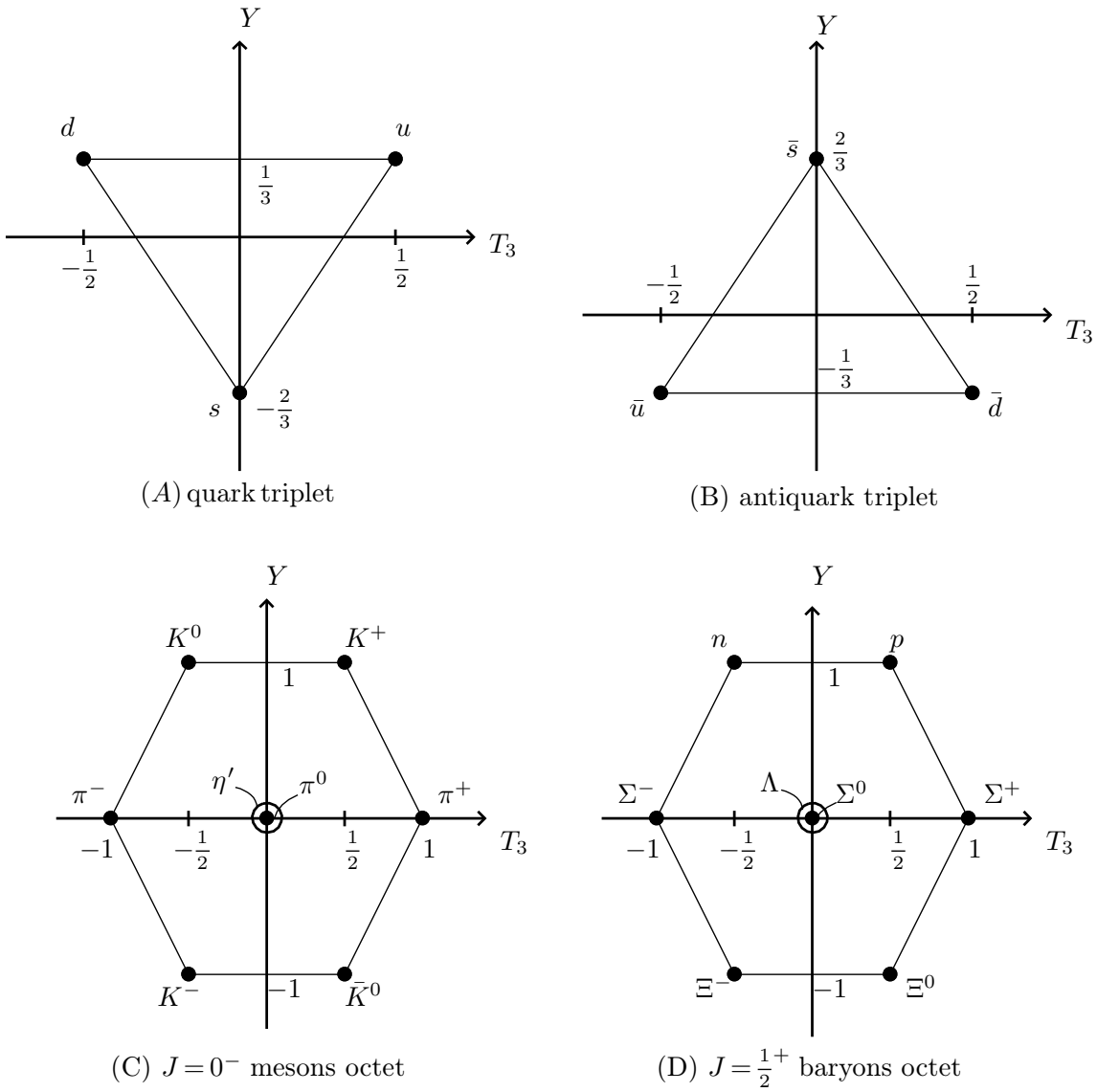

Figure 2.2. Examples of $SU(3)$ flavor multiplets as a function of hypercharge Y and the isospin component T_3. Panel (A) and (B) show the smallest nontrivial representation of SU(3) made out of u, d, and s quarks, and panels (C) and (D), respectively, show pseudoscalar meson and baryon octets,

These contradictions are avoided with an additional quantum number called "color" so that the baryon wave function is totally antisymmetric in the color quantum number. Because color symmetry has no other obvious physical role, it is natural for color symmetry to be classified as the gauge group. Thus, if we set the quark to q^c where $c = 1, 2, 3$ is color index, the quarks transform under the **3** representation of the color $SU(3)$ symmetry, whereas the antiquark transform under the $\bar{\mathbf{3}}$. The corresponding quanta of the $SU(3)$ gauge

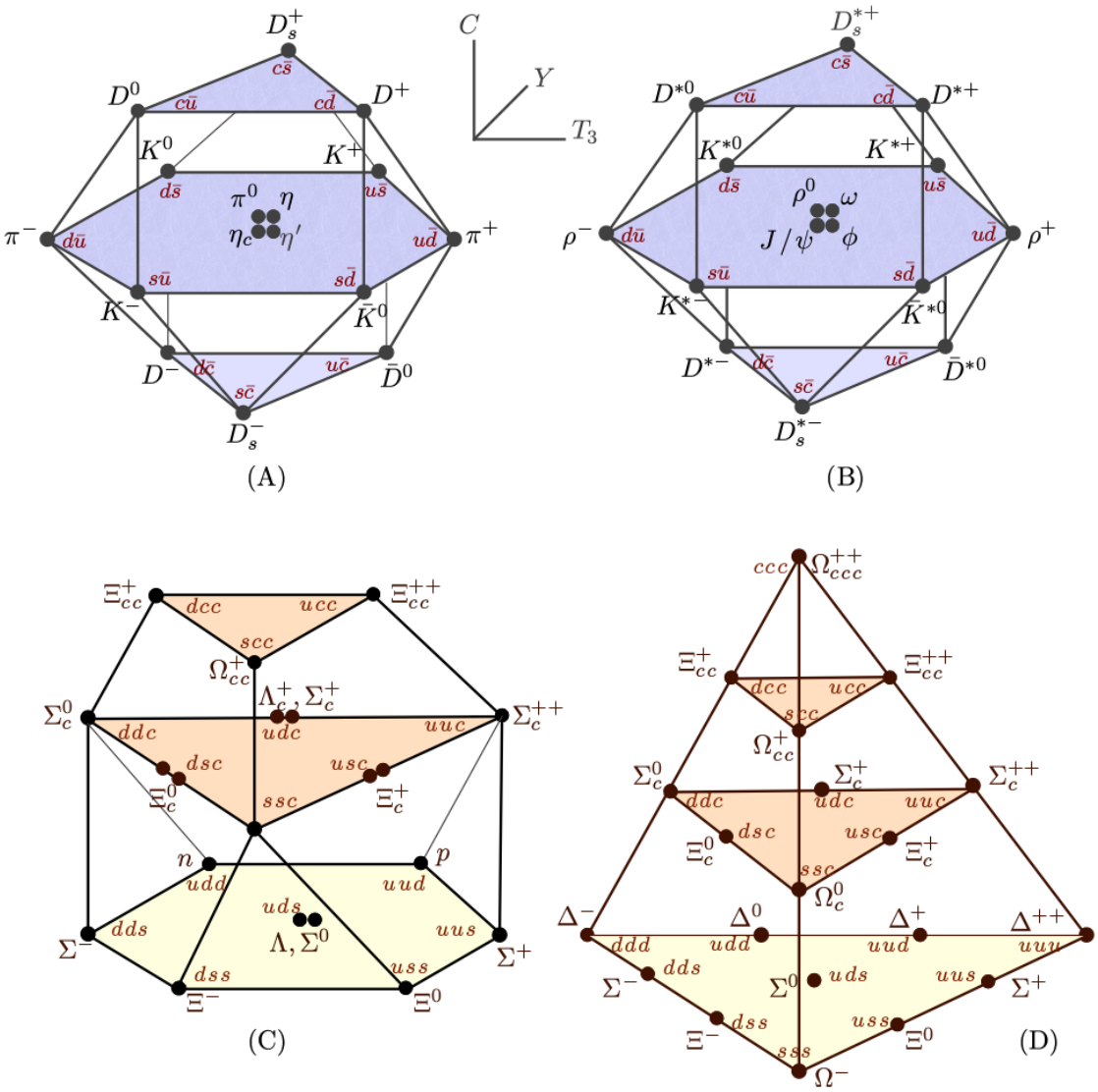

Figure 2.3. Examples $SU(4)$ multiplets made out of u, d, s, and c quarks. Panels (A) and (B), respectively, show the pseudoscalar and vector mesons 16-plets, and panels (C) and (D) show the 20-plet, as a function of hypercharge Y, isospin component T_3, and charm C.

field are gluons. In addition, all hadrons must be singlets under the color symmetries. Now, the required antisymmetrization of baryon and anti-baryon wavefunctions can be done by using the Levi-Civita symbol, ϵ_{abc},

$$\epsilon_{abc} q^a q^b q^c \,, \qquad \epsilon_{abc} \bar{q}^a \bar{q}^b \bar{q}^c \,. \tag{2.11}$$

On the other hand, because a meson consists of a pair of quark-antiquark, one can simply write it as

$$\bar{q}_c q^c \,, \tag{2.12}$$

where both baryons and mesons appear as color-singlet.

2.4.2 QCD Lagrangian

In the previous subsection, I have discussed the representations of quark fields and introduced an additional quantum number, color. In this subsection, I will discuss the Lagrangian which is invariant under the color $SU(3)$ transformations.

Quantum chromodynamics is an $SU(3)$ nonabelian gauge theory of the color charge (g_S) [17]. The fermions, which carry color charge, are the quarks, each with field $\psi_c^f \equiv \{[\psi_c^f]_\alpha\}$, where $f = u, d, s, ...$ is the flavor label, $c = 1, 2, 3$ is the color index, and we suppress the Dirac-spinor indices $\alpha = 1, 2, 3, 4$. The gauge bosons, also carrying color, are the gluons, with field $A_\mu^a, a = 1, ..., 8$. One can write the Lagrangian L_{QCD} as

$$\mathcal{L}_{\rm QCD} = \sum_f \bar{\psi}_{c_1}^f (i\not{D}_{c_1 c_2} - m^f \delta_{c_1 c_2})\psi_{c_2}^f - \frac{1}{4} F_a^{\mu\nu} F_{\mu\nu}^a \,, \tag{2.13}$$

where $\not{D} \equiv \gamma_\mu D^\mu$, and $F_{\mu\nu}^a$ is the color field strength tensor,

$$F_{\mu\nu}^a = \partial_\mu A_\nu^a - \partial_\nu A_\mu^a - g_S f^{abc} A_\mu^b A_\nu^c \,. \tag{2.14}$$

Note that we suppress the color indices c_i. $F_{\mu\nu}^a$ contains a bilinear term in the gluon fields, as it corresponds to a nonabelian gauge theory with structure constants $f^{abc}(a, b, c = 1, ..., 8)$. The quark covariant derivative is

$$D_\mu \psi = \left(\partial_\mu + i g_S \frac{\lambda_a}{2} A_\mu^a\right) \psi \,, \tag{2.15}$$

With $SU(3)$ generators, $\lambda^a/2$, and the rotation parameters, θ^a, the local $SU(3)$ transformations of the color degree of freedom for the quark and gluon fields are given by

$$\psi(x) \to U(\theta)\psi(x) = \exp(-i\theta^a \frac{\lambda^a}{2})\psi(x) \,, \tag{2.16}$$

$$A_\mu^a \to A_\mu^a - \frac{1}{g_S}\partial_\mu \theta^a + f^{abc}\theta^b A_\mu^c \,, \tag{2.17}$$

respectively. The generators, $\lambda^a/2$, are 3×3 traceless, hermitian matrices and are given in terms of Gell-Mann matrices,

$$\lambda_1 = \begin{pmatrix} 0 & 1 & 0 \\ 1 & 0 & 0 \\ 0 & 0 & 0 \end{pmatrix} \quad , \quad \lambda_2 = \begin{pmatrix} 0 & -i & 0 \\ i & 0 & 0 \\ 0 & 0 & 0 \end{pmatrix} \quad , \quad \lambda_3 = \begin{pmatrix} 0 & -i & 0 \\ i & 0 & 0 \\ 0 & 0 & 0 \end{pmatrix}$$

$$\lambda_4 = \begin{pmatrix} 0 & 0 & 1 \\ 0 & 0 & 0 \\ 1 & 0 & 0 \end{pmatrix} \quad , \quad \lambda_5 = \begin{pmatrix} 0 & 0 & -i \\ 0 & 0 & 0 \\ i & 0 & 0 \end{pmatrix}$$

$$\lambda_6 = \begin{pmatrix} 0 & 0 & 0 \\ 0 & 0 & 1 \\ 0 & 1 & 0 \end{pmatrix} \quad , \quad \lambda_7 = \begin{pmatrix} 0 & 0 & 0 \\ 0 & 0 & -i \\ 0 & i & 0 \end{pmatrix} \quad , \quad \lambda_8 = \frac{1}{\sqrt{3}} \begin{pmatrix} 1 & 0 & 0 \\ 0 & 1 & 0 \\ 0 & 0 & -2 \end{pmatrix}$$

As generators, they obey the commutation relations

$$[\lambda_a, \lambda_b] = 2i f_{abc} \lambda_c \qquad (a, b, c = 1, ...8)\,, \tag{2.18}$$

where the f-coefficients are totally antisymmetric structure constants of $SU(3)$. The non-vanishing elements are,

$$f_{123} = 1, \quad f_{147} = \frac{1}{2}, \quad f_{156} = -\frac{1}{2}, \quad f_{246} = \frac{1}{2}, \quad f_{257} = \frac{1}{2}$$
$$f_{345} = \frac{1}{2}, \quad f_{367} = -\frac{1}{2}, \quad f_{458} = \sqrt{\frac{3}{2}}, \quad f_{678} = \sqrt{\frac{3}{2}}\,.$$

Note that the group $SU(3)$ has an infinite number of irreducible representations $\boldsymbol{R} = \mathbf{1}$, $\mathbf{3}$, $\bar{\mathbf{3}}$, $\mathbf{6}$, $\bar{\mathbf{6}}$, $\mathbf{8}$, $\mathbf{10}$, $\overline{\mathbf{10}}$, ... where each irreducible representation is labeled in terms of its dimensionality. For example, quarks, antiquarks, and gluons are assigned to the representations $\mathbf{3}, \bar{\mathbf{3}}, \mathbf{8}$.

One can show that $\mathcal{L}_{\rm QCD}$ is invariant under the local $SU(3)$ transformations, expressed in Eqs. (2.16) and (2.17), respectively. Before showing the invariance of $\mathcal{L}_{\rm QCD}$, hereafter (so in the later chapters), we use the vector notations for A^a_μ, D_μ, and $F^a_{\mu\nu}$, defined as

$$\boldsymbol{A}_\mu \equiv \frac{\lambda_a}{2} A^a_\mu\,. \tag{2.19}$$
$$\boldsymbol{D}_\mu \psi \equiv (\partial_\mu + i g_S \boldsymbol{A}_\mu)\, \psi\,, \tag{2.20}$$
$$\boldsymbol{F}_{\mu\nu} \equiv \partial_\mu \boldsymbol{A}_\nu - \partial_\nu \boldsymbol{A}_\mu + i[\boldsymbol{A}_\mu, \boldsymbol{A}_\nu]\,, \tag{2.21}$$

where the $\boldsymbol{A}_\mu$ obeys the commutation relations

$$[\boldsymbol{A}_\mu, \boldsymbol{A}_\nu] = i f_{abc} \frac{\lambda^a}{2} A^b_\mu A^c_\nu\,. \tag{2.22}$$

Thus, one can obtain the a-th component of the field strength tensor, $\boldsymbol{F}_{\mu\nu} = \{F^a_{\mu\nu}\}$, by multiplying the above equation from the left by $\lambda^a/2$ and taking the trace. With these notations, the covariant derivative, $\boldsymbol{D}_\mu$, transforms under the local $SU(3)$ transformations as

$$\boldsymbol{D}_\mu \to U(\theta) \boldsymbol{D}_\mu\,, \tag{2.23}$$

and next, by using Eq. (2.22), we get the commutation relation between the covariant derivatives

$$[\boldsymbol{D}_\mu, \boldsymbol{D}_\nu] = i g_S \boldsymbol{F}_{\mu\nu}\,. \tag{2.24}$$

Now, from Eq. (2.24), one can easily verify that the field strength tensor, $\boldsymbol{F}_{\mu\nu}$, transforms as

$$\boldsymbol{F}_{\mu\nu} \to U(\theta)\boldsymbol{F}_{\mu\nu}U^{-1}(\theta)\,. \tag{2.25}$$

Therefore, if we perform $SU(3)$ transformation for $\mathcal{L}_{\rm QCD}$, all $U(\theta)$ terms will be canceled, *i.e.,* the QCD Lagrangian, $\mathcal{L}_{\rm QCD}$, is invariant under the local $SU(3)$ transformations of the color degree of freedom.

One of the important features of the QCD Lagrangian is that it is based on nonabelian gauge group coupling to color. This nonabelian group property results in an important phenomenon called "color confinement", in which the coupling constant becomes strong at long distance and weak at short distance. As mentioned in previous section, this color confinement had been a big obstacle to the study of the hadron spectrum in the low-energy regime, perturbatively, due to the large coupling constant. However, since Wilson's introduction of lattice QCD [21], which formulates QCD on a discretized Euclidean space-time, it has been possible to study QCD nonperturbatively in the strong coupling regime. In the next chapter, I will discuss lattice QCD.

CHAPTER 3

INTRODUCTION TO LATTICE QCD

In this chapter, I give a brief review of the lattice formulation of QCD, which forms the basis of the research topics in Chapters 4, 5, and 6.

3.1 Feynman path integral

Feynman path integration [22] is the basic framework for the lattice gauge theory. That is, the quantum lattice gauge theory is defined through classical lattice actions via the Feynman path integral in a discretized Euclidean space-time, where the Euclidean space-time can be achieved by performing a Wick rotation, $t \to it$, to Minkowski space-time. Therefore, rather than describing the Feynman path integral in continuous Minkowski space-time, I discuss it in a discretized Euclidean space-time with finite lattice spacing a.

For illustration, I consider a simple quantum mechanical system for a single particle in a potential $V(x)$ and show how we discretize path integral. Consider a Green's function (or propagator) that gives the evolution of a position eigenstate $|x_i\rangle$ from t_i to t_f controlled by a given Hamiltonian. It can be written in terms of a Feynman path integral as

$$G(x_f, t_f; x_i, t_i) = \langle x_f | e^{-H(t_f - t_i)} | x_i \rangle = \int \mathcal{D}x(t) e^{-S[x]} \tag{3.1}$$

where the integration with measure $\mathcal{D}x(t)$ is the sum over all possible positions with $x(t_i) = x_i$ and $x(t_f) = x_f$. $S[x]$ is the classical action given by

$$S[x] = \int_{t_i}^{t_f} dt \mathcal{L}(x, \dot{x}) \equiv \int_{t_i}^{t_f} dt \left[\frac{m\dot{x}^2}{2} + V(x) \right] , \tag{3.2}$$

where $\mathcal{L}$ is Lagrangian density. Our ultimate goal is to show how one can implement the path integral on a computer. Consider the discretized path, in time,

$$t_j = t_i + ja \qquad \text{for } j = 0, 1, ...N \tag{3.3}$$

where a is finite lattice spacing,

$$a \equiv \frac{t_f - t_i}{N} . \tag{3.4}$$

Later, we take $a \to 0$. Note that in Eq. (3.1), $\int \mathcal{D}x(t)$ means that we integrate over all possible paths. To define what this means as well as making the integration tractable for numeric computation, we consider sets of discretized paths characterized by "configurations", with $N+1$ "sites",

$$x = \{x_0, x_1, ..., x_N\} \tag{3.5}$$

and the derivative

$$\dot{x} = \frac{x_{j+1} - x_j}{a} \,. \tag{3.6}$$

That is, the measure, $\int \mathcal{D}x$, now becomes

$$\int \mathcal{D}x \to A \int dx_1 ... dx_{N-1} \,, \tag{3.7}$$

where A is a normalization constant which depends on the lattice spacing a. We denote the discretized lattice action as S_{lat}, given by

$$S_{lat} = \sum_{j=0}^{N-1} \left[\frac{m}{2a}(x_{j+1} - x_j)^2 + aV(x_j) \right] \,. \tag{3.8}$$

As an example, consider the propagator $\langle x|e^{-HT}|x'\rangle$, in which we set set $x_0 = x$ and $x_N = x'$ and $t_f - t_i = T$. By inserting a complete set of energy eigenstate,

$$\mathbb{1} = \sum_n |n\rangle\langle n| \,, \tag{3.9}$$

where $|n\rangle$ is the energy eigenket satisfying $H|n\rangle = E_n|n\rangle$ spanning the Hilbert space. Then we get

$$\langle x|e^{-HT}|x'\rangle = \sum_n \langle x|n\rangle e^{-E_n T}\langle n|x'\rangle \xrightarrow{T\to\infty} \langle x|0\rangle\langle 0|x'\rangle e^{-E_0 T} \,, \tag{3.10}$$

where the sum is dominated by the ground state energy, E_0, when T is large. At the same time, we can rewrite this propagator as a discrete quantum mechanical Green function involving the discretized action, S_{lat}, as

$$\langle x|e^{-HT}|x'\rangle = A \int_{-\infty}^{\infty} dx_1 ... dx_{N-1} e^{-S_{lat}[x]} \tag{3.11}$$

Now, by calculating Eq. (3.11) numerically and fitting it to the model expressed as Eq. (3.10), we can get the ground state energy, E_0, which is the vacuum energy in quantum field theory.

The path integral formulation can also provide the thermal and vacuum expectation values of an observable, $\mathcal{O}$, in a quantum mechanical system. The expectation value can be defined through

$$\langle \mathcal{O} \rangle \equiv \frac{\mathrm{Tr}\, \mathcal{O} \exp(-\beta H)}{Z(\beta)} \,, \tag{3.12}$$

where $Z(\beta)$ is the quantum partition function,

$$Z(\beta) \equiv \mathrm{Tr}\exp(-\beta H)\,, \tag{3.13}$$

and the trace is taken over all spin, color, and spatial sites. Thus, unlike Eq. (3.1), by setting $x_f = x_i$, the numerator and the denominator can be expressed as the path integral formulation,

$$\mathrm{Tr}\,\mathcal{O}e^{-\beta H} = \int \mathcal{D}x(t)\mathcal{O}[x]\exp\left(-S[x]\right), \tag{3.14}$$

$$Z(\beta) = \int \mathcal{D}x(t)\exp\left(-S[x]\right) \qquad \text{for } \beta = \frac{1}{T}\,. \tag{3.15}$$

The Feynman technique allows us to calculate this expectation value numerically by multi-dimensional integral so that we can calculate some important physical quantities such as masses decay constants from this expectation value.

As an example, let us consider the expectation value of $x(t_\beta)x(t_\alpha)$,

$$\langle x(t_\beta)x(t_\alpha)\rangle \equiv \frac{\int \mathcal{D}x(t)x(t_\beta)x(t_\alpha)e^{-S[x]}}{\int \mathcal{D}x(t)e^{-S[x]}}\,. \tag{3.16}$$

Again, set $t_f - t_i = \beta$ and $t_\beta - t_\alpha = t$. One can write the path integral, on the right-hand side of Eq. (3.16), in its discretized version :

$$A'\int_{-\infty}^{\infty} dx_1 ... dx_{N-1}x_\beta x_\alpha e^{-S_{lat}[x]}\,. \tag{3.17}$$

Again, we can calculate Eq. (3.17) numerically, and fit it to Eq. (3.25) to get the first excited state energy, E_1.

One can carry out the path integration using a Monte Carlo method. We generate a large number (N_{cf}) of random path configurations,

$$x^{(\zeta)} = \{x_0^{(\zeta)}, x_1^{(\zeta)}, ..., x_N^{(\zeta)}\}, \qquad \text{for } \zeta = 1, 2, ..., N_{cf}\,, \tag{3.18}$$

such that the probability $P[x^{(\zeta)}]$ to get the path $x^{(\zeta)}$ is proportional to $\exp\left(-S(x)\right)$. This can be done by commonly used acceptance-rejection sampling. Then, the desired propagator is the weighted average over such paths:

$$\langle x(t_\beta)x(t_\alpha)\rangle \approx \overline{\mathcal{O}} = \frac{1}{N_{cf}}\sum_{\zeta=1}^{N_{cf}} \mathcal{O}(x^{(\zeta)})\,. \tag{3.19}$$

With the Monte Carlo method, the averaged value $\overline{\mathcal{O}}$ is never exact unless $N_{cf} \to \infty$. The uncertainty σ can be obtained from the variance,

$$\sigma^2 = \frac{\overline{\mathcal{O}^2} - \overline{\mathcal{O}}^2}{N_{cf}}\,. \tag{3.20}$$

Now, we can obtain the fit model to extract the physical information from the expectation value, $\langle x(t_\beta)x(t_\alpha)\rangle$, by using the Heisenberg picture $x(t) = e^{Ht}xe^{-Ht}$. It can be rewritten as

$$\langle x(t_\beta)x(t_\alpha)\rangle = \sum_{n=0}^{\infty}\langle n|e^{-E_n(t_f-t_\beta)}xe^{-H(t_\beta-t_\alpha)}xe^{-E_n(t_\alpha-t_i)}|n\rangle \tag{3.21}$$

$$= \sum_{n=0}^{\infty} e^{-E_n\beta}\langle n|xe^{-(H-E_n)t}x|n\rangle\,. \tag{3.22}$$

If we consider $\beta \to \infty$ limit ($T \to 0$), only the vacuum state, E_0, dominates. Therefore,

$$\langle x(t_\beta)x(t_\alpha)\rangle \xrightarrow{\beta\to\infty} \langle 0|xe^{-(H-E_0)t}x|0\rangle\,. \tag{3.23}$$

Inserting a complete set of energy eigenstates given by Eq. (3.9), we get

$$\langle x(t_\beta)x(t_\alpha)\rangle = \sum_n |\,\langle 0|x|n\rangle\,|^2 e^{-(E_n-E_0)t}\,. \tag{3.24}$$

Since E_0 is a constant vacuum energy, we can shift all energies by the amount E_0 so that $E_0 = 0$. Also, because we are interested in extracting the first excited energy, E_1, we take the limit $t \to$ large, but still small enough compared with β. Then, the above equation reduces to

$$\langle x(t_\beta)x(t_\alpha)\rangle \xrightarrow{t\ \text{large}} |\,\langle 0|x|1\rangle\,|^2 e^{-E_1 t}\,. \tag{3.25}$$

Therefore, to obtain the ground state, E_1, we fit the numeric data obtained from the path integral formulation to the above equation.

3.2 Lattice QCD actions

Next, I introduce the lattice QCD actions [23, 24]. In order to achieve this, we need to discretize both space and time. The action should be gauge invariant, and for $a \to 0$, it should be equivalent to the continuum QCD action, expressed by Eq. (2.13).

Consider a fermion field $\psi(x)$ on the lattice. Analogous to the continuum field as described in Chap. 2, $\psi(x)$ and $\bar{\psi}(x)$ transform under the $SU(3)$ color gauge transformation, $\mathcal{U}(x)$ as follows:

$$\psi(x) \to \mathcal{U}(x)\psi(x), \quad \bar{\psi}(x) \to \bar{\psi}(x)\mathcal{U}(x)^\dagger\,. \tag{3.26}$$

Next, we introduce a link variable involving the gauge field, $\boldsymbol{A}_\mu(x)$, on the lattice,

$$U_\mu(x) = \exp(iag_S\boldsymbol{A}_\mu(x))\,, \tag{3.27}$$

where g_S is the coupling constant and $U_\mu(x)$ is associated with a link connecting two lattice sites along the μ direction (see Fig. 3.1). Analogous to the continuum gauge field Eq. (2.17),

Figure 3.1. The link variables $U_\mu(x)$ and $U_{-\mu}(x)$ connecting two lattice sites denoted as filled dots.

it transforms as

$$U_\mu(x) \to \mathcal{U}(x) U_\mu(x) \mathcal{U}(x+\hat{\mu})^\dagger \,, \tag{3.28}$$

in discretized space-time. With a fermion ψ and a link $U_\mu(x)$, one can write the gauge invariant lattice QCD actions :

$$S_{lat}^{QCD} = S_F^{(naive)} + S_G \,. \tag{3.29}$$

$S_F^{(naive)}$ is the so-called the "naive fermion action",

$$S_F^{(naive)}[\psi, \bar{\psi}, U] = a^4 \sum_x \bar{\psi}(x) \left[\sum_{\mu=1}^{4} \gamma_\mu \frac{U_\mu(x)\psi(x+a\hat{\mu}) - U_{-\mu}(x)\psi(x-a\hat{\mu})}{2a} + m\psi(x) \right] , \tag{3.30}$$

and S_G is the so-called "Wilson gauge action", written as

$$S_G[U] = \frac{2}{g_S^2} \sum_x \sum_{\mu<\nu} \mathrm{Re}\,\mathrm{Tr}[\mathbb{1} - U_{\mu\nu}(x)] \,, \tag{3.31}$$

where we used link variable property, $U_{-\mu}(x) = U_\mu(x - a\hat{\mu})^\dagger$, to construct the covariant derivative on the lattice. $U_{\mu\nu}$ is called the "plaquette variable", which is a product of only four link variables defined as

$$\begin{aligned} U_{\mu\nu}(x) &= U_\mu(x) U_\nu(x + a\hat{\mu}) U_{-\mu}(x + a\hat{\mu} + a\hat{\nu}) U_{-\nu}(x + a\hat{\nu}) \\ &= U_\mu(x) U_\nu(x + a\hat{\mu}) U_\mu(x + a\hat{\nu})^\dagger U_\nu(x)^\dagger \,, \end{aligned} \tag{3.32}$$

where the graphical representation is shown in Fig. 3.2.

One can easily check that $S_F^{(naive)}$ reduces to the continuum form of the action (fermion parts of QCD Lagrangian) given in Eq. (2.13) in the limit $a \to 0$. This can be done by expanding a link variable $U_\mu(x)$ in Eq. (3.27) for small lattice spacing a,

$$U_\mu(x) = \mathbb{1} + iag_S \boldsymbol{A}_\mu(x) + O(a^2) \;\;,\;\; U_{-\mu}(x) = \mathbb{1} - iag_S \boldsymbol{A}_\mu(x - a\hat{\mu}) + O(a^2) \,. \tag{3.33}$$

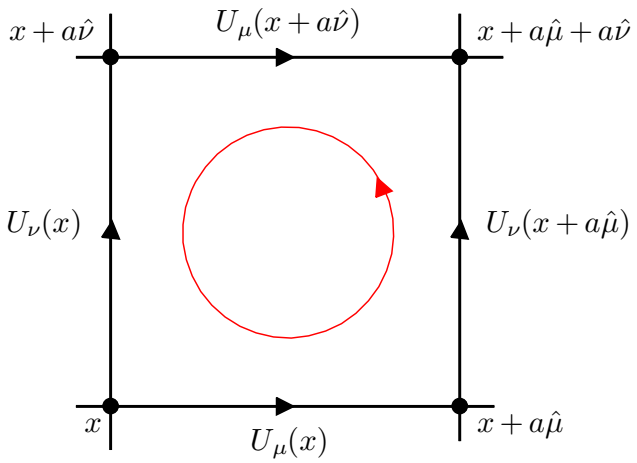

Figure 3.2. The plaquette $U_{\mu\nu}$ which consists of the four link variables. The circle indicates the order that the link variables run through.

Then, by inserting Eq. (3.33) into Eq. (3.30), we rewrite naive action as

$$\begin{aligned} S_F^{(naive)}[\psi, \bar{\psi}, U] &= a^4 \sum_x \bar{\psi}(x) \left[\sum_{\mu=1}^{4} \gamma_\mu \left(\frac{\psi(x + a\hat{\mu}) - \psi(x - a\hat{\mu})}{2a} \right.\right. \\ &+ \left.\left. ig_s \frac{\boldsymbol{A}_\mu(x)\psi(x + a\hat{\mu}) + \boldsymbol{A}_\mu(x - a\hat{\mu})\psi(x - a\hat{\mu})}{2} \right) + m\psi(x) + O(a) \right] . \end{aligned} \tag{3.34}$$

As $a \to 0$, the derivative part of the above equation reduces to the covariant derivative and $O(a)$ vanishes; thus, $S_F^{(naive)}$ satisfies the continuum limit.

For the Wilson gauge action, it is slightly more complex to show whether S_G assumes its continuum form. First, by using the Baker-Campbell-Hausdorff formula,

$$e^A e^B = e^{A+B+\frac{1}{2}[A,B]+\ldots} , \tag{3.35}$$

and performing a Taylor expansion of the gauge fields,

$$\boldsymbol{A}_\nu(x + a\hat{\mu}) = \boldsymbol{A}_\nu(x) + a\partial_\mu \boldsymbol{A}_\nu(x) + O(a^2) , \tag{3.36}$$

one can easily check that the plaquette variable becomes

$$U_{\mu\nu}(x) = \exp\left(ia^2 g_S (\partial_\mu \boldsymbol{A}_\nu(x) - \partial_\nu \boldsymbol{A}_\mu(x) + i[\boldsymbol{A}_\mu(x), \boldsymbol{A}_\nu(x)]) + O(a^3) \right) \tag{3.37}$$

$$= \exp(ia^2 g_S \boldsymbol{F}_{\mu\nu}(x) + O(a^3)) \tag{3.38}$$

where we use the continuum definition of $\boldsymbol{F}_{\mu\nu}$ given in Eq. (2.14). Now, inserting Eq. (3.38) into Eq. (3.31), we get

$$S_G[U] = \frac{a^4}{2} \sum_x \sum_{\mu,\nu} \mathrm{Tr}[\boldsymbol{F}_{\mu\nu}(x)^2] + O(a^2)\,, \tag{3.39}$$

where the Wilson gauge action is approximately the continuum QCD gauge action up to $O(a^2)$ as shown in Eq. (2.13). Therefore, by taking $a \to 0$, both $S_F^{(naive)}$ and S_G reduce to the continuum QCD actions.

3.3 Fermions action on the lattice

In this section, I introduce the fermion propagator given by the inverse of the Dirac matrix. As I show below, the fermion propagator derived from the naive action suffers from a lattice artifact called "fermion doubling" contributed from high momentum excitation at the edges of the Brillouin zone (BZ), which has no analog in continuum. To overcome this lattice artifact, various types of lattice actions have been developed. I give an introduction to some of these actions.

3.3.1 Grassmann numbers

All fermion fields obey anticommutation relations. Therefore, they are represented classically as Grassmann anticommuting numbers. Therefore to perform the fermionic path integrals, it is useful to display two key integration formulas related to the anticommutating numbers, η. One can find all the proofs in any related textbook, *e.g.,* Ref. [17].

Two Grassmann variables obey the following anticommutation relation :

$$\eta_i \eta_j = -\eta_j \eta_i \qquad \text{for } i,j = 1,...,N\,, \tag{3.40}$$

so $\eta_i^2 = 0$. Grassmann variable, η_i transforms linearly,

$$\eta_i' = \sum_{j=1}^{N} M_{ij} \eta_j\,, \tag{3.41}$$

where M is a complex $N \times N$ matrix. One integral formula needed here is called the "Matthews-Salam formula",

$$Z_F \equiv \int d\eta_N d\bar{\eta}_N ... d\eta_1 \bar{\eta}_1 \exp\left(\sum_{i,j=1}^{N} \bar{\eta}_i M_{ij} \eta_j \right) = \det[M]\,, \tag{3.42}$$

where $\bar{\eta}_i$ is another set of Grassmann numbers satisfying Eq. (3.40) with $\bar{\eta}_j$ as well as η_j. Another useful integration formula for Grassmann numbers is called "Wick's theorem" :

$$\langle \eta_{i_1}\bar{\eta_{j_1}}...\eta_{i_n}\bar{\eta_{j_n}}\rangle \equiv \frac{1}{Z_F}\int\prod_{k=1}^{N} d\eta_k d\bar{\eta}_k \eta_{i_1}\bar{\eta_{j_1}}...\eta_{i_n}\exp\left(\sum_{l,m=1}^{N}\bar{\eta}_l M_{lm}\eta_m\right)$$
$$= (-1)^n \sum_{P(1,2,...,n)} \text{sign}(P)(M^{-1})_{i_1 j_{P_1}}...(M^{-1})_{i_2 j_{P_2}}...(M^{-1})_{i_n j_{P_n}} \quad (3.43)$$

where the sum in the second line runs over all permutations $P(1,2,...,n)$ of the indices $1,2,...,n$, and sign(P) is the sign of the permutation P. The expectation values in Wick's theorem are often referred to as "n-point functions" abbreviated as "n-pt functions". We will use this term often in later chapters.

3.3.2 The lattice path integral and fermion propagator

On the lattice, the quantum expectation value of an observable can be calculated from the path integral. As introduced in previous chapters, the lattice QCD action can be divided into two parts - fermion and gauge field parts. Thus, it is convenient to write the expectation value of an observable, $\mathcal{O}$, which generally depends on both fermion fields, ψ and $\bar{\psi}$, and link variable, U, as

$$\langle\mathcal{O}\rangle = \left\langle\left\langle\mathcal{O}[U,\psi,\bar{\psi}]\right\rangle_F\right\rangle_G \quad (3.44)$$

where $\langle...\rangle_F$ is fermionic part and $\langle...\rangle_G$ is the gauge field part of the path integral. The fermionic part of the path integral, $\langle...\rangle_F$, is defined by

$$\left\langle\mathcal{O}[U,\psi,\bar{\psi}]\right\rangle_F = \frac{1}{Z_F[U]}\int\mathcal{D}[\psi,\bar{\psi}]e^{-S_F[\psi,\bar{\psi},U]}\mathcal{O}[\psi,\bar{\psi},U]\,, \quad (3.45)$$

where $\mathcal{D}[\psi,\bar{\psi}]$ is an integral over the Grassmann fields ψ and $\bar{\psi}$. $Z_F[U]$ is the fermionic partition function,

$$Z_F[U] = \int\mathcal{D}[\psi,\bar{\psi}]e^{-S_F[\psi,\bar{\psi},U]}\,. \quad (3.46)$$

Using Eq. (3.42), one can perform the integral over the Grassmann fields

$$Z_F[U] = \det[D] = \exp(\text{Tr}\ln D)\,, \quad (3.47)$$

where the fermionic partition function, Z_F, is also called the "fermion determinant", and D is Dirac matrix. For the naive fermion action, the expression of the Dirac matrix can be obtained by rewriting the naive fermion action given in Eq. (3.30) as

$$S_F^{(naive)}[\psi,\bar{\psi},U] = a^4\sum_{x,y}\sum_{a,b,\alpha,\beta}\bar{\psi}(x)^a_\alpha D(y;x)^{a,b}_{\alpha,\beta}\psi(x)^a_\beta\,, \quad (3.48)$$

where Dirac spin (Greek) and color (Roman) indices are explicitly shown to clarify D as matrix. Here, $D(y;x)$ is called naive Dirac operator on the lattice and it is given by

$$D(y;x)^{a,b}_{\alpha,\beta} = \sum_{\mu=1}^{4}(\gamma_\mu)_{\alpha\beta}\frac{U_\mu(y)^{ab}\delta_{y+a\hat{\mu},x} - U_{-\mu}(y)^{ab}\delta_{y-a\hat{\mu},x}}{2a} + m\delta_{\alpha,\beta}\delta_{a,b}\delta_{x,y}\,. \quad (3.49)$$

Finally, let $\mathcal{O}_F[U] \equiv \left\langle \mathcal{O}[U,\psi,\bar{\psi}] \right\rangle_F$ for an operator $\mathcal{O}$. Then, we perform the gauge field part of the path integral

$$\langle \mathcal{O} \rangle = \langle \mathcal{O}_F[U] \rangle_G = \frac{1}{Z} \int \mathcal{D}[U] e^{-S_G[U]} \det[D] \mathcal{O}_F[U] \,, \tag{3.50}$$

to obtain an expectation value of an observable, $\mathcal{O}$.

One can also obtain the fermionic expectation value of a fermion and anti-fermion fields, $\left\langle \psi(y)\bar{\psi}(x) \right\rangle_F$, *i.e.,* a two-point function of fermions in terms of the Dirac matrix. From Eq. (3.43), one can write

$$\left\langle \psi(y)^a_\alpha \bar{\psi}(x)^b_\beta \right\rangle_F = a^{-4} D^{-1}(y;x)^{ab}_{\alpha\beta} \,, \tag{3.51}$$

which is the inverse of the Dirac matrix.

3.3.3 Fermion doubling problem

The quark propagator, the inverse of Dirac matrix, given in Eq. (3.51), plays an important role in calculating any observable quantities in lattice QCD. Therefore, it is interesting to investigate the property of the fermion and anti-fermion propagator. Consider the Fourier transformation of the propagator for the free, naive action given in Eq. (3.30) with $U_\mu(x) = 1$,

$$D^{-1}(p) = \frac{m\mathbb{1} + ia^{-1}\sum_\mu \gamma_\mu \sin(p_\mu a)}{m^2 + a^{-2}\sum_\mu \sin(p_\mu a)^2} \,. \tag{3.52}$$

To investigate the poles, it is convenient to take the massless limit. Then, the inverse Dirac matrices on the lattice and in continuum are

$$D^{-1}(p) = \frac{ia^{-1}\sum_\mu \gamma_\mu \sin(p_\mu a)}{a^{-2}\sum_\mu \sin(p_\mu a)^2} \xrightarrow{a\to 0} \frac{-i\sum_\mu \gamma_\mu p_\mu}{p^2} \,. \tag{3.53}$$

In the continuum, it is obvious that the momentum-space propagator for massless fermions has a pole at

$$p = (0,0,0) \,. \tag{3.54}$$

This pole coincides with the pole of the single fermion propagator described by the continuum Dirac operator. On the other hand, the lattice propagator, before we take the continuum limit, has 15 additional poles :

$$p = \left(\frac{\pi}{a},0,0,0\right), \left(0,\frac{\pi}{a},0,0\right), ..., \left(\frac{\pi}{a},\frac{\pi}{a},\frac{\pi}{a},\frac{\pi}{a}\right) \,. \tag{3.55}$$

Therefore, we get states on all 16 corners of the Brillouin zone (BZ) in a $d = 4$ hypercube. This is called the "fermion doubling problem". As mentioned at the beginning of this chapter, to overcome this lattice artifact, various lattice actions have been invented. In the following subsections, I introduce two of those actions, Wilson and staggered-fermion actions.

3.3.4 Wilson fermions

To solve the fermion doubling problem on the lattice, Wilson proposed adding an "irrelevant term", *i.e.,* which vanishes in the continuum limit, $a \to 0$,

$$S_F^{(W)} = S_F^{(naive)} - \frac{ar}{2} \sum_x \Delta\psi(x) \tag{3.56}$$

where r is the Wilson parameter, and Δ is the four-dimensional lattice Laplacian defined as

$$\Delta\psi(x) = \sum_{\mu=1}^{4} \frac{1}{a^2} \left[U_\mu(x)\psi(x + a\hat{\mu}) + U_{-\mu}(x)\psi(x - a\hat{\mu}) - 2\psi(x) \right] . \tag{3.57}$$

Now the mass term, m, in the Fourier transformation given by Eq. (3.52) becomes

$$m \to M(p) = m + \frac{2r}{a} \sum_\mu \sin^2 \left(\frac{p_\mu a}{2} \right) . \tag{3.58}$$

Therefore as $a \to 0$, $M(p)$ approaches m. However, near the corners of the BZ, $M(p)$ diverges as $a \to 0$. This eliminates the fermion doubling problem, but at the expense of breaking the "chiral symmetry" of the original naive action. Here, the chiral symmetry means the invariance of the continuum action (or Lagrangian density) under the chiral rotation,

$$\psi \to e^{i\theta\gamma_5}\psi \ , \quad \bar{\psi} \to \bar{\psi} e^{i\theta\gamma_5} , \tag{3.59}$$

in the massless limit ($m \to 0$).

3.3.5 Hopping expansion

The Dirac matrix inverse, D^{-1}, can be expanded for a large quark mass m. For the Wilson action, we can rewrite the Dirac matrix as [25–27]

$$D = C(\mathbb{1} - \kappa H), \qquad \text{with } \kappa = \frac{1}{2(ma + 4r)}, \tag{3.60}$$

$$H(y; x) = \sum_{\mu=\pm1}^{\pm4} (r - \gamma_\mu) U(y) \delta_{y,x+a\hat{\mu}} , \tag{3.61}$$

where κ is the hopping parameter and H is the hopping matrix. The constant C is irrelevant because it can be absorbed into the fermion fields. Since κ becomes small for large mass, D^{-1} can be expanded as

$$D^{-1} = (\mathbb{1} - \kappa H)^{-1} = \sum_{j=0}^{\infty} \kappa^j H^j , \tag{3.62}$$

where the j-th power of H, H^j, can be calculated by using Eq. (3.61),

$$H^j(y; x) = \sum_{\mu=\pm1}^{\pm4} \prod_{i=1}^{j} (r - \gamma_\mu) P_{\mu_1 \ldots \mu_j}(x) \delta_{y,x+a\hat{\mu}_1+\ldots+a\hat{\mu}_j} . \tag{3.63}$$

Here, $P_{\mu_1 \ldots \mu_j}(x)$ represents the paths formed from the product of link variables connecting the lattice sites x and y :

$$P_{\mu_1 \ldots \mu_j}(x) = U_{\mu_1}(x) U_{\mu_2}(x + a\hat{\mu}_1) \ldots U_{\mu_j}(x + a\hat{\mu}_1 + \ldots + a\hat{\mu}_{j-1}) \,. \tag{3.64}$$

The path of length j comes with a power of κ^j. Therefore, for a given value of x and y, the leading term is the shortest path. In the later chapters, Chap. 4, 5 and 6, I will always display the specific κ values, instead of the corresponding heavy quark masses that are used for the lattice simulation.

3.3.6 Staggered fermions

The staggered fermion formulation was first suggested by Kogut and Susskind [28–30]. The idea is to eliminate the redundant fermion modes. It reduces the size of the BZ by redistributing the spinor degrees of freedom across different lattice sites. As a result, the sixteen-fold degenerate doublers of naive fermions becomes a four-fold degenerate species. To achieve this, we start from the Kawamoto-Smit transformation $\psi(x) = \Omega(x)\Phi(x)$ (*e.g.,* Ref. [24]), where

$$\Omega(x) = \gamma_1^{x_1} \gamma_2^{x_2} \gamma_3^{x_3} \gamma_4^{x_4} \,, \tag{3.65}$$

and use the relations,

$$\Omega(x)^\dagger \gamma_\mu \Omega(x + a\hat{\mu}) = (-)^{x_1 + x_2 + \ldots + x_{\mu-1}} \equiv \alpha_\mu(x) \tag{3.66}$$

$$\Omega(x)^\dagger \Omega(x) = 1 \,. \tag{3.67}$$

We then rewrite the naive action in Eq. (3.30) as

$$S_F^{(naive)} = a^4 \sum_x \left(\sum_{\mu=1}^{4} \alpha_\mu(x) \overline{\Phi}(x) \frac{U_\mu(x)\Phi(x + a\hat{\mu}) - U_\mu(x - a\hat{\mu})^\dagger \Phi(x - a\hat{\mu})}{2a} + m\overline{\Phi}(x)\Phi(x) \right) , \tag{3.68}$$

where the action becomes diagonal in spinor space. Now, let us see how this spin diagonalization affects the propagator. Because the transformed Dirac matrix of Eq. (3.68) has no explicit spin-dependence, we can drop all but one "spin", or from Eq. (3.51), we can define the staggered fermion propagator, $S^{ab}(y; x)$ as

$$\left\langle \Phi_\alpha^a(y) \overline{\Phi}_\beta^b(x) \right\rangle_F = \delta_{\alpha\beta} S^{ab}(y; x) \,, \tag{3.69}$$

where $S(y; x)$ has no spin component. Then, the naive fermion 2-pt propagator in Eq. (3.51) can be rewritten as

$$\left\langle \psi(y)^a_\alpha \psi(x)^b_\beta \right\rangle_F = \Omega(y)_{\alpha\gamma} \left\langle \Phi^a_\gamma(y) \Phi^b_\delta(x) \right\rangle_F \Omega(y)^\dagger_{\delta\beta} \tag{3.70}$$

$$= \Omega(y)_{\alpha\gamma} \delta_{\gamma\delta} \Omega(y)^\dagger_{\delta\beta} S^{ab}(y;x) \tag{3.71}$$

$$= \left[\Omega(y)\Omega(x)^\dagger\right]_{\alpha\beta} S^{ab}(y;x) \tag{3.72}$$

Therefore, we can reduce the multiplicity of the naive fermion propagator by a factor of four and the spin to one Dirac component. Due to the sign alternation in $\alpha_\mu(x)$ included in $S(y;x)$, the natural unit cell for the staggered fermion field is the 2^4 hypercube. The residual doubler degree of freedom is called "taste". That is, a single staggered fermion corresponds to four tastes of continuum fermions.

One can perform an inverse transform of a staggered fermion basis to the so-called "staggered fermion spin-taste basis",

$$\Phi_\rho(\boldsymbol{n}) = 2\,\mathrm{Tr}\left[\Omega(\boldsymbol{\rho})^\dagger \zeta(\boldsymbol{n})\right], \tag{3.73}$$

where $\Phi_\rho(\boldsymbol{n}) \equiv \Phi(2\boldsymbol{n}+\boldsymbol{\rho})$ and $\boldsymbol{n} \in \mathbb{Z}^3$ so that $2\boldsymbol{n}$ is the the origin of a hypercube and $\rho_\mu = 0$ or 1. $\Omega \equiv \{\Omega^{\alpha t}\}$ where α is a spin index and t is a taste index. Thus, the field ζ has four Dirac spinor components as well as the four taste components and lives on the hypercube with origin at $2\boldsymbol{n}$. By the inverse transform, the action can be rewrite as

$$S = \sum_{\boldsymbol{n},\mu} b^4 \bar{\zeta}(\boldsymbol{n}) \left[(\gamma_\mu \otimes \mathbb{1})\boldsymbol{D}_\mu \zeta(\boldsymbol{n}) + a S_{tb,1} + O(a^2) + m b^4 \bar{\zeta}(\boldsymbol{n}) \mathbb{1} \otimes \mathbb{1} \zeta(\boldsymbol{n})\right] \tag{3.74}$$

where the sum over $\boldsymbol{n}$ runs over all hypercubes of the lattice, $b = 2a$, $\boldsymbol{D}_\mu$ is the covariant derivative on the lattice and the tensor product notation is spin $\otimes$ taste. $S_{tb,1}$ contains dimension five fermion bilinear terms [1] , such as $\gamma_5 \otimes \gamma_\mu\gamma_5 \boldsymbol{D}^2_\mu$, $(\gamma_\mu - \gamma_\nu) \otimes \mathbb{1}\boldsymbol{F}_{\mu\nu}$, and $\gamma_5\sigma_{\mu\nu} \otimes (\gamma_\mu + \gamma_\nu)\gamma_5 \boldsymbol{F}_{\mu\nu}$ where $\sigma_{\mu\nu} = i/2[\gamma_\mu, \gamma_\nu]$. These terms explicitly break the taste symmetry at the nonzero lattice spacing, while in the continuum limit, taste symmetry is restored.

3.4 Improved actions

As we discretize the derivative terms, *e.g.,* Eqs. (3.30) and (3.8), it is inevitable to get unwanted discretization effects. Typically, for the fermion actions, discretization effects are

[1] The action, S, has no dimension. Consider the mass term in the naive action, Eq. (3.30). The dimension of a^4 is fm^4, thus the dimension of $m\bar{\psi}\psi$ term should be fm^{-4} or MeV^4. Therefore, because the dimension of the mass is MeV, we know that the fermion field, ψ, should have dimension $\mathrm{MeV}^{\frac{3}{2}}$, so it has dimension 3/2. In the same analogy, the gauge field should have dimension one, thus the field strength tensor, $\boldsymbol{F}_{\mu\nu}$, has dimension two. The covariant derivative, $\boldsymbol{D}$, has dimension one. Therefore, we say the terms, for example, such as $m^2\bar{\psi}(x)\psi(x)$ and $m\,\mathrm{Tr}[\boldsymbol{F}_{\mu\nu}\boldsymbol{F}_{\mu\nu}]$ are "dimension five terms".

of order $O(a)$ and for the gauge actions $O(a^2)$. One can reduce these effects, systematically, by adding more correction terms. For example, consider the following symmetric derivative,

$$\frac{f(x+a)-f(x-a)}{2a} = f'(x) + a^2 C^{(2)}(x) + O(a^4)\,. \tag{3.75}$$

By using a Taylor expansion, we can easily identify $C^{(2)}(x) = 1/6 f'''(x)$. Therefore, to eliminate the leading-order discretization effect, we need to add a correction term on the left-hand side of the above equation,

$$\frac{f(x+a)-f(x-a)}{2a} + ca^2 D^{(3)}[f](x) = f' + O(a^4)\,, \tag{3.76}$$

where $D^{(3)}[f]$ is a discretized expression obeying $D^{(3)}[f] \approx f''' + O(a^2)$ and $c = 1/6$. Therefore, we can achieve $O(a^2)$ improvement for the discretized symmetric derivative. With the lattice actions, this kind of improvement is called "Symanzik improvement" [31–33].

3.4.1 Clover action

The clover action is an $O(a)$ improvement of the Wilson lattice action [34]. Because the Lagrangian of the action has dimension four, the leading order of the correction term must be dimension five. Therefore, for the Wilson lattice action, one can achieve $O(a)$ improvement by adding a dimension-five correction term, such as

$$S_F^{(clover)} = S_F^{(Wilson)} + c_{sw} a^5 \sum_x \sum_{\mu<\nu} \bar{\psi}(x) \frac{1}{2} \sigma_{\mu\nu} \hat{F}_{\mu\nu}(x) \psi(x)\,, \tag{3.77}$$

where $\sigma_{\mu\nu} \equiv [\gamma_\mu, \gamma_\nu]/2i$, and c_{sw} is called the Sheikholeslami-Wohlert coefficient [34]. The convenient lattice representation of $\boldsymbol{F}_{\mu\nu}$ is

$$\hat{F}_{\mu\nu}(x) = \frac{-i}{8a^2}(Q_{\mu\nu}(x) - Q_{\nu\mu}(x)) \tag{3.78}$$

where $Q_{\mu\nu}(x)$ is the sum of plaquettes $U_{\mu,\nu}(x)$ (Eq. (3.32)),

$$Q_{\mu\nu}(x) \equiv U_{\mu,\nu}(x) + U_{\nu,-\mu}(x) + U_{-\mu,-\nu}(x) + U_{-\nu,\mu}(x)\,. \tag{3.79}$$

Figure 3.3 shows a schematic plot for $Q_{\mu\nu}(x)$.

3.4.2 Asqtad action

The asqtad action [35–38] is an improvement to the staggered action that reduces the taste-symmetry breaking (see Fig. 3.4) by suppressing taste changing interactions. Lattice artifacts $O(a^2)$ are removed at tree level, and then the order of leading error becomes

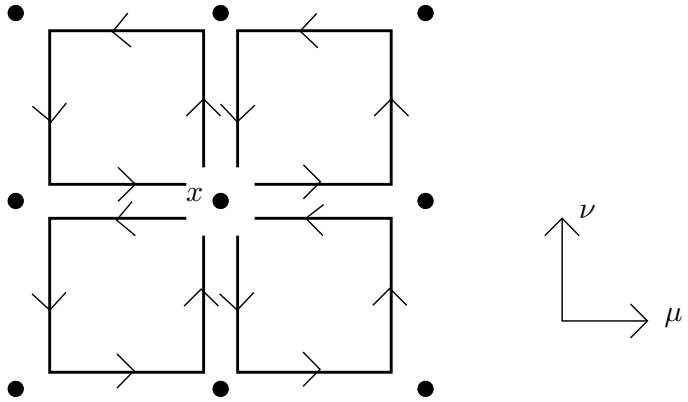

Figure 3.3. Graphical representation of the clover term, $Q_{\mu\nu}(x)$, which is the sum of four plaquettes in the $\mu - \nu$ plane centered at coordinate x.

$O(\alpha a^2)$. The taste symmetry violations can happen due to the interactions between quarks changing their tastes as they exchange high-momentum gluons ($\sim \pi/a$). Fig. 3.5 gives a diagrammatic representation of the correction terms in the "asqtad" improved staggered lattice gauge action. For example, the one link term is

$$c_1 \left[U_\mu(x)\delta_{y,x+a\hat{\mu}} - U_\mu^\dagger(x - a\hat{\mu})\delta_{y,x-a\hat{\mu}} \right] , \tag{3.80}$$

the staple term is

$$c_3 \sum_{\nu\neq\mu} \Bigg[\left\{ U_\nu(x)U_\mu(x+\hat{\nu})U_\nu^\dagger(x+a\hat{\mu}) + U_\nu^\dagger(x-a\hat{\nu})U_\mu(x-a\hat{\nu})U_\nu(x-a\hat{\nu}+a\hat{\mu}) \right\} \delta_{y,x+a\hat{\mu}} - \text{backward staple term} \Bigg] , \tag{3.81}$$

and the Naik term is

$$c_N \left[U_\mu(x)U_\mu(x+a\hat{\mu})U_\mu(x+2a\hat{\mu})\delta_{y,x+3a\hat{\mu}} - \text{backward Naik term} \right] . \tag{3.82}$$

With these terms, one can eliminate errors at $O(a^2)$ leaving $O(a^4)$- and $O(\alpha a^2)$. See Ref. [35] for the detailed explanation of the choices of constants, c_1, c_3, and c_N.

3.4.3 HISQ action

A further improvement to the staggered fermion action is the highly improved staggered quark (HISQ) action [2, 4, 39], an $O(a^2)$ improvement of the staggered lattice action that

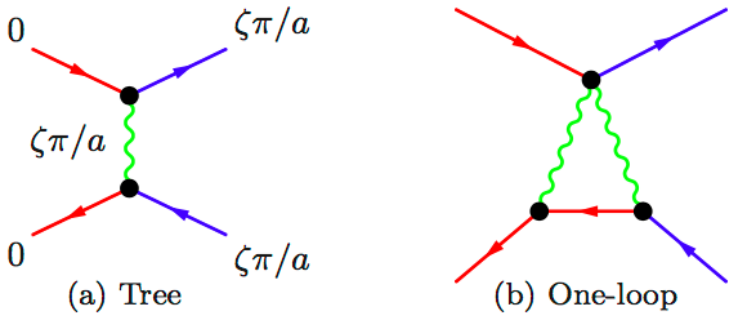

Figure 3.4. Diagrammatic expression for the taste symmetry breaking [2]. The straight lines with different color represent different tastes of quarks. Wiggly lines represent gluons. ζ are the four-dimensional integer vectors, where $\zeta = (1,0,0,0),(1,1,0,0)....$ Thus, $\zeta\pi/a$ indicates the corners of the Brillouin zone

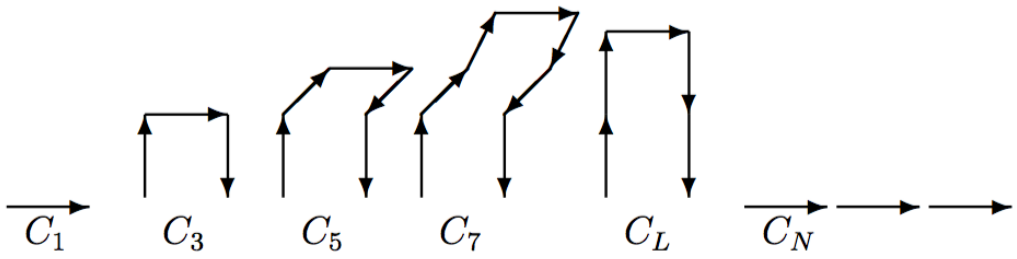

Figure 3.5. Diagrammatic expression for the improvement for the staggered lattice gauge action - asqtad improvement [3]. From the left, the diagrams represent one link term (C_1), the staple term (C_3), the five link term (C_5), the seven link term (C_7), Lapage link term (C_L), and Naik term (C_N), respectively.

also reduces still further the taste-symmetry breaking by suppressing even more the taste-exchanging interactions. Furthermore, it improves the quark dispersion relation, which enables us to simulate charm quarks on the lattice.

At tree level, by adding the $O(a^2)$ correction term, referred to as the Naik term, it achieves an $O(a^2)$ improvement. Further, to suppress taste symmetry breaking, it replaces the link operator $U_\mu(x)$ in quark gluon vertex, $\bar{\psi}\gamma_\mu U_\mu\psi$, by $\mathcal{F}_\mu U_\mu(x)$. The smearing function $\mathcal{F}_\mu$ is defined by [40]

$$\mathcal{F}_\mu \equiv \prod_{\rho\neq\mu}\left(1+\frac{a^2\delta_\rho^{(2)}}{4}\right)\Bigg|_{\text{symm.}}, \tag{3.83}$$

where $\delta_\rho^{(2)}$ approximates a covariant derivative :

$$\delta_\rho^{(2)} \equiv \frac{1}{a^2}\Big[U_\rho(x)U_\mu(x+a\hat{\rho})U_\mu(x+a\hat{\mu}) - 2U_\mu(x) + U_\rho^\dagger(x-a\hat{\rho})U_\mu(x-a\hat{\rho})U_\rho(x-a\hat{\rho}+a\hat{\mu})\Big]\,. \tag{3.84}$$

$\mathcal{F}_\mu$ is called "Fat7" smearing. A schematic representation is shown in Fig. 3.6. Then, the links are reunitarized, and the side links are smeared with asqtad. Therefore, finally the HISQ improvement becomes Fat7$_R \otimes$ Asqtad.

The dominant taste-exchange interactions in asqtad comes from the one-loop diagrams shown in Fig. 3.7. Again, the gluons transfer the momenta of order $\zeta\pi/a$. In the HISQ action, there are 28 terms to cancel these out. The 28 terms involves current-current interaction terms,

$$2\Delta\mathcal{L}_{\text{contact}} = d_5^{(5\mu)}\left|\mathcal{J}_5^{(5\mu)}\right|^2 + ... \tag{3.85}$$

where repeated indices can be understood as summed over except $\nu \neq \mu$. $\mathcal{J}_s^{(n)}$ is a staggered quark operator defined as

$$\mathcal{J}_s^{(n)}(x_B) = \frac{1}{16}\sum_{\delta x_\mu \in \mathbb{Z}_2} \bar{\psi}(x_B+\delta x)\gamma_n \otimes \xi_s \psi(x_B+\delta x) \tag{3.86}$$

and the coefficients $d_n^{(s)}$ are computed by on-shell matching of the taste scattering amplitude, $A(0,0;\zeta\pi/a,-\zeta\pi/a)$. Here, I do not list all of the correction terms. For further discussion, refer to Ref. [4].

3.5 Meson spectroscopy on the lattice

As discussed in Chap. 2, the strong coupling constant, g_S, is larger than unity in the low energy regime. Therefore, there is no proper perturbative method to get the energy spectrum of hadrons. However, in lattice QCD, one can calculate expectation values of observables nonperturbatively in a regime where the strong interacting particles emerge. These expectation values, which can be calculated numerically, often include very useful information about the hadron spectrum. In this section, we discuss how to calculate expectation values and extract the meson spectra on the lattice. I do not discuss baryon spectroscopy, but one can find references in various textbooks, *e.g.,* Ref. [24]

3.5.1 Meson interpolators and correlators

On the lattice, hadron masses are determined from the Euclidean-time correlation functions (or "correlators") , $C(t)$ from time 0 to t, defined as

$$C(t) = \langle 0|\mathcal{O}(t)\mathcal{O}^\dagger(0)|0\rangle\,, \tag{3.87}$$

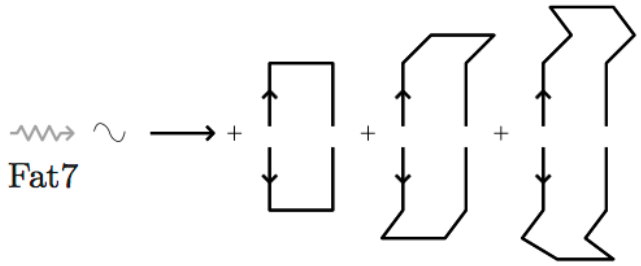

Figure 3.6. A schematic of Fat7 smearing in HISQ action. In the second smearing, the original smeared links are used. [2].

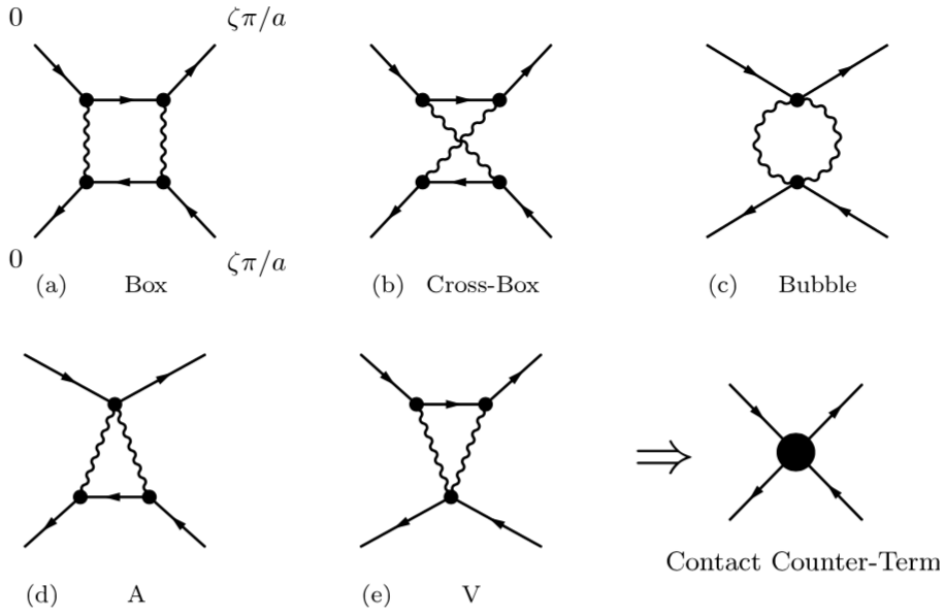

Figure 3.7. The one loop taste exchange contribution from $q\bar{q} \to q\bar{q}$ for the asqtad action [4]. In the HISQ action, these taste breaking terms are further suppressed by employing $2\Delta\mathcal{L}_{\text{contact}}$ in Eq. (3.85).

where $\mathcal{O}(t)$ is an "interpolating operator", or "interpolator" for short. It is an operator that creates the state of interest from the vacuum. In the Heisenberg picture, one can write it as

$$\mathcal{O}(t) = e^{Ht}\mathcal{O}e^{-Ht} \tag{3.88}$$

where H is the QCD hamiltonian. Here, we assume that the time extent, T, of the lattice is sufficiently large that we need only consider the propagation forward in time. By inserting

a complete set of energy eigenstates (Eq. (3.9)), we can rewrite the correlator as

$$C(t) = \sum_{n=0}^{\infty} \langle 0|\mathcal{O}(0)|n\rangle e^{-E_n t} \langle n|\mathcal{O}^{\dagger}(0)|0\rangle \tag{3.89}$$

$$= A_0 + A_1 e^{-E_1 t} + A_2 e^{-E_2 t} + \dots , \tag{3.90}$$

where $A_n = |\langle 0|\mathcal{O}|n\rangle|^2$. Therefore, we ignore this vacuum expectation value, and hereafter, the ground state means the $n = 1$ state. We can perform the fitting to the multiexponential expansion, given by Eq. (3.110). However, before fitting, one can extract an effective ground state energy. At asymptotic times, $t \gg 1$, only the $n = 1$ state dominates. Thus, we can extract the ground state energy from an "effective mass" formula,

$$E_{\text{eff}}(t) = \log \left[\frac{C(t)}{C(t+1)} \right] . \tag{3.91}$$

where E_{eff} is the effective mass in the asymptotic region. Therefore, this method can be used for a rough guide for fitting correlators, not for an exclusive use.

In this dissertation, most of the interesting observables are mesons involving a quark and antiquark pair. Consider measuring a meson correlator

$$C(t) = \sum_{x} \langle 0|\mathcal{O}_A(t, \boldsymbol{x}) \mathcal{O}_B^{\dagger}(0, 0)|0\rangle , \tag{3.92}$$

where

$$\mathcal{O}_{[A,B]}(t, \boldsymbol{x}) = \bar{\psi}^{f_1}(t, \boldsymbol{x}) \Gamma_{[A,B]} \psi^{f_2}(t, \boldsymbol{x}) , \tag{3.93}$$

where Γ_A and Γ_B are gamma matrices, and superscripts f_1 and f_2 represent flavors. The coordinate $(0, \mathbf{0})$ gives the space-time position for the "source" and $(t, \boldsymbol{x})$, for the "sink" of the meson. The total angular momentum and the discrete symmetries (parity and charge conjugation) play an important role in the classification of mesons (and also baryons). Therefore, the gamma matrices, Γ_A and Γ_B, should be properly chosen according to the quantum number of the desired state.

However, concerning total angular momentum, J, the lattice spatial rotational symmetry reduces to symmetries of a cubic lattice [41]. This group is called the "octahedral group" (or the crystallographic point group) denoted as O_h, which is a finite subgroup of the rotation group SO_3. There are only five irreducible representations (irreps) of the octahedral group: $A_1(1)$, $T_1(3)$, $T_2(3)$, $E(2)$, and $A_2(1)$ where each number in the parentheses represents the dimension of the irrep. A given O_h irrep corresponds to many J values. Therefore, there is no unique continuum spin assignment on the lattice. Table 3.1 shows the relation between continuum angular momentum and the lattice irreps. Table 3.2 shows commonly used local

Table 3.1. Left block: continuum total angular momentum (J) subduced into the lattice irreps (O_h) (left) and right block: the lattice irreps (O_h) contributing to the continuum total angular momentum (J).

J	Irreps (O_h)	Irrep (O_h)	J
0	A_1	A_1	$0, 4, ...$
1	T_1	A_2	$3, 6, ...$
2	$T_2 \oplus E$	E	$2, 4, 5, ...$
3	$T_1 \oplus T_2 \oplus A_2$	T_1	$1, 3, 4, 5, ...$
4	$A_1 \oplus T_1 \oplus T_2 \oplus E$	T_2	$2, 3, 4, 5, ...$

Table 3.2. Choices of gamma matrices for the interpolators in Eq. (3.93). From the left, each column shows the state, total angular momentum with parity and charge conjugation, gamma matrices, and the names of some mesons to which they couple.

State	J^{PC}	Γ	Particles
Pseudoscalar	$A_1^{-+}(0^{-+})$	$\gamma_5, \gamma_4\gamma_5$	$\pi^{\pm}, \pi^0, \eta, K^{\pm}, K^0, \eta_c, ...$
Vector	$T_1^{--}(1^{--})$	$\gamma_i, \gamma_4\gamma_i$	$\rho^{\pm}, \rho^0, \omega, K^*, \phi, J/\psi$
Axial vector	$T_1^{++}(1^{++})$	$\gamma_5\gamma_i$	$a_1, f_1, \chi_{c1}, ...$
Scalar	$A_1^{++}(0^{++})$	$1, \gamma_4$	$f_0, a_0, \chi_{c0}, ...$
Tensor	$T_1^{+-}(1^{+-})$	$\gamma_i\gamma_j$	$h_1, b_1, h_c ...$

interpolators and the corresponding particle names. In Chaps. 4, 5, and 6, we use the lattice irreps notation, rather than the continuum total angular momentum.

Now as an example, let us consider iso-singlet meson interpolators, $\mathcal{O} \sim \bar{u}\Gamma u + \bar{d}\Gamma d$. Then, we can write a meson correlator as

$$\begin{aligned}
\left\langle \mathcal{O}_A(y)\mathcal{O}_B^\dagger(x) \right\rangle &\sim \langle \bar{u}(y)\Gamma_A u(y)\bar{u}(x)\Gamma_B u(x)\rangle + [u \leftrightarrow d] \\
&= 2(\Gamma_A)_{\alpha_1\beta_1}(\Gamma_B)_{\alpha_2\beta_2} \left\langle \bar{u}(y)^{c_1}_{\alpha_1} u(y)^{c_1}_{\beta_1} \bar{u}(x)^{c_2}_{\alpha_2} u(x)^{c_2}_{\beta_2} \right\rangle \\
&= 2(\Gamma_A)_{\alpha_1\beta_1}(\Gamma_B)_{\alpha_2\beta_2} \\
&\quad \times \left[\left\langle \bar{u}(y)^{c_1}_{\alpha_1} u(y)^{c_1}_{\beta_1} \right\rangle \left\langle \bar{u}(x)^{c_2}_{\alpha_2} u(x)^{c_2}_{\beta_2} \right\rangle - \left\langle u(x)^{c_2}_{\beta_2} \bar{u}(y)^{c_1}_{\alpha_1} \right\rangle \left\langle u(y)^{c_1}_{\beta_1} \bar{u}(x)^{c_2}_{\alpha_2} \right\rangle \right] \\
&= 2\,\mathrm{Tr}\left[D^{-1}(y;y)\Gamma_A\right] \mathrm{Tr}\left[D^{-1}(x;x)\Gamma_B\right] - 2\,\mathrm{Tr}\left[D^{-1}(x;y)\Gamma_A D^{-1}(y;x)\Gamma_B\right]
\end{aligned} \tag{3.94}$$

where α_i and β_i represent Dirac spin indices, and c_i color indices. All repeated indices

can be understood as summed over. In the fourth step, I used Wick's theorem, given in Eqs. (3.43) and (3.51). The graphical representation of Eq. (3.94) is shown in Fig. 3.8. Panel (A) in Fig. 3.8 represents disconnected diagram (the left-hand side in Eq. (3.94)), and panel (B), connected diagram (the right-hand side in Eq. (3.94)).

3.5.2 Calculation of the quark propagator

In the previous subsection, I discussed how to construct meson interpolators and correlators. The essential task is to calculate the correlators numerically. They include quark propagators, so calculating the inverse Dirac matrices, D^{-1}, is the key required task.

Consider a meson interpolator given in Eq. (3.93) in the more general form,

$$\mathcal{O}(t,x) = \sum_{\boldsymbol{x}_1\boldsymbol{x}_2} F(\boldsymbol{x}_1,\boldsymbol{x}_2|t,\boldsymbol{x})\bar{\psi}(t,\boldsymbol{x}_1)\Gamma\psi(t,\boldsymbol{x}_2)\,. \tag{3.95}$$

where F is a function depending on the lattice sites, $\boldsymbol{x}_1$, $\boldsymbol{x}_2$, and $\boldsymbol{x}$, and specific time slice, t. To be specific, let us write $F(\boldsymbol{x}_1,\boldsymbol{x}_2|t,\boldsymbol{x}) = S_A(\boldsymbol{x},\boldsymbol{x}_1)^\dagger S_B(\boldsymbol{x},\boldsymbol{x}_2)$. If S_A and S_B have the same functional form as $S_p(\boldsymbol{x},\boldsymbol{x}_i)$:

$$S_B(\boldsymbol{x},\boldsymbol{x}_i)^a_\alpha = S_A(\boldsymbol{x},\boldsymbol{x}_i)^a_\alpha = S_p(\boldsymbol{x},\boldsymbol{x}_i)^a_\alpha = \delta^{(3)}(\boldsymbol{x}-\boldsymbol{x}_i)\delta_{\alpha,\alpha_0}\delta_{a,a_0}\,, \tag{3.96}$$

then, the interpolator $\mathcal{O}$ reduces to the original interpolator form in Eq. (3.93). Here, the source S_p is called a "point source". In fact, the function F does not need to be a product of two point sources. If we are mostly interested in extracting the ground-state mass, to get a better signal-to-noise ratio, we need to suppress radially excited states as well as all momentum excited states. To achieve this, one can implement F as an approximate hadronic ground-state wave function. Since we do not know the wavefunction precisely, often we simply use Gaussian. In any case, F is then called a "smearing function".

Let us consider a connected meson correlator in Eq. (3.94) in which smearings are done at both the source and sink. It can be written as

$$\begin{aligned}\left\langle \mathcal{O}_A(t,\boldsymbol{y})\mathcal{O}_B^\dagger(0,\boldsymbol{x})\right\rangle \;=\; -\sum_{\boldsymbol{x}_1\boldsymbol{x}_2\boldsymbol{y}_1\boldsymbol{y}_2} \mathrm{Tr}\,\big[&F(\boldsymbol{x}_1,\boldsymbol{x}_2|0,\boldsymbol{x})D^{-1}(0,\boldsymbol{x}_1;t,\boldsymbol{y}_1)\Gamma_A \\ &\times F(\boldsymbol{y}_1,\boldsymbol{y}_2|t,\boldsymbol{y})^\dagger D^{-1}(t,\boldsymbol{y}_2;0,\boldsymbol{x}_2)\Gamma_B\big]\,.\end{aligned} \tag{3.97}$$

Here, if we write $F(\boldsymbol{x}_1,\boldsymbol{x}_2|t,\boldsymbol{x})$ is a product of two sources,

$$F(\boldsymbol{x}_1,\boldsymbol{x}_2|t,\boldsymbol{x}) = S_A(\boldsymbol{x},\boldsymbol{x}_1)^\dagger S_B(\boldsymbol{x},\boldsymbol{x}_2)\,, \tag{3.98}$$

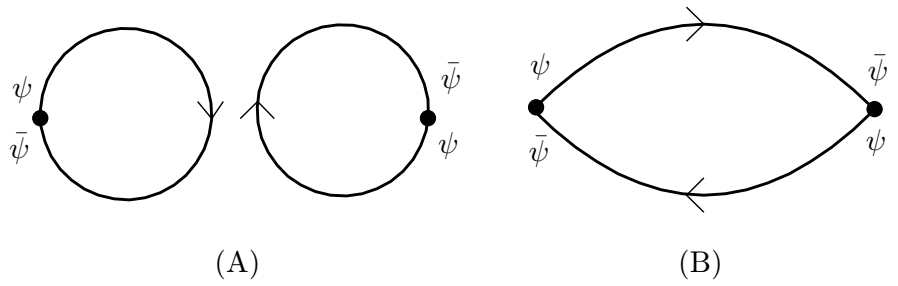

Figure 3.8. Diagrammatic expression for disconnected (A) and connected (B) meson correlators in Eq. (3.94). Each ψ or $\bar{\psi}$ represents the quark field operator creating or annihilating a quark. Each line represents the quark propagator.

then, Eq. (3.97) becomes

$$\left\langle \mathcal{O}_A(t,\boldsymbol{y})\mathcal{O}_B^\dagger(0,\boldsymbol{x})\right\rangle = -\,\mathrm{Tr}\left\langle \sum_{\boldsymbol{x}_2\boldsymbol{y}_2}\left[S_B(\boldsymbol{y}_2;\boldsymbol{y})^\dagger D^{-1}(t,\boldsymbol{y}_2;0,\boldsymbol{x}_2)S_B(\boldsymbol{x}_2;\boldsymbol{x})\right]\Gamma_B \right. \\ \left. \times \sum_{\boldsymbol{x}_1\boldsymbol{y}_1}\left[S_A(\boldsymbol{y}_1,\boldsymbol{y})^\dagger D^{-1}(t,\boldsymbol{y}_1;0,\boldsymbol{x}_1)S_A(\boldsymbol{x}_1;\boldsymbol{x})\right]^\dagger \Gamma_A\right\rangle . \quad (3.99)$$

Therefore, to get the meson correlator, we need to evaluate

$$\sum_{\boldsymbol{x}_i} D^{-1}(t,\boldsymbol{y}_j;0,\boldsymbol{x}_i)S(\boldsymbol{x}_i;\boldsymbol{x}), \quad (3.100)$$

where for $i=1$, $S\equiv S_A$, and for $i=2$, $S\equiv S_B$, respectively.

Before discussing how to solve this equation numerically, let us go over another type of source called "stochastic wall source", which can be used for gaining better statistics and assigning a specific momentum to the source. The stochastic sources are constructed on the color space with random orientation on a single time slice. They can be considered as the collection of point sources distributed on the entire lattice spatial sites, but satisfying the following relation:

$$\sum_{j}^{N_R}\xi_j^{a\dagger}(\boldsymbol{x}_1)\xi_j^b(\boldsymbol{x}_2) \to \delta(\boldsymbol{x}_1-\boldsymbol{x}_2)\delta^{ab}\,, \qquad \text{for } N_R\to\infty \quad (3.101)$$

where a and b indicate color indices. N_R is the number of stochastic sources, so that if N_R is large, it puts the sources of the quark and antiquark fields at the same location. One can include momentum by inserting the Fourier factor, $e^{i\boldsymbol{p}\cdot\boldsymbol{x}}$,

$$\sum_{\boldsymbol{x}} e^{i\boldsymbol{p}\cdot\boldsymbol{x}}\xi(\boldsymbol{x})\,. \quad (3.102)$$

Therefore, in Eq. (3.98), if we replace $S_B(\boldsymbol{x}, \boldsymbol{x}_2)$ by $e^{i\boldsymbol{p}\cdot\boldsymbol{x}_2}\xi(\boldsymbol{x}_2)$, we calculate the quark propagator with momentum $\boldsymbol{p}$,

$$\sum_{\boldsymbol{x}_2} D^{-1}(\boldsymbol{x}, t; \boldsymbol{x}_2, 0) \left[e^{ip\cdot\boldsymbol{x}_2}\xi(\boldsymbol{x}_2)\right] , \tag{3.103}$$

where the square bracket in Eq. (3.103) is taken as the source term in solving the propagator.

Finally, to calculate the meson correlator, we need to solve $X = D^{-1}S$, numerically, where X is a desired solution and S is the source. D represents the Dirac matrix, which is a large sparse matrix with many vanishing entries and F is a source. To solve the equation, $DX = F$, we use a stabilized biconjugate gradient solver (Bi-CG) for clover propagators [42] and a standard conjugate gradient solver (CG) for asqtad and HISQ propagators [43] in our lattice simulations.

3.5.3 Lattice ensemble

An expectation value of an observable, $\langle O \rangle$, can be obtained via the path integral shown in Eq. (3.50),

$$\langle \mathcal{O} \rangle = \frac{1}{Z} \int \mathcal{D}[U] e^{-S_G[U]} \det[D(U)] \mathcal{O}_F[U] , \tag{3.104}$$

where, again, $\mathcal{O}_F[U]$ is the fermionic path integral as discussed in Sec. 3.3.2. $\mathcal{O}_F[U]$ could be a meson correlator resulting from integrations over only the fermion part of the path integral, $\langle ... \rangle_F$.

In analogy with the discussion in Sec. 3.1, the gauge field part of the path integral can be done by generating a large number of gauge field configurations, $U^{(i)}(x)$, where $i = 1, ..., N_{cf}$. As seen in Eq. (3.104), the gauge field configurations must be randomly distributed with probabilities,

$$P[U^{(i)}] = \frac{1}{Z} e^{-S_G[U]} \det[D] . \tag{3.105}$$

Then, finally, we can calculate the average value of an observable $\mathcal{O}$,

$$\overline{\mathcal{O}} = \frac{1}{N_{cf}} \sum_{i=1}^{N_{cf}} \mathcal{O}_i . \tag{3.106}$$

where $\mathcal{O}_i$ is an expectation value of an observable $\mathcal{O}$ calculated on i-th configuration. Its variance is given by

$$\sigma^2 = \frac{\overline{\mathcal{O}^2} - \overline{\mathcal{O}}^2}{N_{cf}} . \tag{3.107}$$

Note that the probability (or weighting function), $P[U^{(i)}]$, includes the fermion determinant that describes the fermionic "Dirac sea" – the virtual pairs of quarks and antiquarks

that are created and annihilated. It also includes any valence quark propagators. Including sea quark effects is expensive. Therefore, in early lattice calculation, most of results had been acquired by setting $\det[D(U)] = 1$ as an approximation. This approximation is called "quenched approximation". However, the computing technology has developed enough to include the full effects of $\det[D(U)]$. This type of lattice calculation is called a "full dynamical lattice QCD calculation". In our simulation, we perform a full dynamical lattice QCD calculation.

The long sequence of gauge field configurations form a Markov chain, *i.e.,* each configuration is correlated to some extent with the previous one, because each new configuration is generated from the previously generated configuration. With the desired probability, the initial gauge field configuration, $\phi^{(0)}$ is generated through a sequence of random updates, called "thermalizing". The next gauge configurations are generated with the same way, but from the previous configuration. Thus, they form a chain, $\phi^{(0)}$, $\phi^{(1)}$, $\phi^{(2)}$ ... There are various methods to generate these random field configuration, including the Metropolis algorithm [44], the heat bath method, and the molecular dynamics [45, 46] method.

This Markov chain correlation is called an "autocorrelation". It must be taken into account to get an unbiased variance. There are various methods to remove the autocorrelation effect. Here, I introduce the "blocking method" [24] as an example. Suppose, we measure an observable on N successive configurations in the chain and group the data into blocks, such that each block includes n_b successive measurements. We get the average of observable $\langle X \rangle$ on each block represented by B_i for the i-th block. Then, the variance of the mean over all blocks is

$$\sigma^2_{\text{mean}}(n_b) = \frac{1}{M_b(M_b-1)} \sum_{i=1}^{M_b} (B_i - \langle X \rangle)^2 \,, \tag{3.108}$$

where $M_b = N/n_b$ is the number of blocks. As the block size n_b increases, the autocorrelation effect is reduced, *i.e.,* $\sigma^2_{\text{mean}}(n_b)$ increases to its asymptotic, unbiased value. Therefore, if we have enough measurements for the variance $\sigma^2_{\text{mean}}(n_b)$ to be saturated at certain n_b, then the saturated variance is the real variance of the data. However, if it is not saturated, one can extrapolate $n_b \to \infty$ within given data. As the n_b increases, the variance, $\sigma^2_{\text{mean}}(n_b)$, converges to the real variance, σ^2_{mean}, by the following relation:

$$\sigma^2_{\text{mean}}(n_b) = \sigma^2_{\text{mean}} - \frac{\alpha}{n_b} \,, \tag{3.109}$$

where σ^2_{mean} and α are positive fit parameters and $1/n_b$ is an independent variable. Therefore, by linearly extrapolating $1/n_b \to 0$, one can get the unbiased variance.

3.5.4 Fitting correlators

The meson correlator, $C(t)$ in Eq. (3.87) can be expanded in a multiexponential form as in Eq. (3.90). Therefore, our fit function should be

$$f(t) = \sum_{n=1}^{N} A_n \exp(-E_n t)\,, \tag{3.110}$$

where N is the maximum number of exponentials which could be determined by the fit range and states of interest. If we are interested in the ground state of a meson, then we set the fit range, $[t_{min}, t_{max}]$, with a sufficiently high t_{min} to suppress the contribution of higher excited states. However, if we set it too high, then we may lose useful information available at low times. To set a proper t_{min}, we often start by looking for a plateau in the effective mass as a function of t. As we reduce t_{min}, we may need to include more exponential terms to get a good chi square.

3.5.5 Variational method

The variational method [47, 48] is widely used for determining the hadron spectrum in lattice calculations. It is particularly useful for studying excited states. Consider the hadronic correlator matrix propagating in Euclidean space-time from 0 to t,

$$C_{ij}(t) = \langle 0|\mathcal{O}_i(t)\mathcal{O}_j^{\dagger}(0)|0\rangle\,, \tag{3.111}$$

where we are now dealing with correlator matrix generated by a set of hermitian interpolating operators, $\mathcal{O}_i(t)$, with the same quantum numbers for $i = 1...N$, where N is the number of interpolators. Each $\mathcal{O}_i(t)$ varies according to the QCD hamiltonian H derived from an action with a single time-step transfer matrix $T = \exp(-H)$. Again, we assume that the time extent of the lattice is sufficiently large that we may consider only propagation forward in time. Then, the eigenvalues of the transfer matrix are simply given by e^{-E_n} and the correlator can be expressed in the multiexponential form

$$C_{ij}(t) = \sum_{n=1}^{\infty} \langle 0|\mathcal{O}_i|n\rangle e^{-E_n t} \langle n|\mathcal{O}_j^{\dagger}|0\rangle\,, \tag{3.112}$$

or in matrix form

$$C(t) = Z T^t Z^{\dagger}\,, \tag{3.113}$$

where Z is a matrix with an infinite number of rows (labeled by the eigenvalues) and N columns (labeled by the interpolating operators), which can be expressed as

$$Z_{i,n} = \langle 0|\mathcal{O}_i|n\rangle\,. \tag{3.114}$$

With a finite set of interpolators, we cannot identify an infinite set of eigenvalues. We start by truncating the infinite sum in Eq. (3.87) to a finite sum for $n \in [1, N]$ and introduce at least N linearly independent interpolating operators $\mathcal{O}_i(t)$. Then, by multiplying Eq. (3.113) by $(Z^\dagger)^{-1}$ and inserting $I = C(t_0)C(t_0)^{-1}$, we can reduce Eq. (3.113) to the generalized eigenvalue problem (GEVP).

$$C(t)(Z^\dagger)^{-1} = C(t_0)C(t_0)^{-1}ZT^t \tag{3.115}$$

$$= C(t_0)(Z^\dagger)^{-1}T^{t-t_0}\,. \tag{3.116}$$

where T^t is diagonal matrix. For the n th row of the transfer matrix, we can find the n th eigenvalue by solving the GEVP

$$C(t)u_n = \lambda_n(t, t_0)C(t_0)u_n\,, \tag{3.117}$$

where u_n is the nth column of the matrix $(Z^\dagger)^{-1}$, and the eigenvalues of the GEVP behave as [47]

$$\lambda_n(t, t_0) \propto e^{-E_n(t-t_0)}(1 + O(e^{-t\Delta E_n}))\,, \tag{3.118}$$

At fixed t_0, ΔE_n is the distance of E_n to the closest energy level, while for the special case of $t < 2t_0$ and a basis of N correlators, ΔE_n is given by [48],

$$\Delta E_n = E_{N+1} - E_n\,. \tag{3.119}$$

Therefore, at large time separations, the eigenvalues are dominated by a single state, allowing for stable two parameter fits to the eigenvalues. The largest eigenvalue decays with the energy of the ground state, the second largest eigenvalue with the energy of the first excited state, and so on.

3.5.6 Continuum and chiral extrapolation on the lattice

As we discussed in Sec. 3.4, discretization effects are inevitable in the lattice QCD calculation. The correction term of the measured hadron mass, M, with the Wilson lattice action is of $O(a)$:

$$M(a) = M_{phys}(1 + O(a))\,. \tag{3.120}$$

However, the clover-improved action reduces this dependence to $O(a^2)$. Therefore, to overcome this lattice artifact, we need to perform lattice simulations on a number of different ensembles that are characterized by different lattice spacings a. Then, we extrapolate $M(a)$ to the continuum, $a \to 0$, to get M_{phys}. This is called a "continuum extrapolation".

On the lattice, it is expensive to simulate at the physical light quark masses, due to the high cost of calculating $D^{-1}(U)$. Often numerical simulation results are obtained for somewhat larger, unphysical quark masses. Here, the "light quarks" include both valence light quarks and sea quarks. The valence light quarks are characterized by the quark fields in the meson interpolators and the sea quarks result from the fermion determinant $\det D[U]$, given in Eq. (3.47). However, as we reduce the light quark masses, the measured hadron masses are closer to the physical hadron masses. Therefore, as we do the continuum extrapolation, if we run lattice simulations on a number of different ensembles characterized by different light quark masses, and extrapolate, then we are able to get M_{phys}. This extrapolation is often aided by chiral perturbation theory, which specifies an explicit dependence on light quark masses, so the extrapolation is called the "chiral" extrapolation.

3.6 Finite volume method

In this section, I provide a brief introduction to Lüscher's finite volume method [49,50], which will be used for the analysis of the $X(3872)$ in Chap. 6. At finite volume, every observable is affected by finite size effects, not only multiparticle but also single-particle states. On the lattice, one may consider this to be a lattice artifact that one should eliminate. However, in fact, from finite volume effects, we can extract useful information about the scattering states, such as the phase shift and scattering length. Here, we discuss finite volume effects and how one can extract scattering information from them to determine the characteristic of multiparticle states, *e.g.,* resonances or bound states.

Consider two-particle states in the center-of-mass frame. The total energy of the system is given by

$$E_{AB}(\boldsymbol{p}) = \sqrt{m_A^2 + \boldsymbol{p}^2} + \sqrt{m_B^2 + \boldsymbol{p}^2}\,, \tag{3.121}$$

where $\boldsymbol{p}$ is the relative momentum of two particles labeled by A and B. In a finite box L^3 on the lattice, by imposing periodic boundary conditions, all momenta are quantized and can be labeled by an integer $\boldsymbol{n}(\in \mathbb{Z}^3)$ as $\boldsymbol{p}_n$. If two particles do not interact with each other, then $\boldsymbol{p}_n$ is simply given by $2\pi\boldsymbol{n}/L$. However, if they do interact, the momentum $\boldsymbol{p}$ is no longer a multiple of integer $\boldsymbol{n}$. In the finite volume method, the basic assumption is that the interaction range is finite and smaller than L,

$$V(\boldsymbol{r}) = 0 \qquad\qquad \text{for} \;\; |\boldsymbol{r}| > R\,, \tag{3.122}$$

where $\boldsymbol{r} = \boldsymbol{r}_A - \boldsymbol{r}_B$ and R is the interaction range and $R < L/2$. In the exterior region, the two-particle wave function satisfies

$$H_{\text{free}}\psi_{\text{free}}(r_A, r_B) = E\psi_{free}(r_A, r_B)\,. \tag{3.123}$$

In quantum mechanics, with $H_{\text{free}} = \boldsymbol{p}^2/2m$, we can describe the scattering process with a wave function that combines incoming and outgoing waves,

$$\psi(\boldsymbol{r}) = \frac{1}{(2\pi)^{3/2}}\left[e^{i\boldsymbol{p}\cdot\boldsymbol{r}} + \frac{e^{ipr}}{r}f(\boldsymbol{p}', \boldsymbol{p})\right] \tag{3.124}$$

where the incoming wave is a plane wave and the outgoing wave is a plane wave and a spherical wave with amplitude $f(\boldsymbol{p}, \boldsymbol{p}')$. By inserting the expansion of a plane wave in terms of spherical waves,

$$e^{i\boldsymbol{p}\cdot\boldsymbol{r}} = 4\pi\sum_{l=0}^{\infty}\sum_{m=-l}^{l} i^l j_l(pr)Y_{lm}^*(\hat{\boldsymbol{p}})Y_{lm}(\hat{\boldsymbol{r}})\,, \tag{3.125}$$

into Eq. (3.124), and without loss of generality, by choosing the coordinate system such that the $\boldsymbol{p}$ is aligned parallel to the positive z-axis so that

$$Y_{lm}(\hat{\boldsymbol{p}}) = \sqrt{\frac{2l+1}{4\pi}}\delta_{m0}\,, \tag{3.126}$$

we obtain the new form of the wave function, $\psi(\boldsymbol{r})$, at a large distance, r,

$$\psi(\boldsymbol{r}) \xrightarrow{\text{large } r} \frac{1}{(2\pi)^{3/2}}\sum_l (2l+1)\frac{P_l(\cos\theta)}{2ip}\left[[1+2ipf_l(p)]\,\frac{e^{ipr}}{r} - \frac{e^{-i(pr-l\pi)}}{r}\right] \tag{3.127}$$

where $P_l(\cos\theta)$ is a Legendre polynomial, and $f_l(p)$ is the partial-wave amplitude,

$$f(\boldsymbol{p}', \boldsymbol{p}) = f(\theta) = \sum_{l=0}^{\infty}(2l+1)f_l(p)P_l(\cos\theta)\,. \tag{3.128}$$

In this form, it is clearer to see the effects of the potential, $V(\boldsymbol{r})$. At a large distance r, without the scatterer, the wave function becomes simply the sum of an incoming wave, $e^{-i(pr-l\pi)}/r$ and an outgoing wave, e^{ipr}/r. By contrast, with scattering, the outgoing wave amplitude changes only as

$$1 \to 1 + 2ipf_l(p)\,. \tag{3.129}$$

Now, one can define the scattering matrix as

$$S_l(p) \equiv 1 + 2ipf_l(p)\,, \tag{3.130}$$

and, as a consequence of probability conservation, S_l must satisfy

$$|S_l(p)| = 1\,. \tag{3.131}$$

As a result, in elastic scattering, the only change in the wave function at a large distance is the phase of the outgoing waves. Therefore, by defining this phase to be $2\delta_l$, one can write the scattering matrix

$$S_l = e^{2i\delta_l}\,, \tag{3.132}$$

where l denotes the angular momentum of the outgoing wave, and δ_l is called the "scattering phase shift", which must be real for elastic scattering. Then, from Eqs. (3.130) and (3.132), one can write the partial-wave amplitude $f_l(p)$ in terms of the phase shift,

$$f_l = \frac{e^{2i\delta_l} - 1}{2ip} = \frac{e^{i\delta_l}\sin\delta_l}{p} = \frac{1}{p\cot\delta_l - ip}\,. \tag{3.133}$$

Causality requires that $p\cot\delta_l$ be a real analytic function of p^2 in the vicinity of $p = 0$. Therefore, the effect of the interaction is taken into account by a momentum-dependent phase shift $\delta_l(p)$, acquired in the interaction region.

Returning to the finite volume, first, to simplify the situation, let us discuss a $1+1$ dimensional system of finite and periodic spatial extension L, but infinite time extension. In 1+1 dimensions, both incoming and outgoing wave functions outside the interaction range are simple plane waves $\sim e^{ipx}$. Therefore, the phase shift comes in as $\psi(x) \sim e^{ipx+2i\delta(p)}$. From the periodic boundary condition, the plane wave function at $x = L$ should equal its value at $x = 0$, *i.e.,* $\psi(L) = \psi(0)$. If there is no interaction, the phase shift becomes zero. Thus, wave function satisfies the periodic boundary condition

$$e^{ip\cdot L} = e^{ip\cdot 0} = 1\,, \tag{3.134}$$

where the momentum is simply quantized as $2\pi/L$. However, if there is an interaction, the phase shift has nonzero value. Therefore, now, the periodic boundary condition becomes

$$e^{ip\cdot L+2i\delta(p)} = e^{ip\cdot 0} = 1\,. \tag{3.135}$$

This gives rise to the functional form of the phase $\delta(p_n)$:

$$\delta(p_n) = n\pi - p_n L \tag{3.136}$$

On the lattice, the momenta can be obtained from the energy values of the two-particle states determined from correlators or the correlation matrix, *i.e.,* the variational method. For given L, one computes the discrete energy levels of two particles labeled A and B: $E_{AB}^{(0)}$, $E_{AB}^{(1)}$, $E_{AB}^{(2)}$, $\cdots$. Then, the values of $\boldsymbol{p}_n$ can be found by using the dispersion relation given by Eq. (3.121). Therefore, from the discrete energies in a finite interval, we get the infinite-volume phase shift at the corresponding discrete values of p_n. If we change L, we

get other values of the phase shift at other p_n. In this way, we can map out the phase shift in the region near $p = 0$.

In $3+1$ dimensions, the relation between the phase shift and momentum becomes more complicated. To get the relation between the phase shift and momentum, I follow the steps in Ref. [50], where a more rigorous treatment is found.

The eigenvalue equation, Eq. (3.123), in the exterior region can be rewritten as the well-known Helmholtz equation,

$$(\nabla^2 + p^2)\psi(\boldsymbol{r}) = 0 \qquad\qquad |\boldsymbol{r}| > R\,. \tag{3.137}$$

As mentioned previously, only the phase shift, $\delta(p)$, is needed to characterize the effect of interaction within $|\boldsymbol{r}| < R$. At infinite volume, the solution of Eq. (3.137) is given by

$$\psi(\boldsymbol{r}) = \sum_{l,m} c_{lm} Y_{lm}(\theta,\phi)\left[\alpha_l(p) j_l(pr) + \beta_l(p) n_l(pr)\right]\,, \tag{3.138}$$

where $j_l(pr)$ and $n_l(pr)$ are spherical Bessel functions. The phase shift $\delta_l(p)$ in the continuum is defined through the ratio of the amplitudes of the outgoing wave, $j_l - in_l$, to the amplitude of the incoming wave, $j_l + in_l$,

$$e^{2i\delta_l(p)} \equiv \frac{\alpha_l(p) + i\beta_l(p)}{\alpha_l(p) - i\beta_l(p)}\,. \tag{3.139}$$

One can use the same phase shift definition in finite volume; however, the wave function has a more complex form due to the boundary condition,

$$\psi(\boldsymbol{r} + \boldsymbol{n}L) = \psi(\boldsymbol{r}) \qquad \text{for all } \boldsymbol{n} \in \mathbb{Z}^3\,. \tag{3.140}$$

Also, the potential $V(\boldsymbol{r})$ satisfies the periodic relation,

$$V_L(\boldsymbol{r}) = \sum_{\boldsymbol{n}\in\mathbb{Z}^3} V(|\boldsymbol{r} + \boldsymbol{n}L|)\,. \tag{3.141}$$

Now, the Green function satisfying both the Helmholtz equation and the periodic boundary condition is

$$G(\boldsymbol{r}; \boldsymbol{p}^2) = L^{-3} \sum_{\boldsymbol{k}\in\Gamma} \frac{e^{i\boldsymbol{p}\boldsymbol{r}}}{\boldsymbol{p}^2 - \boldsymbol{k}^2}\,, \tag{3.142}$$

where the sum runs over the lattice. With this Green function, we can define linearly independent solutions,

$$G_{lm}(\boldsymbol{r}; \boldsymbol{p}^2) = \mathcal{Y}_{lm}(\nabla) G(\boldsymbol{r}; p^2)\,, \tag{3.143}$$

where ∇ is the gradient and $\mathcal{Y}_{lm}$ is the harmonic polynomial,

$$\mathcal{Y}_{lm}(\boldsymbol{r}) = \boldsymbol{r}^l Y_{lm}(\theta,\phi)\,. \tag{3.144}$$

The solutions G_{lm} form a complete basis as shown in Ref. [50], and the wave function $\psi(\boldsymbol{r})$ can be expanded in terms of them :

$$\psi(\boldsymbol{r}) = \sum_{lm} v_{lm} G_{lm}(\boldsymbol{r}; \boldsymbol{p}^2) \ , \qquad |\boldsymbol{r}| > R \tag{3.145}$$

Now, the phase shifts δ_l are related to the incoming j_l and outgoing spherical waves as in the infinite volume in Eq. (3.139). Thus, we need to express G_{lm} in terms of j_l and n_l [50],

$$G_{lm}(\boldsymbol{r}; \boldsymbol{p}^2) = \frac{(-)^l}{4\pi} p^{l+1} \left\{ Y_{lm}(\theta, \phi) n_l(pr) + \sum_{l'=0}^{\infty} \sum_{m'=-l'}^{l'} \mathcal{M}_{lm,l'm'} Y_{l'm'}(\theta, \phi) j_{l'}(pr) \right\} . \tag{3.146}$$

The matrix $\mathcal{M}_{lm,l'm'}$ plays a crucial role in the analysis of the two-particle spectrum in finite volume. The general solution in the exterior region $\psi(\boldsymbol{r})$ in Eq. (3.145) is obtained by inserting Eq. (3.146) into Eq. (3.145) and by comparing this with Eq. (3.138) in order to extract the phase shifts defined in Eq. (3.139). *e.g.,*

$$\begin{aligned} \psi(\boldsymbol{r}) &= \sum_{lm} v_{lm} \frac{(-)^l}{4\pi} p^{l+1} \left\{ n_l(pr) Y_{lm}(\theta, \phi) + \sum_{l'm'} \mathcal{M}_{lm,l'm'} j_{l'}(pr) Y_{l'm'}(\theta, \phi) \right\} & (3.147) \\ &= \sum_{l,m} c_{lm} Y_{lm}(\theta, \phi) \left\{ \alpha_l(p) j_l(pr) + \beta_l(p) n_l(pr) \right\} . & (3.148) \end{aligned}$$

Therefore, from the coefficients $Y_{lm} n_l$ and $Y_{lm} j_l$, we get two relations,

$$v_{lm} \frac{(-)^l}{4\pi} p^{l+1} = c_{lm} \beta_l(p) \ , \qquad \sum_{l'm'} v_{l'm'} \frac{(-)^{l'}}{4\pi} p^{l'+1} \mathcal{M}_{lm,l'm'} = c_{lm} \alpha_l(p) \tag{3.149}$$

and v_{lm} can be formed from the first relation and inserted into the second, resulting in

$$\sum_{l'm'} c_{l'm'} \left[\beta_{l'}(p) \mathcal{M}_{lm,l'm'} - \alpha_{l'}(p) \delta_{ll'} \delta mm' = 0 \right] . \tag{3.150}$$

A nontrivial solution $c_{l'm'}$ exists only if

$$\det(B\mathcal{M} - A) = 0 \, , \tag{3.151}$$

where the matrices A and B are defined as diagonal matrices related to coefficients α_l and β_l,

$$\begin{aligned} A_{lm,l'm'} &\equiv \alpha_l(p) \delta_{ll'} \delta_{mm'} & (3.152) \\ B_{lm,l'm'} &\equiv \beta_l(p) \delta_{ll'} \delta_{mm'} \, . & (3.153) \end{aligned}$$

Finally, we can replace the phase shift expression in the continuum, Eq. (3.139), with the finite volume expression satisfying periodic boundary condition,

$$e^{2i\delta_l(p)} = \frac{A + iB}{A - iB} \, . \tag{3.154}$$

By dividing Eq. (3.151) by $\det(A-iB)$, we can obtain the final relation between the diagonal matrix $e^{2i\delta}$ and nondiagonal matrix M,

$$\det[e^{2i\delta}(\mathcal{M}-i)-(\mathcal{M}+i)]=0\,, \tag{3.155}$$

where $[e^{2i\delta}]_{lm,l'm'} \equiv e^{2i\delta_l(p)}\delta_{ll'}\delta_{mm'}$. Eq. (3.155) is the essential expression of the phase shift relation and relates the energy E measured on the lattice to the unknown phase shifts $\delta_l(p)$ via the matrix elements $\mathcal{M}_{lm,l'm'}$.

The final result can be obtained by applying the differential operator $\mathcal{Y}(\nabla)$ to the series $G(\boldsymbol{r};p^2)$ and expanding G_{lm} in terms of j_l and n_l in Eq. (3.146),

$$\mathcal{M}_{lm,l'm'} = \frac{(-)^l}{\pi^{\frac{3}{2}}}\sum_{j=|l-l'|}^{l+l'}\sum_{s=-j}^{j}\frac{i^j}{q^{j+1}}\mathcal{Z}_{js}(1;q^2)C_{lm,js,l'm'} \quad , \tag{3.156}$$

$$C_{lm,js,l'm'} = (-)^{m'}i^{l-j+l'}\sqrt{(2l+1)(2j+1)(2l'+1)}\begin{pmatrix} l & j & l' \\ 0 & 0 & 0\end{pmatrix}\begin{pmatrix} l & j & l' \\ m & s & -m'\end{pmatrix}, \tag{3.157}$$

where $C_{lm,js,l'm'}$ is expressed in terms of the Wigner 3j-symbols and $\mathcal{Z}_{js}$ is a generalized zeta function,

$$\mathcal{Z}_{lm}(s;q^2)=\sum_{\boldsymbol{n}\in\mathbb{Z}^3}\frac{\mathcal{Y}_{lm}(\boldsymbol{n})}{(\boldsymbol{n}^2-q^2)^{-s}} \quad , \qquad \boldsymbol{q}=\frac{L}{2\pi}\boldsymbol{p}\,. \tag{3.158}$$

The following properties generally hold:

$$\mathcal{M}_{lm,l'm'}=\mathcal{M}_{l'm',lm}=\mathcal{M}_{l-m,l'-m'}\,. \tag{3.159}$$

For the practical purpose of the $X(3872)$ study discussed in Chap 6, we will use only the formula of the S-wave phase shift, $l=0$ and $s=0$. However, $\mathcal{Z}_{00}$ is finite only for $s>3/2$, but the divergence is not physical, as it cancels in the difference between the finite and infinite volume result. Indeed, $\mathcal{Z}_{00}$ can be obtained by analytic continuation from $s>3/2$ to $s=1$.

From Eqs. (3.155) and (3.156), the phase shift formula for S-wave scattering can be expressed as

$$\tan\delta(\boldsymbol{p}_n)=\frac{\pi^{3/2}\sqrt{q^2}}{\mathcal{Z}_{00}(1;q^2)} \tag{3.160}$$

where $\mathcal{Z}_{00}(s;q^2)$ is an analytic continuation of the generalized Riemann zeta function,

$$\mathcal{Z}_{00}(s;q^2)=\frac{1}{\sqrt{4\pi}}\sum_{\boldsymbol{n}\in Z^3}(\boldsymbol{n}^2-q^2)^{-s}\,, \tag{3.161}$$

from the region $s>3/2$ to $s=1$.

Concerning the $X(3872)$ study, where we consider a possible weak bound state of the D and $\bar{D}^*$ mesons, we will need an expression for $\mathcal{Z}_{00}$ for $q^2 < 0$. $\mathcal{Z}_{00}$ can be efficiently calculated using the method described in Ref. [51] only for $q^2 > 0$; however, Ziwen Fu extended it to negative q^2 in the center of mass system [52],

$$\mathcal{Z}_{00}(s;q^2) = \sum_{\boldsymbol{n}\in\mathbb{Z}^3}{}' \frac{e^{-(\boldsymbol{n}^2-q^2)}}{\boldsymbol{n}^2-q^2} + \sum_{l=0}^{\infty} \frac{\pi^{3/2}}{l-1/2}\frac{q^{2l}}{l!} + \int_0^1 dt e^{q^2 t}\left(\frac{\pi}{t}\right)^{3/2} \sum_{\boldsymbol{n}\in\mathbb{Z}^3}{}' e^{-\pi^2\boldsymbol{n}^2/t}, \quad (3.162)$$

where $\sum'_{\boldsymbol{n}\in\mathbb{Z}^3}$ stands for a summation without $\boldsymbol{n} = \boldsymbol{0}$.

The S-wave scattering length a_0 is is defined through $a_0 = \lim_{p\to 0} \tan\delta_0(p)/p$. If the S-wave scattering length a_0 is sufficiently smaller than the spatial size L, one can make a Taylor expansion of the phase-shift formula Eq. (3.160) around $q^2 = 0$, and then the asymptotic solution of Eq. (3.160) can be obtained. Under the condition $p^2 \ll m_A^2$ and m_B^2, where m_A and m_B are the rest masses of two particles labeled A and B, the difference between the interaction energy and the sum of the rest masses of the two particles in $1/L$ is [49, 50]

$$\Delta E_{q^2=0} \approx -\frac{2\pi a_0}{\mu L^3}\left[1 + c_1\frac{a_0}{L} + c_2\left(\frac{a_0}{L}\right)^2 + \mathcal{O}\left(\frac{1}{L^3}\right)\right] \quad (3.163)$$

which corresponds to the energy shift of the lowest ($n = 0$) scattering state. The coefficients are $c_1 = -2.837297$ and $c_2 = 6.375183$, and μ is the reduced mass of two particles A and B. The finite volume method, so far, has been used in a great many calculations of hadron scattering lengths, *e.g.*, $\pi-\pi$, $\pi-K$, $\pi-N$, $\pi-D$, $K-D$, $K-N$, $D-D^*$, $N-N$ and J/ψ-hadron [51, 53–75].

CHAPTER 4

LOW-LYING CHARMONIUM STATES ON THE LATTICE

The main objective of this chapter is to present our dynamical lattice calculation of the low-lying charmonium spectrum [8, 9, 76]. In Sec. 4.1, I give a brief introduction to charmonium and the nonrelativistic potential model. In Sec. 4.2, I discuss the lattice methodologies to perform numerical simulation and analyze the resultant data. Finally, in the last section, I report on our lattice simulation results of low-lying charmonium spectrum and the corresponding analysis.

4.1 Introduction

Charmonium plays an important role in the application of QCD to hadron physics. Physically, charmonium is analogous to positronium. Positronium consists of an electron and positron interacting via the electromagnetic force, and charmonium, one charm quark, and one anti-charm quark interacting via the strong force. The states are characterized by the radial quantum number n and the relative angular momentum between quark and antiquark L. The orbital levels are labeled by $S, P, D, ...$ corresponding to $L = 0, 1, 2...$ The quark and antiquark couple to give the total spin, singlet $S = 0$ or triplet $S = 1$. S and L couple to give the total angular momentum J. The parity of a quark-antiquark state with angular momentum L is $P = (-1)^{L+1}$, and the charge conjugation quantum number is $C = (-1)^{L+S}$. The charmonium states are generally denoted by $^{2S+1}L_J$ with quantum numbers J^{PC}. Therefore, $L = 0$ states are $^1S_0$ and $^3S_0$ with $J^{\rm PC} = 1^{-+}$ and 1^{--}. $L = 1$ states are $^1P_1$, $^3P_0$, $^3P_1$, and $^3P_2$ with $J^{\rm PC} = 1^{+-}$, 0^{++}, 1^{++}, and 2^{++}, respectively. All of these states have their own names, as shown in the Fig. 4.1.

In the nonrelativistic quark model, based on the interpretation of the charmonium states as a bound state of a pair of quark and antiquark, typically, the energy levels are found by solving the nonrelativistic Shrödinger equation,

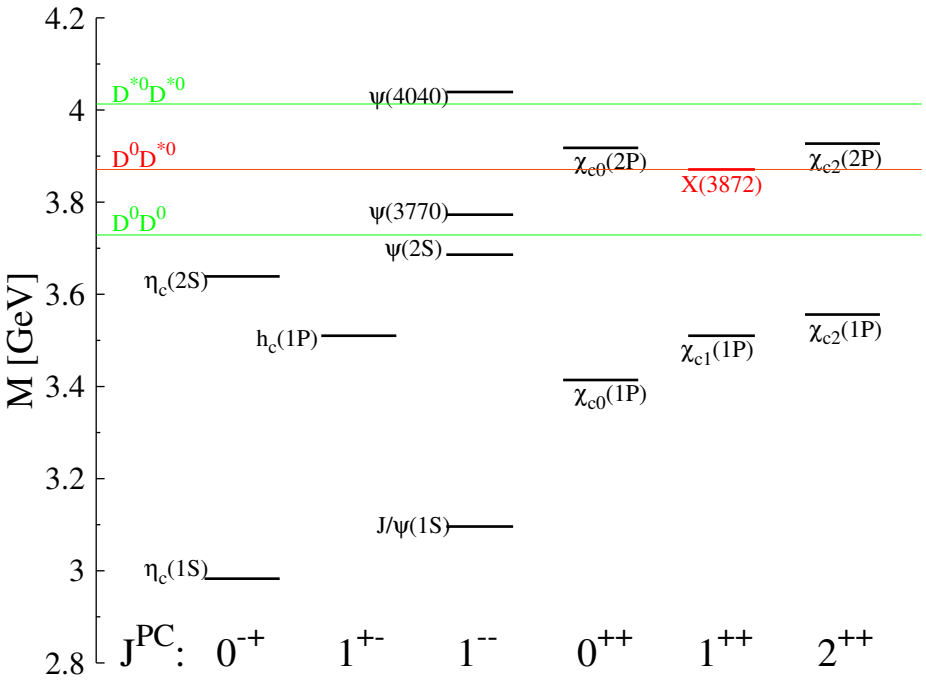

Figure 4.1. Charmonium spectrum from experiment [5]. Quantum number, $J^{\rm PC}$, varies along the horizontal axis and the energy value varies along the vertical axis. Each black bar represents the energy level of the corresponding charmonium state. The green lines represent the $M_{D^0} + M_{D^0}$, $M_{D^{*0}} + M_{D^{*0}}$ thresholds, *i.e.*, the "open charm" thresholds above which states decay into mesons containing a single charm quark or antiquark plus light quarks. The red line $M_{D^0} + M_{D^{*0}}$ is very close to the $X(3872)$ state energy level, which we discuss in Chap. 6.

$$\left(\frac{p^2}{2\mu_c} + V(\boldsymbol{r})\right)\psi(\boldsymbol{r}) = E\psi(\boldsymbol{r})\,, \tag{4.1}$$

where $\mu_c = m_c/2$ is the reduced mass of two charm quark masses. The potential $V(r)$ depends on the distance r between the quark and antiquark. Relativistic effects up to the order v^2/c^2 are treated as a perturbation. They come from relativistic terms in the potential as well as in the kinetic energy. Thus, we can write potential $V(r)$ as

$$V(r) = V^{(0)}(r) + \delta V^{(1)}_{\rm rel}(r)\,, \tag{4.2}$$

where $V^{(0)}(r)$ is the leading nonrelativistic potential and $\delta V^{(1)}_{\rm rel}(r)$ is the relativistic effect of order $(v/c)^2$.

At short distance, the shape of the potential, $V^{(0)}(r)$, is determined by the perturbation theory in QCD incorporating one gluon exchange. At long distance, it is determined by the phenomenology of confining quark interactions. One of the most developed models is the Cornell model [77–79], which builds upon the simplest potential,

$$V^{(0)}(r) = -\frac{4}{3}\frac{\alpha_S}{r} + br\,. \tag{4.3}$$

Here, the Coulomb term takes into account the attractive color-singlet quark-pair interaction resulting from the exchange of gluons at the lowest order, and the linear term builds in confinement with string tension, b.

Then, to first order in $(v/c)^2$, the potential $\delta V^{(1)}_{\rm rel}(r)$ in Eq. (4.2) includes spin-dependent interactions. There are three types of interactions terms,

$$\delta V^{(1)}_{\rm rel}(r) = V_{LS}(r)(\boldsymbol{L}\cdot\boldsymbol{S}) + V_T(r)\left[S(S+1) - \frac{3(\boldsymbol{S}\cdot\boldsymbol{r})(\boldsymbol{S}\cdot\boldsymbol{r})}{r^2}\right] + V_{SS}(r)\left[S(S+1) - \frac{3}{2}\right], \tag{4.4}$$

where $\boldsymbol{S} = (\boldsymbol{S}_Q + \boldsymbol{S}_{\bar{Q}})/2$, $S = \boldsymbol{\sigma}/2$, and $\boldsymbol{\sigma}$ is Pauli spin matrix. The spin-orbit, V_{LS}, and the tensor, V_T, terms describe the fine structure of the states, while the spin-spin term, V_{SS}, proportional to $2(\boldsymbol{s}_Q\cdot\boldsymbol{s}_{\bar{Q}}) = S(S+1) - \frac{3}{2}$, gives the hyperfine spin-singlet – triplet splittings. These terms can be directly derived from the standard Breit-Fermi expression [80] to order $(v/c)^2$ with the charm quark mass m_c [81] [1],

$$V_{SS}(r) = \frac{32\pi\alpha_S}{9m_c^2}\delta(r)\,, \tag{4.5}$$

$$V_{LS}(r) = \frac{2\alpha_S}{m_c^2 r^3} - \frac{b}{2m_c^2 r}\,, \tag{4.6}$$

$$V_T(r) = \frac{4\alpha_S}{m_c^2 r^3}\,. \tag{4.7}$$

Figure 4.2 gives an example of the charmonium spectrum resulting from the nonrelativistic quark model [6, 83] compared with the experiment [5]. The parameters used are $(\alpha_S, b, m_c, \sigma) = (0.5461, 0.1425\ \text{GeV}^2, 1.4794\ \text{GeV}, 1.0946\ \text{GeV})$. [2]

Despite the great success of the potential model in charmonium physics, there are obvious limitations, because the functional forms of the $Q\bar{Q}$ potentials, except at long distance, are basically deduced from a perturbative approach. The phenomenological spin-dependent potentials based on the perturbative method would be valid only at short distances and also in the heavy-quark-mass limit. This fact leads to uncertainties in predictions for the higher-lying states of heavy quarkonium in potential models. In addition, the newly discovered states above the open-charm threshold depicted in Sec. 6.2 are not simply explained as a conventional charmonium states.

[1] A more direct connection to QCD is established by the modern approach of effective field theory called potential nonrelativistic QCD (pNRQCD) [82]

[2] In Eq. (4.5), one can replace $\delta(r)$ with a Gaussian-smeared contact hyperfine interaction, $\bar{\delta}_\sigma(r) = (\sigma/\sqrt{\pi})^3 e^{-\sigma^2 r^2}$.

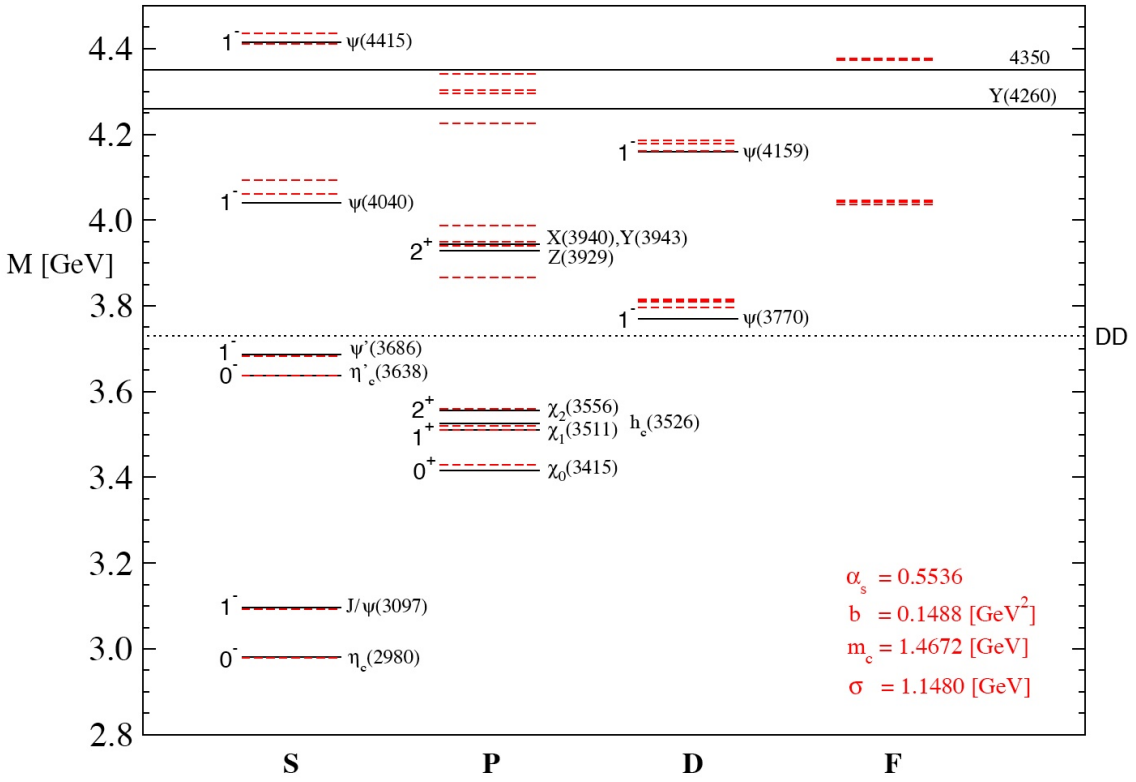

Figure 4.2. The energy level comparisons between experiment(solid black lines) and potential model prediction(red dotted lines) [6].

From this point of view, lattice QCD is the only available method for getting non-perturbative results from an *ab initio* calculation. In 2010, Dudek et al. [84] published results of a lattice QCD study of the excitation spectrum of charmonium as well as low-lying states. In order to access excited states, they introduced a large set of interpolating operators and used a variational method introduced in Chap. 3. These results are promising, but the calculation was done at only one lattice spacing, so a continuum and chiral extrapolation is not possible. Although lattice QCD enables us to perform *ab initio* calculations, the result is affected by lattice artifacts - finite lattice spacing, a, and light-quark masses heavier than physical. Thus, it is essential to take the continuum and chiral limit to get the physical values. That is the objective in our lattice calculation of the low-lying charmonium states [8,9,76]. In this chapter, I discuss the lattice methodology as well as the results from our high-precision calculation of the splittings between low-lying charmonium states at the physical point.

4.2 Methodology

As described in Chap. 3, to extract the hadron spectrum, one can use either direct correlator fitting or the variational method. In this study, we use the variational method, described in Sec. 3.5.5, to extract the charmonium energy levels. In the following subsections, I describe the observables we measure, the simulation setup, our method for constructing interpolating operators, the charm quark-mass corrections, and our chiral and continuum fits [8, 9].

4.2.1 Observables

To isolate the leading central potentials $V^{(0)}(r)$ introduced in Sec. 4.1, it is often convenient to discuss spin-averaged masses. For example, we define

$$M(\overline{1S}) = \frac{1}{4}\left(M(\eta_c) + 3M(J/\psi)\right) , \tag{4.8}$$

$$M(\overline{1^3P}) = \frac{1}{9}\left(M(\chi_{c0}) + 3M(\chi_{c1}) + 5M(\chi_{c2})\right) . \tag{4.9}$$

They are insensitive to the spin-orbit or the tensor interactions from Eqs. (4.6) and (4.7).

Now let us consider spin-dependent potentials, $\delta V^{(1)}_{\rm rel}(r)$. First, from Eq. (4.5), we notice that it is directly proportional to $|\psi(0)|^2$, and this implies that the hyperfine splitting between the ${}^3S_1$ and ${}^1S_0$ states should be proportional to the e^+e^- decay width of the vector ${}^3S_1$ resonance, which is also proportional to $|\psi(0)|^2$. Thus, it is interesting to consider the 1S-hyperfine splitting:

$$M(nS_{\rm HFS}) = M_{J/\psi} - M_{\eta_c} . \tag{4.10}$$

By contrast, the hyperfine splitting in the P-wave states should be extremely small because the wave function vanishes at the origin. Thus, for P-wave states, we consider the shifts between $M(\overline{1^3P})$ and each $M_{\chi_{cJ}}$. We can derive the following expression from Eq. (4.4) [81],

$$\delta M_{\chi_{c0}} = -2\langle V_{LS}\rangle + 2\langle V_T\rangle , \quad \delta M_{\chi_{c1}} = -\langle V_{LS}\rangle - \langle V_T\rangle , \quad \delta M_{\chi_{c2}} = \langle V_{LS}\rangle + \frac{1}{5}\langle V_T\rangle . \tag{4.11}$$

Then, for χ_{c0}, χ_{c1} and χ_{c2}, we get the two combination of splittings, spin-orbit, and tensor which we are interested in

$$M(nP_{\rm SO}) = \frac{1}{9}\left(5M(\chi_{c2}) - 2M(\chi_{c0}) - 3M(\chi_{c2})\right) \tag{4.12}$$

$$M(nP_{\rm T}) = \frac{1}{9}\left(3M(\chi_{c1}) - M(\chi_{c2}) - 2M(\chi_{c0})\right) \tag{4.13}$$

In summary, $M(nS_{\rm HFS})$ and $M(nP_{\rm T})$ are sensitive to spin-spin and tensor interactions, and $M(nP_{\rm SO})$, to spin-orbit interactions.

4.2.2 Simulation setup

The calculations have been performed with the (2+1)-flavor gauge configurations provided by the MILC collaboration [85], listed in Table 4.1. We use ensembles at five lattice spacings and two different light sea quark masses, simulated with the asqtad action [35–37]. The ensemble contains degenerate up and down sea quarks with masses approximately 1/5 and 1/10 the masses of the strange quark and with strange quark masses at close to their physical values, respectively. We use clover charm quarks within the Fermilab interpretation [86]. The charm-quark hopping parameter κ_c is tuned by matching the D_s kinetic mass to be equal to the physical D_s meson mass. Four source time slices per gauge configuration are used, for a total of ≈ 2000 to ≈ 4000 sources per ensemble.

4.2.3 Heavy quark formalism

I introduced the Wilson action in Chap. 3. However, with Wilson or $\mathcal{O}(a)$ Symanzik-improved "clover" actions, it is hard to deal with relativistic heavy quarks due to the large discretization lattice artifact. The Fermilab interpretation [86] was designed to overcome these difficulties. Therefore, we implement the Fermilab version of the clover action for charm quarks to reduce the lattice artifact in the overall simulations in this thesis. The Fermilab actions S can be written as [86]

$$S = S_0 + S_B + S_E \,, \tag{4.14}$$

where S_0 is the action for dimension-three and four interactions:

$$\begin{aligned} S_0 = \sum_n \bar{\psi}_n \psi_n \quad &- \quad \kappa_t \sum_n \left[\bar{\psi}_n (1-\gamma_0) U_{n,0} \psi_{n+\hat{0}} + \bar{\psi}_{n+\hat{0}} (1+\gamma_0) U^\dagger_{n,0} \psi_n \right] \\ &- \quad \kappa_s \sum_{n,i} \left[\bar{\psi}_n (r_s-\gamma_i) U_{n,i} \psi_{n+\hat{i}} + \bar{\psi}_{n+\hat{i}} (r_s+\gamma_i) U^\dagger_{n,i} \psi_n \right] , \end{aligned} \tag{4.15}$$

S_B is the chromomagnetic dimension-five interaction :

$$S_B = \frac{i}{2} c_B \kappa_s \sum_{n;i,j,k} \epsilon_{ijk} \bar{\psi}_n \sigma_{ij} B_{n;k} \psi_n \,, \tag{4.16}$$

and S_E is the chromoelectric dimension-five interaction :

$$S_E = i c_E \kappa_s \sum_{n;i} \bar{\psi}_n \sigma_{0i} E_{n;i} \psi_n, \tag{4.17}$$

where ψ and $\bar{\psi}$ denote the quark and antiquark fields and B and E are suitable functions of the lattice gauge field U. We set the temporal and spatial hopping parameters to be same, $\kappa_t = \kappa_s = \kappa$. Also, we set $r_s = 1$ and $c_E = c_B = c_{SW}$. Thus, the action reduces to the

Table 4.1. Simulation run parameters and number of configurations of the ensembles in use for the low-lying charmonium study. From left, listed parameters are the approximate lattice spacing a, the ratio of the light and heavy seaquark masses m_l/m_h, the lattice size $L^3 \times T$, the total number of sources (4 time slices times the number of gauge configurations), the tuned charm-quark hopping parameter κ_c, and finally, the charm-quark hopping parameter $\kappa_{\rm sim}$ used in this simulation, respectively. Note that for the uncertainty of κ_c displayed in the fifth column, the first uncertainty is statistical, the second is from the uncertainty in the lattice scale.

$\approx$ a [fm]	m_l/m_h	size	# of sources	κ_c	$\kappa_{\rm sim}$
0.14	0.2	$16^3 \times 48$	2524	0.12237(26)(20)	0.1221
0.14	0.1	$20^3 \times 48$	2416	0.12231(26)(20)	0.1221
0.114	0.2	$20^3 \times 64$	4800	0.12423(15)(16)	0.12423
0.114	0.1	$24^3 \times 64$	3328	0.12423(15)(16)	0.1220/0.1245/0.1280
0.082	0.2	$28^3 \times 96$	1904	0.12722(9)(14)	0.12722
0.082	0.1	$40^3 \times 96$	4060	0.12714(9)(14)	0.12714
0.058	0.2	$48^3 \times 144$	2604	0.12960(4)(11)	0.1298
0.058	0.1	$64^3 \times 144$	1984	0.12955(4)(11)	0.1296
0.043	0.2	$64^3 \times 192$	3204	0.130921(16)(70)	0.1310

Sheikholeslami-Wohlert action [34]. The energy-momentum dispersion relation for a single quark of spatial momentum $\boldsymbol{p}$ in this action is

$$E(\boldsymbol{p}) = m_1 + \frac{\boldsymbol{p}^2}{2m_2} + O(p^4)\,, \tag{4.18}$$

where the quark rest mass is m_1, and the kinetic mass is m_2. At tree level in lattice QCD perturbation theory,

$$m_1 a = \log(1 + m_0 a) \tag{4.19}$$

$$m_2 a = \left(\frac{2}{m_0 a(2 + m_0 a)} + \frac{1}{m_0 a + 1} \right)^{-1}\,, \tag{4.20}$$

where m_0 is the bare quark mass. It can be expressed in terms of κ and $\kappa_{\rm crit}$,

$$m_0 a = \frac{1}{2u_0} \left(\frac{1}{\kappa} - \frac{1}{\kappa_{crit}} \right)\,, \tag{4.21}$$

where κ_{crit} is critical value of κ at which chiral symmetry is restored and the quark mass vanishes.[3] Note that $m_1 \neq m_2$ unless $ma \ll 1$.

[3]For the case of the Wilson action, $\kappa_{crit} = 1/8r$. See Eq. (3.61).

4.2.4 Interpolating operators

As listed in Table 3.2, the simplest interpolators are the color-singlet local fermion bilinears, $\bar{c}_\alpha(\vec{x},t)\Gamma_{\alpha\beta}c_\beta(\vec{x},t)$, where the quantum numbers are determined by the choice of the gamma matrix, Γ. The charm-quark fields can be replaced by a rotationally symmetric smeared quark source field. However, as discussed in Chapter 3, to extract a highly excited state, it is more helpful to use various interpolators involving non-local derivative operators [70, 87–92] with appropriate quantum numbers. They can be constructed to be both irreducible representations of the lattice rotation group (O_h) at zero momentum and to have definite form in the continuum limit (*cf.* Sec. 3.5.1).

In this study, we use stochastic wall sources discussed in Sec. 3.5.2. The rotationally symmetric smeared source can be constructed by applying successive derivative operations to the stochastic sources. Let S_W represent the smearing levels where S_p is the plain stochastic wall source and S_g is the covariant Gaussian smearing sources constructed from S_p :

$$\begin{aligned} S_g(x) &= M(x)S_p(x)\,, \\ M(x) &= \left(1+\frac{\sigma^2}{4N}\Delta\right)^N\,, \end{aligned} \tag{4.22}$$

where Δ is the three-dimensional Laplacian operator on the lattice, defined in Eq. (3.57), but summed over only spatial lattice sites, $\mu = 1, 2,$ and 3. From $\exp(a) \approx (1+\frac{a}{N})^N$ for $N \to \infty$, $M(x)$ is proportional to $e^{\sigma^2\Delta/4}$ and approximates a Gaussian in coordinate space.

For the non-local derivative operators, we need to define the covariant derivatives D_i on the lattice:

$$D_i(\vec{x},\vec{y}) = U_i(\vec{x},0)\delta(\vec{x}+a\hat{i},\vec{y}) - U_i(\vec{x}-a\hat{i},0)^\dagger\delta(\vec{x}-a\hat{i},\vec{y})\,, \tag{4.23}$$

where $\hat{i}$ runs over only spatial direction, $\hat{i} = 1, 2, 3$. To reduce UV fluctuations in the creation of these sources, the spatial links are smeared using n_{APE} steps of "APE smearing" [93],

$$\begin{aligned} V_i(x) &= (1-\alpha)U_i + \frac{\alpha}{6}\sum_{i\neq\mathrm{j}}^{3} C_{ij}(x)\,, \\ C_{ij}(x) &= U_j(x)U_i(x+a\hat{j})U_j(x+a\hat{i})^\dagger + U_j(x-a\hat{j})^\dagger U_i(x-a\hat{j})U_j(x-a\hat{j}+a\hat{i}) \end{aligned}$$

with a typical weight of $\alpha = 0.1$ for the staples. Notice that the original gauge links are used for creating the quark propagator. At the sink, the order of operators is reversed in

order to treat sources and sink symmetrically under time reversal. With this prescription, we implement the following non-local interpolators:

$$\begin{aligned} \vec{\nabla}_i &= M D_i S_p \,, \\ \mathbb{D}_i &= M \,|\varepsilon_{ijk}|\, \vec{D}_j \vec{D}_k S_p \,, \\ \mathbb{B}_i &= \varepsilon_{ijk} M \overrightarrow{D}_j \overrightarrow{D}_k S_p \,. \end{aligned} \tag{4.24}$$

For example, using these operators, one can write the interpolators classified by T_1^{--} as fermion bilinear,

$$\bar{c}\nabla_i c \;, \quad \bar{c}|\epsilon_{ijk}|\gamma_j \mathbb{D}_i c \;, \quad \bar{c}\gamma_5 \mathbb{B}_i c \,.$$

Finally, in this low-lying charmonium study, we consider seven channels classified by irreducible representations with the corresponding interpolating operators represented by the above equations. In Table 4.2, we list the interpolators for each irreducible representation. Note that the interpolators without derivatives are used with both point, S_p, and Gaussian, S_G, sources and sinks.

4.2.5 Charm quark-mass corrections

Because the hopping parameter, κ, was tuned more precisely after the simulation was done, the data must be corrected for the slightly mistuned charm-quark hopping parameter, $\kappa_{\rm sim}$. Consider the small shift in the mass-splitting observables, ΔM_1, *e.g.,* Eqs. (4.10), (4.13) and (4.13). Then, the relation between corrected and simulated data is

$$\Delta M_1^{\rm corrected} = \Delta M_1^{\rm sim} + \frac{d\Delta M_1}{d\kappa}\delta\kappa \,. \tag{4.25}$$

Therefore, to determine the correction, we need to calculate the slope, $d\Delta M_1/d\kappa$, on each ensemble. This is done by measuring the hopping parameter dependence of the kinetic charm quark mass, m_2, on one ensemble, $a \approx 0.11$ fm for $m_l/m_h = 0.1$ with three different kappas, where we use m_2 instead of m_1 because m_2 controls the quark dynamics. Once we determine the hopping parameter dependence for the all observables, then we assume that the slope, expressed in physical quantities, is constant to a good approximation:

$$\frac{dM_1}{dm_2} = \text{const.} \,, \tag{4.26}$$

over the all lattice spacings and sea quark masses. Then, by differentiating Eqs. (4.20) and (4.21) by κ, and by combining the resulting expressions, we get

$$\frac{dr_1\Delta M_1}{d\kappa} = \frac{d\Delta M_1}{dm_2} \cdot \left(\frac{r_1}{a}\right) \frac{d(m_2 a)}{d\kappa} \tag{4.27}$$

$$= \frac{d\Delta M_1}{dm_2} \cdot A \tag{4.28}$$

Table 4.2. Interpolating operators used for the variational analysis. The first row lists J^{PC} in use as the irreps. of octahedral group. The correspondence between continuum J and irreps. of octahedral group are listed in Table 3.1. Repeated indices are summed over. Interpolators without derivatives are used with both point (S_p) and Gaussian (S_g) sources and sinks.

A_1^{-+}	A_1^{++}	T_1^{--}	T_1^{+-}	T_1^{++}	T_2^{++}	E^{++}
$\gamma_5 \cdot S_p$	$\mathbb{1} \cdot S_p$	$\gamma_i \cdot S_p$	$\gamma_t\gamma_5\gamma_i \cdot S_p$	$\gamma_5\gamma_i \cdot S_p$	$\lvert\varepsilon_{ijk}\rvert\gamma_j\nabla_k$	$Q_{ijk}\gamma_j\nabla_k$
$\gamma_5 \cdot S_g$	$\mathbb{1} \cdot S_g$	$\gamma_i \cdot S_g$	$\gamma_t\gamma_5\gamma_i \cdot S_g$	$\gamma_5\gamma_i \cdot S_g$	$\lvert\varepsilon_{ijk}\rvert\gamma_t\gamma_j\nabla_k$	$Q_{ijk}\gamma_t\gamma_j\nabla_k$
$\gamma_t\gamma_5 \cdot S_p$	$\gamma_i\nabla_i$	$\gamma_t\gamma_i \cdot S_p$	$\gamma_5\nabla_i$	$\varepsilon_{ijk}\gamma_j\nabla_k$	$\mathbb{D}_i$	$Q_{ijk}\gamma_5\gamma_j\mathbb{D}_k$
$\gamma_t\gamma_5 \cdot S_g$	$\gamma_t\gamma_i\nabla_i$	$\gamma_t\gamma_i \cdot S_g$	$\gamma_t\gamma_5\nabla_i$	$\varepsilon_{ijk}\gamma_t\gamma_j\nabla_k$	$\lvert\varepsilon_{ijk}\rvert\gamma_t\gamma_5\gamma_j\mathbb{B}_k$	$Q_{ijk}\gamma_t\gamma_5\gamma_j\mathbb{B}_k$
$\gamma_t\gamma_5\gamma_i\nabla_i$	$\gamma_t\gamma_5\gamma_i\mathbb{B}_i$	∇_i	$\lvert\varepsilon_{ijk}\rvert\gamma_t\gamma_5\gamma_j\mathbb{D}_k$	$\lvert\varepsilon_{ijk}\rvert\gamma_5\gamma_j\mathbb{D}_k$		
$\gamma_i\mathbb{B}_i$		$\varepsilon_{ijk}\gamma_5\gamma_j\nabla_k$	$\mathbb{B}_i$	$\gamma_t\mathbb{B}_i$		
$\gamma_t\gamma_i\mathbb{B}_i$		$\lvert\varepsilon_{ijk}\rvert\gamma_j\mathbb{D}_k$	$\varepsilon_{ijk}\gamma_5\gamma_j\mathbb{B}_k$	$\varepsilon_{ijk}\gamma_t\gamma_5\gamma_j\mathbb{B}_k$		
		$\lvert\varepsilon_{ijk}\rvert\gamma_t\gamma_j\mathbb{D}_k$				
		$\gamma_5\mathbb{B}_i$				
		$\gamma_t\gamma_5\mathbb{B}_i$				

Thus, A is the only ensemble-dependent parameter. From Eq. (4.20), it is

$$A = \left(\frac{r_1}{a}\right)\frac{1}{2u_0\kappa^2}\frac{4 + 12m_0a + 16(m_0a)^2 + 8(m_0a)^3 + (m_0a)^4}{(2 + 4(m_0a) + (m_0a)^2)^2}\,. \tag{4.29}$$

Table 4.3 displays all the values needed for the kappa correction. Once we determine the slopes of the observables over κ on one ensemble (here the ensemble with $a \approx 0.11$ fm for $m_l/m_h = 0.1$), we can calculate all kappa tuning corrections on all other ensembles.

4.2.6 Scale setting uncertainty

Lattice quantities are measured in units of the lattice spacing. Scale setting is needed to determine the lattice spacing in physical units (*e.g.,* fm). This is needed to convert all dimensionful quantities to physical unit. For example, consider the dimensionless quantity, aM, which is the product of the lattice spacing and mass M. Then, to determine M in physical mass units, we need to determine the lattice spacing a (or scale) in physical units. To determine the scale, we go through an intermediate quantity that is easily measured on the lattice. That quantity is the length r_1, called the Sommer scale, of the force between static quarks, $r_1^2F(r_1) = 1$. The values of r_1/a for the asqtad ensembles can be found in [12]. Then, the scale r_1 is determined from a precise lattice measurement of the pion decay constant, and its precise experimental value. r_1 has been determined to be 0.31174(216) fm [12] in the "mass-independent scheme". For the figures presented in Sec. 4.3, we use the

Table 4.3. The parameters required for the charm-quark mass corrections. From left, listed parameters show the lattice spacings, the ratio of simulation seaquark masses, the critical κ value, the tadpole factor, the ratio of the Sommer scale r_1 [11] to the lattice spacing, the calculated bare quark mass, and the resulting factor A from Eq. (4.29). The values of r_1/a for the asqtad ensembles and an explanation for our value $r_1 = 0.31174(216)$ can be found in Ref. [12].

$\approx a$	m_l/m_h	κ_{crit}	u_0	r_1/a	$m_0 a$	A
0.14	0.2	0.14243	0.8604	2.2215	0.67849	71.54
0.114	0.2	0.14091	0.8677	2.7386	0.53872	85.06
0.082	0.2	0.13912	0.8782	3.7887	0.35147	112.42
0.058	0.2	0.13763	0.8879	5.3531	0.24593	155.40
0.043	0.2	0.13664	0.8951	7.2082	0.17481	208.69
0.14	0.1	0.14236	0.8602	2.2067	0.67849	71.15
0.114	0.1	0.14096	0.8678	2.7386	0.53872	85.04
0.082	0.1	0.13917	0.8779	3.7546	0.36191	111.51
0.058	0.1	0.13768	0.8876	5.3073	0.25263	154.10

Sommer scale r_1 [11]. For each observable, we first determine the result using the central value for both r_1 and κ_c and then repeat the procedure using the both the scale $r_1 = 0.3139$ fm and the κ_c resulting from the same shift. Although the scale setting uncertainties along with the observables are relevant, we do not include these effects in this thesis. This will be done before we complete the journal paper.

4.2.7 Heavy quark effective field theory

To perform the continuum extrapolation, we need to understand how the heavy-quark discretization effects behave on the lattice. To do so, one can implement an effective Lagrangian that has manifest symmetry in the $m_Q \to \infty$. One can consider two ways to construct such Lagrangians – one, the inverse powers of m_Q appear in the effective the Lagrangian, the other, the powers of $v_{Q\bar{Q}}/c$. The former is called "heavy-quark effective theory" (HQET), where it is appropriate to describe the systems with only one heavy quark and the correction terms are order of the powers of $1/m_Q$, the latter is called "nonrelativistic QCD" (NRQCD), where it is appropriate to describe the systems with more than one heavy quarks and the correction terms are order of the powers of $v_{Q\bar{Q}}/c$.

As long as $m_Q \gg \Lambda_{\rm QCD}$, one can write both effective Lagrangians as

$$\mathcal{L}_{\rm lat} \doteq \mathcal{L}_{\rm HQ}\,, \tag{4.30}$$

where $\doteq$ means they have the same matrix elements in their respective frameworks. Both HQET and NRQCD share the same effective Lagrangian

$$\mathcal{L}_{\rm HQ} = \sum_n \mathcal{C}_n^{\rm lat}(m_Q, g_S^2, m_Q a; \mu/m_Q)\mathcal{O}_n(\mu)\,, \tag{4.31}$$

where μ is the renormalization point and m_Q is heavy quark mass. The $\mathcal{C}_n$ are short-distance coefficients and the operators $\mathcal{O}_n$ give the long-distance behavior. This effective Lagrangian can be expanded in a small parameter. The expansion parameter of the HQET is $1/m_Q$ and of NRQCD is v/c. One can then use "power counting" to determine what terms in the effective field theories are relevant to a given order in the small parameter, where with power counting scheme, we match dimensionality of the operator $\mathcal{O}$ and determine the coefficients $\mathcal{C}$, appropriately, which is order of 1. Thus, $\mathcal{L}_{\rm HQ}$ can be expanded as

$$\mathcal{L}_{\rm HQ} = \mathcal{L}^{(0)} + \mathcal{L}^{(1)} + \mathcal{L}^{(2)} + ..., \tag{4.32}$$

where for HQET, $\mathcal{L}^{(s)}_{\rm HQET}$ contains terms of dimension $4+s$, and for NRQCD, $\mathcal{L}_{\rm NRQCD}$ contains terms of order v^{2s+2}, where v is the relative velocity of charm quark and charm antiquark.

As mentioned above, NRQCD is more appropriate to describe the two heavy quark system. Therefore, for continuum extrapolation, we use NRQCD power-counting. Thus, it must be useful to write the first several terms of $\mathcal{L}_{\rm NRQCD}$,

$$\begin{aligned}
\mathcal{L}^{(2)}_{\rm NRQCD} &= -\bar{h}^{(+)}(D_4 + m_1)h^{(+)} + \frac{\bar{h}^{(+)}\boldsymbol{D}^2 h^{(+)}}{2m_2} - \bar{h}^{(-)}(D_4 + m_1)h^{(-)} + \frac{\bar{h}^{(-)}\boldsymbol{D}^2 h^{(-)}}{2m_2}\,, \\
\mathcal{L}^{(4)}_{\rm NRQCD} &= \frac{\bar{h}^{(+)} i\boldsymbol{\sigma}\cdot\boldsymbol{B} h^{(+)}}{2m_B} + \frac{\bar{h}^{(+)} i\boldsymbol{\sigma}\cdot(\boldsymbol{D}\times\boldsymbol{E}) h^{(+)}}{8m_E^2} + \frac{\bar{h}^{(+)}(\boldsymbol{D}\cdot\boldsymbol{E}) h^{(+)}}{8m_E'^2} + \frac{\bar{h}^{(+)}(\boldsymbol{D}^2)^2 h^{(+)}}{8m_4^3} \\
&+ \frac{\bar{h}^{(-)} i\boldsymbol{\sigma}\cdot\boldsymbol{B} h^{(-)}}{2m_B} - \frac{\bar{h}^{(-)} i\boldsymbol{\sigma}\cdot(\boldsymbol{D}\times\boldsymbol{E}) h^{(-)}}{8m_E^2} - \frac{\bar{h}^{(-)}(\boldsymbol{D}\cdot\boldsymbol{E}) h^{(-)}}{8m_E'^2} + \frac{\bar{h}^{(-)}(\boldsymbol{D}^2)^2 h^{(-)}}{8m_4^3} \\
&+ \frac{1}{6}a^3 w_4 \bar{h}^{(+)} D_i^4 h^{(+)} + \frac{1}{6}a^3 w_4 \bar{h}^{(-)} D_i^4 h^{(-)}\,,
\end{aligned} \tag{4.33}$$

where $h^{(+)}$ and $h^{(-)}$ are a two-component heavy quark field and a two-component heavy antiquark field, respectively. The short-distance coefficients, $\mathcal{C}_n^{\rm lat}$ in Eq. (4.31), m_1, m_2^{-1}, m_B^{-1}, m_E^{-2}, $m_{E'}^{-2}$, m_4^{-3} and w_4 depend on the bare quark masses, the bare gauge coupling, and all other couplings of the lattice actions. As an example, the short-distance coefficient m_B is [7]

$$\frac{1}{m_B a} = \frac{1}{m_2 a} + \frac{(c_B - r)\zeta}{1 + m_0 a}\,, \tag{4.34}$$

and one of the the mass mismatching terms is

$$\frac{1}{4m_E^2} - \frac{1}{4m_2^2} = \frac{a^2}{(2+m_0a)(1+m_0a)} - \frac{a^2}{4(1+m_0a)^2}\,, \tag{4.35}$$

$$\tag{4.36}$$

and the symmetry breaking term is

$$a^3 w_4 = \frac{2a^2}{m_0(2+m_0a)} + \frac{a^3}{4(1+m_0a)}\,, \tag{4.37}$$

which introduces errors of order of $a^2m^3v^4$ in the spin-averaged splittings.

4.2.8 Discretization effects in charmonium mass splittings

For the charmonium masses calculated on the lattice, $M_{\rm lat}$ is

$$\begin{aligned} M_{\rm lat} &= M_{\rm cont} + 2(m_1 - m_2) - \frac{1}{3}w_4 a^3 \sum_i \langle p_i^4 \rangle \\ &- \left(\frac{1}{4m_4^3} - \frac{1}{4m_2^3}\right)\langle (\boldsymbol{p}^2)^2 \rangle + \left(\frac{1}{4m_E^2} - \frac{1}{4m_2^2}\right)\langle 4\pi C_F \alpha_S \delta(\boldsymbol{r}) \rangle \end{aligned} \tag{4.38}$$

where $M_{\rm cont}$ is the charmonium mass in the continuum, and $\boldsymbol{p}$ is the relative momentum. The last term comes from the Darwin term with $C_F = 4/3$ for SU(3). Here, our goal is to find $M_{\rm cont}$. Therefore, we need to understand the functional dependence of the discretization effect on the lattice parameters, bare quark mass, lattice spacing, and gauge coupling. Once we know it, we can extrapolate $M_{\rm lat}$ to the continuum to find $M_{\rm cont}$.

First, consider the $\overline{1P} - \overline{1S}$ mass splitting,

$$\begin{aligned} M_{\rm lat}(1P) - M_{\rm lat}(1S) &= M_{\rm cont}(1P) - M_{\rm cont}(1S) - \frac{1}{w_4}a^3 \sum_i \left(\langle p_i^4 \rangle_{1P} - \langle p_i^4 \rangle_{1S} \right) \\ &- \left(\frac{1}{4m_4^3} - \frac{1}{4m_2^3}\right)\left(\langle (\boldsymbol{p}^2)^2 \rangle_{1P} - \langle (\boldsymbol{p}^2)^2 \rangle_{1S} \right) \qquad (4.39) \\ &+ 4\pi C_F \alpha_S \left(\langle \delta(\boldsymbol{r}) \rangle_{\overline{1P}} - \langle \delta(\boldsymbol{r}) \rangle_{\overline{1S}} \right) \qquad (4.40) \end{aligned}$$

We can evaluate the expectation values of the momentum $\boldsymbol{p}$ from NRQCD power counting using Coulomb wave function and the Hamiltonian [81, 94],

$$H = -\frac{1}{m_2}\nabla^2 - C_F \frac{\alpha_S}{r}\,. \tag{4.41}$$

For charmonium, $\alpha_S \sim v \sim 0.3$. Then, the expectation values in Eq. (4.40) are given by

$$\langle (\boldsymbol{p}^2)^2 \rangle_{\overline{1P}} - \langle (\boldsymbol{p}^2)^2 \rangle_{\overline{1S}} = -\frac{233}{243} m_2^4 \alpha_S^4\,, \tag{4.42}$$

$$\sum_i \left(\langle p_i^4 \rangle_{\overline{1P}} - \langle p_i^4 \rangle_{\overline{2S}} \right) = -\frac{233}{405} m_2^4 \alpha_S^4\,, \tag{4.43}$$

$$4\pi C_F \alpha_S \left(\langle \delta(\boldsymbol{r}) \rangle_{\overline{1P}} - \langle \delta(\boldsymbol{r}) \rangle_{\overline{1S}} \right) = -\frac{128}{81} m_2^3 \alpha_S^4\,. \tag{4.44}$$

For the expression of mass mismatching terms, see Ref. [7].

Next, consider spin-dependent splittings. Here, we briefly go over the terms. For the full discussion, refer to Ref. [95]. The hyperfine and tensor splittings arise from the gluon exchange interactions in the NRQCD Lagrangian given by Eq. (4.31),

$$\bar{h}^{(+)} i\boldsymbol{\sigma}\cdot\boldsymbol{B} h^{(+)} \bar{h}^{(-)} i\boldsymbol{\sigma}\cdot\boldsymbol{B} h^{(-)} \,. \tag{4.45}$$

The mismatch coefficient of this interaction is of order

$$\left(\frac{1}{2m_B} - \frac{1}{2m_2}\right)^2 \sim \alpha_S \sim v \,. \tag{4.46}$$

In addition, we need to consider the higher-dimensional operators for this splitting. Replacing $i\boldsymbol{\sigma}\cdot\boldsymbol{B} \to \{\boldsymbol{D}^2, i\boldsymbol{\sigma}\cdot\boldsymbol{B}\}$, where $\{...\}$ indicates the anticommutator, introduces shifts of the form $v^2 \sim \alpha_S^2$ times

$$\frac{1}{4m_{B'}^3} - \frac{1}{4m_2^3} \,, \tag{4.47}$$

relative to the continuum hyperfine and tensor splittings.

The leading heavy-quark discretization effects contributing to the hyperfine and tensor splittings come from mismatches of m_B and m_2. Following [7], we use NRQCD power counting with $v_{c\bar{c}}^2 = 0.3$ and $m_c = 1400$ MeV along with the tree level formula from [86] to estimate the expected size of all heavy-quark discretization effects. The relevant formula for m_B is Eq. (4.22) of [7]. Notice that our fermion action includes a clover term with the tadpole improved tree-level value $c_b = c_e = \frac{1}{u_0^3}$, where u_0 is the average link from the plaquette. The contribution is therefore improved and the suppression with respect to the reference scale given by $m_c v_c^2$ (the kinetic energy of the meson) contains a factor $\frac{1}{2}\alpha_s v_c^2$.

The next smaller heavy-quark discretization effects come from mismatches of $m_{B'}$ and m_2, where the relevant formula for $m_{B'}$ is given by Eq. (4.23) of [7]. This mismatch is of a higher order in the NRQCD power counting and suppressed by $\frac{1}{8}v^4$ with respect to the kinetic energy.

Similarly, the spin-orbit splittings arise from interactions of the form

$$\bar{h}^{(\pm)} i\boldsymbol{\sigma}\cdot(\boldsymbol{D}\times\boldsymbol{E}) h^{(\pm)} \bar{h}^{(\mp)} A_4 h^{(\mp)} \tag{4.48}$$

Again, we have set $c_E = c_B$, so that the mismatch becomes

$$\frac{1}{2m_E^2} - \frac{1}{2m_2^2} \,. \tag{4.49}$$

In the following sections, we use the terms "leading shape" and "leading + subleading shapes". In the former is the case we include only leading order of the discretization effect in NRQCD when we perform a continuum extrapolation, and in the latter, we include both leading and the next to leading order of discretization effects in NRQCD. Each figure in Sec. 4.3 includes two plots to compare these two cases.

4.2.9 Chiral and continuum fits

We perform an extrapolation to the continuum as well as chiral limit of the light-quark masses [8, 9]. For each observable, we compared continuum extrapolations with just the leading shape (either $\alpha_S a^2$ or the leading heavy-quark discretization term) and using both the leading and subleading for the shapes heavy-quark discretization terms as well as the generic $\alpha_S a^2$ shape. We determine the most important mismatches arising at order v^4 and/or order v^6 in NRQCD power-counting.

As we discussed in the previous section, the discretization effects in the mass depends on the mass mismatch parameters. Therefore, we can write the fit model for the combined extrapolation as

$$\begin{aligned} M &= M_0 + c_1(2x_l + x_h) + c_2 f_1(a) + c_3 f_2(a) + \ldots \\ x_l &= \frac{m_{ud,sea} - m_{ud,phys}}{m_{s,phys}} \\ x_h &= \frac{m_{s,sea} - m_{s,phys}}{m_{s,phys}} \end{aligned} \tag{4.50}$$

where c_i are the fit parameters. $m_{ud,sea}$ and $m_{s,sea}$ are the degenerate up and down mass, and the strange sea quark masses used in simulation, respectively. Then, $m_{ud,phys}$, and $m_{s,phys}$ are physical up, down, and strange quark masses, respectively. Their values are displayed in Table 4.4. For the each different splitting, the functions f_i are determined from mass mismatches within the Fermilab prescription [7].

Figure 4.3 shows the expected discretization uncertainties from power counting estimates for the splitting indicated each figure. The plotted curves corresponds to $c_i = 1$ for all i. In some of our fits, in order to stabilize the fits, we use Bayesian priors for c_i, centered around 0 with a width of 2 as a constraint. In the fit for the $1P - 1S$-splitting, we also allow for a term from rotational symmetry breaking (w_4 term). In addition to these terms, we also allow for a generic $\alpha_s a^2$ term characteristic of the heavy-quark discretization effects from the gauge action.

4.3 Results

We perform a variational analysis to extract the low-lying energy levels. Then, we calculate the $1S$ hyperfine splitting as in Eq. (4.10) and spin-orbit, $1P$ tensor splittings as in Eq. (4.13). Finally, we perform the chiral-continuum extrapolation according to Eq. (4.51). In some cases, implementing the full sets of interpolating operators is not helpful to reduce the size of the uncertainty. Tables 4.5 and 4.6 show our choices of interpolating operators used in the variational analysis to extract energy levels. The '1' in the basis column means

Table 4.4. Nominal (sea) light and heavy quark masses compared with physical light and strange quark masses for each ensemble. The first column shows the approximate lattice spacing. The second and the third columns list the light and strange sea quark mass used for the simulation, respectively. The third and the fourth columns show physical light and strange quark masses.

$\approx a$	$m_{ud,sea}$	$m_{s,sea}$	$m_{ud,phys}$	$m_{s,phys}$
0.14	0.0097	0.0484	0.0015079	0.04185
0.114	0.01	0.05	0.0012150	0.03357
0.082	0.0062	0.031	0.0008923	0.02446
0.058	0.0036	0.018	0.0006401	0.01751
0.043	0.0024	0.014	0.0004742	0.01298
0.14	0.0048	0.0484	0.0015180	0.04213
0.114	0.005	0.05	0.0012150	0.03357
0.082	0.0031	0.031	0.0009004	0.02468
0.058	0.0018	0.018	0.0006456	0.01766

'used' while '0' means 'not-used'. The corresponding interpolator expressions can be found in Table 4.2.

Concerning uncertainties, we include both statistical and chiral-continuum extrapolation uncertainties. At this stage, we do not include uncertainties from the scale-setting procedure. They will be significant for the 1S-hyperfine and 1P-1S splittings. For the 1S-hyperfine splitting uncertainties, the autocorrelations in the Markov-chain of gauge configurations appear to be significant, and so they are taken into account. We estimate the integrated autocorrelation time using two methods. The first method is the blocking method that I mentioned in Sec. 3.5.3. We construct binned data from the jackknife estimates and extrapolated the results for bins of sizes 1 to 5 to infinite bin size using the expected scaling. Another method is to determine the autocorrelation time from the jackknife sample using the method and software provided by Wolff in [96]. We calculate the autocorrelation time using both methods and check that the results are consistent. We quote results from the first method.

Figure 4.4 shows the results for the 1S-hyperfine splitting. This splitting is sensitive to heavy-quark discretization and charm-quark tuning effects so that the most significant errors are from including the subleading discretization effect. The other contribution is from the charm-annihilation [10]. These effects will be included in Ref. [9] based on the

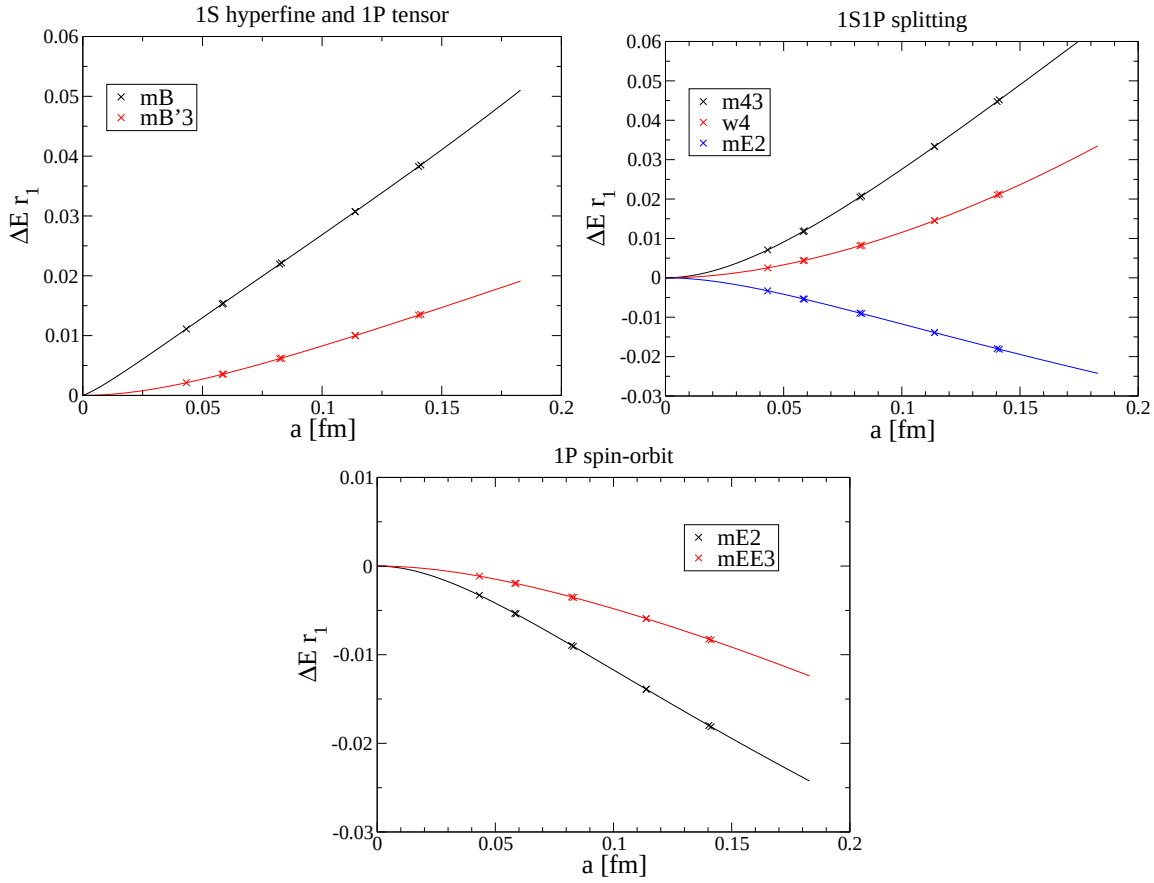

Figure 4.3. Shapes and sizes of the expected discretization uncertainties for charmonium splittings (NRQCD power counting) in the Fermilab approach (using $v^2 = 0.3$ and $mv^2 \approx 420$ MeV$\approx$ 1P-1S-splitting). The symbols mB, mB'3, m43, w4, mE2, and mEE3 represent mismatch coefficients for m_B, $m^3_{B'}$, m^3_4, w_4, m^2_E, and m^3_{EE}, respectively. These short-distance coefficients in $\mathcal{L}_{\rm NRQCD}$ are expressed as $f_i(a)$. See Ref. [7] for the full expressions.

estimation from [10]. Figure 4.5 shows the results for 1P-1S splittings. As in the 1S hyperfine splitting, significant effects from mistuned strange-quark masses are visible in our data. The chiral-continuum fits are stable with regard to the number of shapes, provided reasonable priors are used. The P-wave spin-orbit splitting shown in Fig. 4.6 shows small discretization uncertainties, unlike our results for the P-wave tensor splitting (Fig. 4.7) where the dominant uncertainty arises from the choice of fit model.

Table 4.7 shows our current results for the splittings compared with the experimental values. Except for the 1P-hyperfine splitting, our results shows excellent agreement with experiment.

Table 4.5. Implemented interpolating operators for the variational analysis. The first column represents the data set we used. The labels, 'a0.xx' represent the approximate lattice spacing. When letter 'b' follows, it means $m_l/m_h = 0.1$, otherwise $m_l/m_h = 0.2$. For the data set used for kappa tuning, we add the additional information about the kappa values. The 'v#' are the version numbers. The second column represents the quantum number $J^{\rm PC}$ as the irrep of the octahedral group. The third column represents the reference time, t_0, used for the variational analysis. The fourth column represents the interpolating operator basis implemented in this analysis. The '1' represents the interpolating operator that was used, and '0', the not-used one. They are listed in Table 4.2. For all J^{PC}, each number from left to right matches the interpolator displayed in Table 4.2 from top to bottom, respectively. The rest of the columns show the fit information – fit range, number of exponentials in use, the fit values and the chi-squares per degree of freedoms, in turn.

Data set	J^{PC}	t_0	basis	fit range	fit type	fit result	χ^2/d.o.f.
a0.15_v2	A_1^{-+}	2	1111100	2-20	2exp	1.67624(15)	0.72
a0.15b_v2	A_1^{-+}	2	1111100	2-20	2exp	1.67746(10)	2.35
a0.12_v3	A_1^{-+}	2	1111100	3-27	2exp	1.46897(8)	1.50
a0.12b_k1220	A_1^{-+}	2	1111100	3-27	2exp	1.58055(7)	0.88
a0.12b_k1245	A_1^{-+}	2	1111100	3-27	2exp	1.45278(8)	1.06
a0.12b_k1280	A_1^{-+}	2	1111100	3-27	2exp	1.26162(9)	1.70
a0.09_v2	A_1^{-+}	3	1111100	4-42	2exp	1.14427(8)	1.20
a0.09b_v2	A_1^{-+}	3	1111100	4-42	2exp	1.15211(4)	1.31
a0.06_v2	A_1^{-+}	5	1111100	6-64	2exp	0.83119(4)	1.32
a0.06b_v2	A_1^{-+}	5	1111100	6-64	2exp	0.84756(2)	1.08
a0.045_v2	A_1^{-+}	6	1111100	8-81	2exp	0.63519(3)	1.60
a0.15_v2	T_1^{--}	2	1100111100	2-20	2exp	1.75241(22)	0.50
a0.15b_v2	T_1^{--}	2	1100111100	2-20	2exp	1.75324(16)	1.64
a0.12_v3	T_1^{--}	2	1100111100	3-27	2exp	1.53353(14)	1.46
a0.12b_k1220	T_1^{--}	2	1100111100	3-27	2exp	1.63834(13)	0.92
a0.12b_k1245	T_1^{--}	2	1100111100	3-27	2exp	1.51690(13)	1.06
a0.12b_k1280	T_1^{--}	2	1100111100	3-27	2exp	1.33715(18)	1.31
a0.09_v2	T_1^{--}	3	1100111100	4-42	2exp	1.19131(20)	1.53
a0.09b_v2	T_1^{--}	3	1100111100	4-42	2exp	1.19873(7)	1.01
a0.06_v2	T_1^{--}	5	1100111100	6-64	2exp	0.86508(9)	1.32
a0.06b_v2	T_1^{--}	5	1100111100	6-64	2exp	0.88092(5)	1.18
a0.045_v2	T_1^{--}	6	1100111100	8-81	2exp	0.66053(6)	1.66
a0.15_v2	A_1^{++}	3	11110	4-10	1exp	2.0434(24)	0.20
a0.15b_v2	A_1^{++}	3	11110	4-10	1exp	2.0366(24)	0.33
a0.12_v3	A_1^{++}	3	11110	6-16	1exp	1.7564(20)	0.47
a0.12b_k1220	A_1^{++}	3	11110	6-12	1exp	1.8652(17)	0.11
a0.12b_k1245	A_1^{++}	3	11110	6-12	1exp	1.7395(16)	0.65
a0.12b_k1280	A_1^{++}	3	11110	6-12	1exp	1.5470(23)	0.67
a0.09_v2	A_1^{++}	3	11110	3-19	2exp	1.3421(13)	0.23
a0.09b_v2	A_1^{++}	3	11110	3-19	2exp	1.3481(7)	0.45
a0.06_v2	A_1^{++}	5	11110	6-28	2exp	0.9646(10)	0.77
a0.06b_v2	A_1^{++}	5	11110	6-30	2exp	0.9807(10)	0.57
a0.045_v2	A_1^{++}	6	11110	7-31	2exp	0.7349(8)	0.98

Table 4.6. For an explanation, see the caption of Table 4.5.

Data set	J^{PC}	t_0	basis	fit range	fit type	fit result	χ^2/d.o.f.
a0.15_v2	T_1^{++}	3	1111100	4-10	1exp	2.0907(19)	0.27
a0.15b_v2	T_1^{++}	3	1111100	4-10	1exp	2.0875(14)	0.65
a0.12_v3	T_1^{++}	3	1111100	6-16	1exp	1.8042(14)	0.95
a0.12b_k1220	T_1^{++}	3	1111100	6-12	1exp	1.9043(10)	0.81
a0.12b_k1245	T_1^{++}	3	1111100	6-17	1exp	1.7816(13)	0.51
a0.12b_k1280	T_1^{++}	3	1111100	6-14	1exp	1.6008(17)	0.54
a0.09_v2	T_1^{++}	3	1111100	3-23	2exp	1.3783(24)	1.29
a0.09b_v2	T_1^{++}	3	1111100	3-24	2exp	1.3843(8)	1.14
a0.06_v2	T_1^{++}	5	1111100	6-24	2exp	0.9930(12)	0.93
a0.06b_v2	T_1^{++}	5	1111100	6-32	2exp	1.0070(11)	0.81
a0.045_v2	T_1^{++}	6	1111100	7-41	2exp	0.7542(10)	0.68
a0.15_v2	T_2^{++}	3	1111	4-10	1exp	2.1260(24)	0.34
a0.15b_v2	T_2^{++}	3	1111	4-10	1exp	2.1231(17)	1.46
a0.12_v3	T_2^{++}	3	1111	6-16	1exp	1.8307(22)	0.74
a0.12b_k1220	T_2^{++}	3	1111	6-19	1exp	1.9307(16)	0.47
a0.12b_k1245	T_2^{++}	3	1111	6-18	1exp	1.8104(19)	0.29
a0.12b_k1280	T_2^{++}	3	1111	6-17	1exp	1.6305(30)	0.80
a0.09_v2	T_2^{++}	3	1111	3-19	2exp	1.4006(25)	0.79
a0.09b_v2	T_2^{++}	3	1111	3-23	2exp	1.4045(11)	0.79
a0.06_v2	T_2^{++}	5	1111	6-25	2exp	1.0082(19)	0.92
a0.06b_v2	T_2^{++}	5	1111	6-29	2exp	1.0176(42)	1.05
a0.045_v2	T_2^{++}	6	1111	7-31	2exp	0.7644(20)	0.81
a0.15_v2	E^{++}	3	1111	4-10	1exp	2.1269(24)	0.14
a0.15b_v2	E^{++}	3	1111	4-10	1exp	2.1235(17)	1.77
a0.12_v3	E^{++}	3	1111	6-13	1exp	1.8303(25)	0.32
a0.12b_k1220	E^{++}	3	1111	6-17	1exp	1.9310(17)	0.58
a0.12b_k1245	E^{++}	3	1111	6-15	1exp	1.8113(20)	0.28
a0.12b_k1280	E^{++}	3	1111	6-17	1exp	1.6311(31)	0.48
a0.09_v2	E^{++}	3	1111	3-19	2exp	1.4018(20)	0.98
a0.09b_v2	E^{++}	3	1111	3-23	2exp	1.4051(11)	0.87
a0.06_v2	E^{++}	5	1111	6-29	2exp	1.0081(21)	0.89
a0.06b_v2	E^{++}	5	1111	6-24	2exp	1.0201(35)	1.57
a0.045_v2	E^{++}	6	1111	7-31	2exp	0.7633(26)	0.84
a0.15_v2	T_1^{+-}	3	1111100	4-10	1exp	2.1017(19)	0.27
a0.15b_v2	T_1^{+-}	3	1111100	4-10	1exp	2.1001(12)	1.41
a0.12_v3	T_1^{+-}	3	1111100	6-16	1exp	1.8129(13)	0.44
a0.12b_k1220	T_1^{+-}	3	1111100	6-16	1exp	1.9133(11)	0.77
a0.12b_k1245	T_1^{+-}	3	1111100	6-16	1exp	1.7919(12)	0.77
a0.12b_k1280	T_1^{+-}	3	1111100	6-17	1exp	1.6124(15)	0.55
a0.09_v2	T_1^{+-}	3	1111100	3-21	2exp	1.3856(29)	1.96
a0.09b_v2	T_1^{+-}	3	1111100	3-21	2exp	1.3917(8)	0.78
a0.06_v2	T_1^{+-}	5	1111100	6-35	2exp	0.9985(19)	0.87
a0.06b_v2	T_1^{+-}	5	1111100	6-35	2exp	1.0115(13)	0.84
a0.045_v2	T_1^{+-}	6	1111100	7-42	2exp	0.7585(11)	1.21

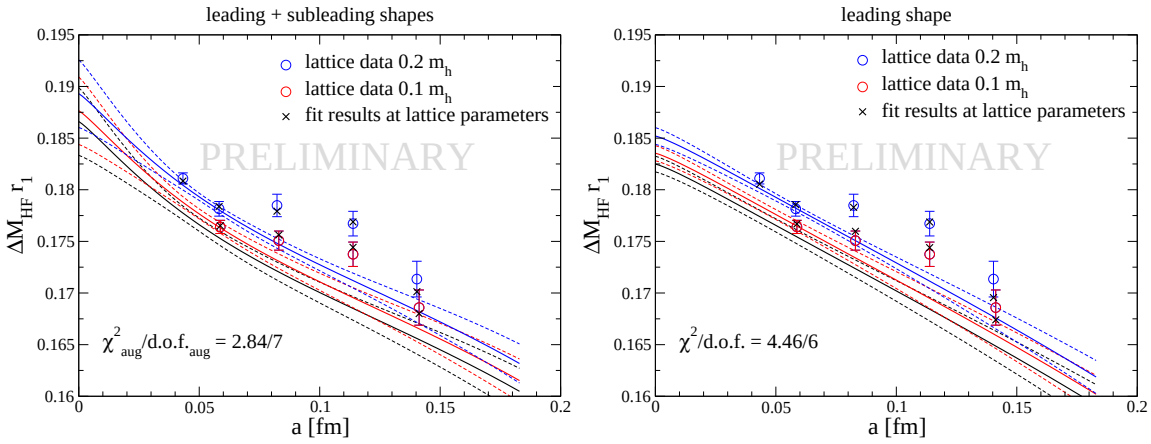

Figure 4.4. Chiral and continuum fit for the 1S-hyperfine splitting using leading and subleading shapes (left) and only the leading shape (right) in the continuum extrapolation [8, 9]. Curves for physical (black), $0.1m_s$, and $0.2m_s$ light-quark masses are plotted. The black crosses show the fit results evaluated at the lattice parameters of the gauge ensemble. Note that many data points are not on the fitting lines because the lines are the results of the chiral extrapolation.

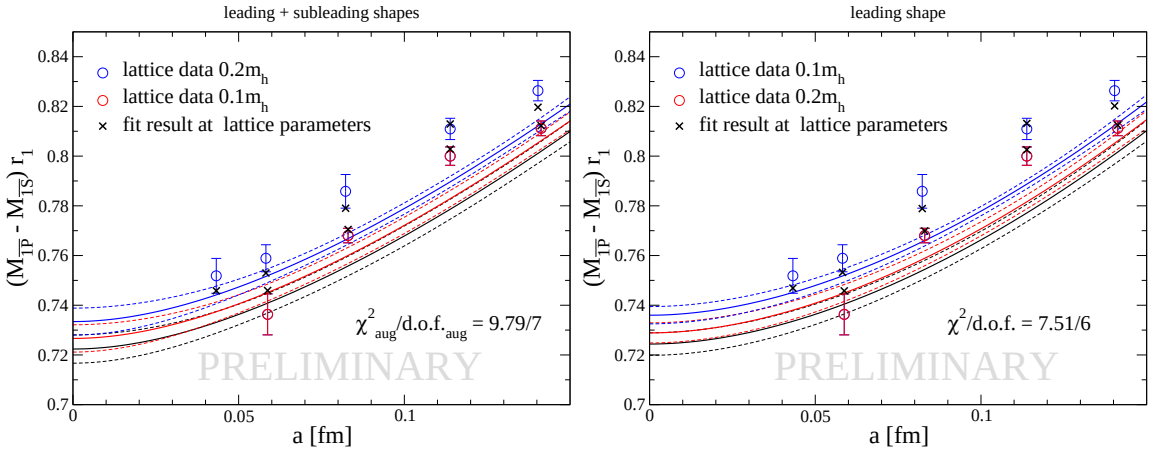

Figure 4.5. Chiral and continuum fit for the 1P-1S-splitting [8, 9]. For an explanation, see caption of Fig. 4.4.

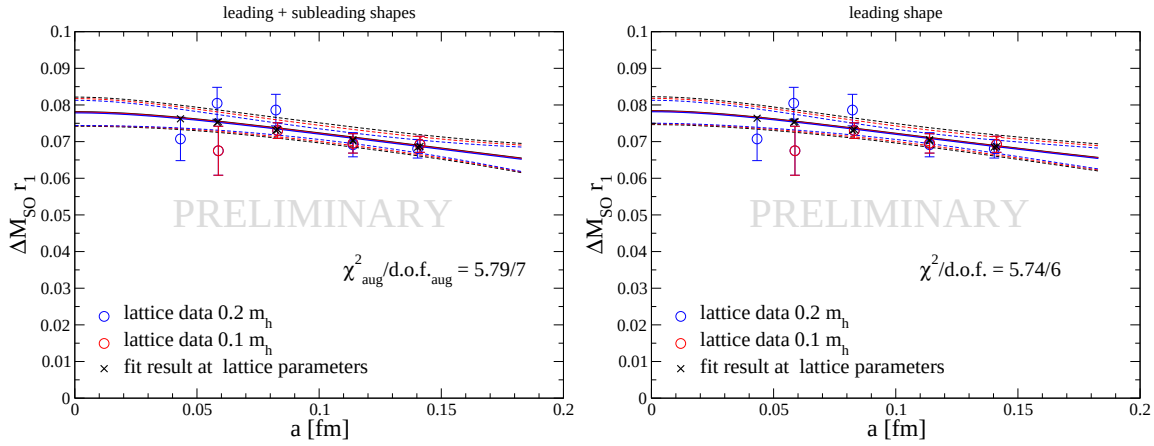

Figure 4.6. Chiral and continuum fit for the 1P spin-orbit splitting [8, 9]. For an explanation, see caption of Fig. 4.4.

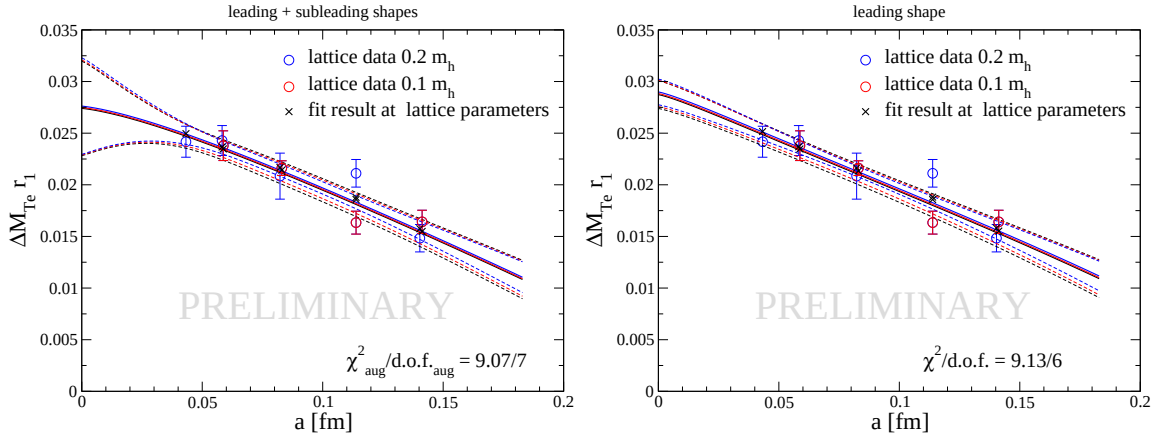

Figure 4.7. Chiral and continuum fit for the 1P tensor splitting [8,9]. For an explanation, see caption of Fig. 4.4.

Table 4.7. Charmonium mass splittings compared with the experimental values [9]. The first column shows the mass splittings. The second column lists the resultant chiral-continuum extrapolated mass splitting values, calculated on the lattice [9]. The third column displays the experimental values acquired from particle data group [5].

Mass difference	Lattice [MeV] [9]	Experiment [MeV] [5]
1P-1S splitting	457.3 ± 3.6	457.5 ± 0.3
1S hyperfine	$118.1 \pm 2.1^{-1.5}_{-4.0}$	113.2 ± 0.7
1P spin-orbit	49.5 ± 2.5	46.6 ± 0.1
1P tensor	17.3 ± 2.9	16.25 ± 0.07
1P hyperfine	-6.2 ± 4.1	-0.10 ± 0.22

CHAPTER 5

VARIATIONAL METHOD FOR STAGGERED FERMIONS

I have introduced the conventional variational method [47, 48] in Chap. 3, used for the action with improved Wilson fermions. However, the method has not been used for the alternative lattice formalism that we use, namely staggered fermions, which does not have a conventional single-time-step transfer matrix, neither has any quantitative variational analysis been performed . Nonetheless, with a simple modification, the variational method can be applied to the staggered action as well [97]. In this chapter, I introduce our modified staggered variational method and analyze the D_s spectrum as a case study. This dissertation describes the work published in Ref. [97].

5.1 Staggered fermions

Unlike clover fermions, the hadronic correlator involving staggered fermions includes time oscillating terms in its multiexponential expansion

$$C_{ij}(t) = \sum_n \langle 0|\mathcal{O}_i(t)|n\rangle s_n(t) e^{-E_n t} \langle n|\mathcal{O}_j^\dagger(0)|0\rangle \,. \tag{5.1}$$

where $s_n(t) = 1$ for the nonoscillating states and $s_n(t) = (-1)^t$ for the oscillating states. The oscillating part is usually called the parity partner of the nonoscillating state, because often the states appear as a pair and have opposite parities.

In this study, we are interested in the meson correlator formed from interpolating operators involving staggered (light) and Wilson (heavy) fermions. To construct such correlators, we first convert the staggered propagator into the "naive" propagator,

$$N(x', x) = \Gamma^\dagger(x')\Gamma(x) S(x', x) \,, \tag{5.2}$$

where, in one convention,

$$\Gamma(x) = \gamma^{x_1}\gamma^{x_2}\gamma^{x_3}\gamma^{x_0} \,, \tag{5.3}$$

and $S(x', x)$ is an improved staggered fermion propagator. The naive propagator carries both color and spin indices, so that we can use the bilinear gamma matrices Γ_A and Γ_B on the source and sink, respectively. The resulting correlator is

$$C(t) = \sum_{\mathbf{x}} \mathrm{Tr}[\Gamma_B N(x', x) \Gamma_A^\dagger W(x, x')] \tag{5.4}$$

where the trace is over both spins and colors.

Now, consider a correlator $C'(t)$ in which the bilinear gamma matrices Γ_A and Γ_B are replaced by $\Gamma_A\gamma_0\gamma_5$ and $\Gamma_B\gamma_0\gamma_5$, respectively. This transformation preserves the angular momentum, but reverses the parity and charge conjugation. One can show that

$$C'(t) = C(t)(-)^t \,. \tag{5.5}$$

because

$$\gamma_0\gamma_5 N(x', x) = (-)^{t'-t} N(x', x)\gamma_0\gamma_5 \,. \tag{5.6}$$

Therefore, a Wilson-plus-staggered hadronic correlator involving Γ_A and Γ_B at the source and sink, respectively, is identical to the correlator involving $\Gamma_A\gamma_0\gamma_5$ and $\Gamma_B\gamma_0\gamma_5$, up to the sign-oscillating factor in time. Moreover, if $\mathcal{O}_i$ is constructed from a hermitian bilinear with gamma matrix Γ_A, the operator constructed from $\Gamma_A\gamma_0\gamma_5$ is antihermitian. Thus,

$$\langle n|\mathcal{O}_i(0)|0\rangle = -\langle 0|\mathcal{O}_i^\dagger(0)|n\rangle \,. \tag{5.7}$$

As a result, the correlator involving staggered propagators includes an overall minus sign due to antihermiticity as noted above when it has an oscillating factor $(-)^t$.

Thus, the correlation matrix involving the single-time-slice Dirac-plus-staggered meson has the form:

$$C(t) = ZT^t g Z^\dagger \,, \tag{5.8}$$

where $T = \mathrm{diag}[e^{-E_n}]$ and $g = \mathrm{diag}[s_n(1)]$, that is, a diagonal matrix with a plus (minus) sign for nonoscillating (oscillating) states. Then, with the same steps as in Eq. (3.116) and (3.116), we can get the same expression of GEVP as the Wilson fermion correlator

$$C(t)u_n = \lambda_n(t, t_0)C(t_0)u_n \,, \tag{5.9}$$

but unlike the Wilson correlation matrix, the eigenvalues can be negative. Here, we modify the ordering convention so that the eigenvalues are in decreasing order according to their absolute values, $|\lambda_n(t, t_0)| > |\lambda_{n+1}(t, t_0)|$. At large t, the eigenvalues have form,

$$\lambda_n(t, t_0) = s_n(t - t_0)e^{-E_n(t-t_0)} \,. \tag{5.10}$$

However, at non-asymptotic t, because the hadronic correlator calculated on the lattice can be expanded as an infinite sum of exponentials, the eigenvalue in Eq. (5.10) must have

correction terms. The ALPHA Collaboration quantitatively estimates the corrections to the large time asymptotics by using perturbation theory [48]. Let N denote the number of interpolating operators in use and separate the hadronic correlation matrix, $C(t)$, into two parts,

$$C(t) = C^{(N)}(t) + C'(t)\,, \tag{5.11}$$

where $C^{(N)}(t)$ is the truncated correlation matrix where each matrix element has a finite number of exponentials, N, whereas $C'(t)$ includes the exponentials from $N+1$-th to ∞. Then, the eigenvalues of the GEVP constructed from $C^{(N)}(t)$ are exactly given by Eq. (5.10). Now, because the transfer matrix decrease exponentially, we can treat the effects of $C'(t)$ perturbatively. As a result, one can show that the corrections to the large time asymptotics due to truncation of the correlation matrix have the form [97]

$$\begin{aligned}
\lambda_n(t,t_0) &\approx s_n(t-t_0)(1-a_n(t_0))e^{-E_n(t-t_0)} \\
&+ \sum_{m>n}^{N} b_{m,n}(t_0)s_m(t-t_0)e^{-E_m(t-t_0)} \\
&- \sum_{m<n}^{N} b_{m,n}(t_0)s_m(t-t_0)e^{-(2E_n-E_m)(t-t_0)} + \mathcal{O}(e^{-E_{N+1}(t-t_0)})\,.
\end{aligned} \tag{5.12}$$

The coefficients a_n and $b_{m,n}$ depend only upon the reference time t_0:

$$\begin{aligned}
a_n(t_0) &\approx A_{n,n,N+1}s_n(t_0)s_{N+1}(t_0)e^{-(E_{N+1}-E_n)t_0} \\
&- \left[e^{-2(E_{N+1}-E_n)t_0}|A_{n,n,N+1}|^2 + \sum_{m>n}^{N} b_{n,m,N+1}(t_0)\right]
\end{aligned} \tag{5.13}$$

$$b_{m,n}(t_0) \approx |A_{m,n,N+1}|^2 s_n(t_0)s_m(t_0)e^{-(2E_{N+1}-E_n-E_m)t_0}\,, \tag{5.14}$$

where $A_{m,n,N+1}$ is given by the product of overlaps

$$A_{m,n,N+1} = \left(\sum_{i=1}^{N} u^*_{m,i}Z_{i,N+1}\right)\left(\sum_{i=1}^{N} Z^*_{i,N+1}u_{n,i}\right)\,. \tag{5.15}$$

As the number N of linearly independent interpolating operators is increased with fixed t_0 and t, the factors $e^{-(E_N-E_n)t_0}$ decrease exponentially, so a_n and b_n vanish exponentially. On the other hand, with fixed N, as the reference time t_0 becomes large, the coefficients also decrease exponentially. Therefore, we can suppress the correction terms by increasing N and t_0 so that we get Eq. (5.10) at fixed time slice t.

In practice, however, for a hadronic excited state, it is challenging to get a good signal at a large t_0, and making N large is expensive. Therefore, rather than requiring the correction

term to vanish, we propose fitting the eigenvalues to a simpler form containing oscillating and nonoscillating correction terms,

$$\begin{aligned}\lambda_n(t,t_0) &\approx [1-a_n(t_0)]s_n(t-t_0)e^{-E_n(t-t_0)} + b_n(t_0)s_n(t-t_0)e^{-\bar{E}_n(t-t_0)} + \\ &+ c_n(t_0)s'_n(t-t_0)e^{-E'_n(t-t_0)} + d_n(t_0)s'_n(t-t_0)e^{-\bar{E}'_n(t-t_0)}\,, \end{aligned} \tag{5.16}$$

where $s'_n(t)$ oscillates if $s_n(t)$ does not, and vice versa. Thus, depending on t_0, $\bar{E}_n$, E'_n or $\bar{E}'_n$ could be either E_m where $m > n$ or $2E_n - E_m$ where $m < n$. We arrange so that the principal term, *i.e.*, the term with the largest amplitude, is the one with coefficient $1 - a_n(t_0)$. Also, because $\lambda_n(t_0, t_0) = 1$, it is useful to impose the sum rule [84],

$$\Sigma_n \equiv 1 - a_n(t_0) + b_n(t_0) + c_n(t_0) + d_n(t_0) \approx 1\,. \tag{5.17}$$

From Eq. (5.13), we see that the parity partner energy is either $E'_n = E_m$ or $E'_n = 2E_n - E_m$, where E_m is the energy of a nearby state. In principle, the same choices apply to the excited state values $\bar{E}_n$ and $\bar{E}'_n$, but in practice, these energies could represent a weighted average of an array of possible states, including the lowest excluded state E_{N+1}.

5.2 Case study: D_s meson spectrum

In this chapter, I illustrate the method by calculating D_s meson spectrum. While the previous studies implementing the variational method have been done with only the clover quark and antiquark formalism [98–102], in this study, we use the staggered strange antiquark and clover (Fermilab) charm quark.

5.2.1 Simulation setup

We work with the MILC ensemble with lattice spacing $a = 0.15089(17)$ [103] fm, generated in the presence of $2 + 1 + 1$ flavors of highly improved staggered sea quarks (HISQ), *i.e.,* equal up and down sea quark masses, plus strange and charm sea quarks with all masses approximately equal to their physical values [104]. The lattice dimension is $32^3 \times 48$. We measured the charm-strange meson correlator on 988 gauge configurations separated by six molecular dynamics time units with eight uniformly spaced source times per configuration. The charm-strange mesons were constructed with a clover (Fermilab) charm quark and a strange HISQ with mass equal to the strange sea quark in the ensemble. We also measured the charmonium correlator to set the charm quark mass. For the more detailed charm-quark tuning description, refer to Sec. 6.3.

To construct the charm-strange meson, we consider a variety of single-time-slice, zero-momentum interpolating operators $\mathcal{O}_i$ of the form

$$\mathcal{O}_i(t) = \sum_x \bar{Q}(\boldsymbol{x}, t) J_i q(\boldsymbol{x}, t)\,. \tag{5.18}$$

where Q is the clover charm quark field and q is the HISQ field, converted by standard methods to a "naive" Dirac field according to Eq. (5.2). Both fields carry suppressed Dirac spin and color indices. The current operators J_i in this study are listed in Table 5.1. We introduce three types of covariant Gaussian smearing to implement wave functions mimicking both $1S$ ground state and other excited states. These Gaussian smearings are defined in Eq. (4.22), which in terms of the gauge-covariant Dirac operator $\not{D}$ and a smearing width r_x:

$$S_x = \exp(r_x^2 \not{D}^2/4) \tag{5.19}$$

for $x = a, b, c$ with widths $r_a = 0$ (plain stochastic wall source), $r_b = 1.6$ (only clover quark smeared to the stochastic wall source), and $r_c = \sqrt{2r_b^2} = 2.2$ (both clover and staggered quarks smeared).

5.2.2 Effective energies from generalized eigenvalues

As we have noted, by solving the GEVP, the states belonging to the channels characterized by the opposite-parity irreducible representations (irreps) A_1^+, T_1^+, and T_2^- can be extracted as the parity partners of states in the irreps A_1^-, T_1^-, and T_2^+. Thus, we can extract effective masses for two channels from a single channel eigenvalues. These effective masses are useful from two perspectives. First, as mentioned in Sec. 3.5.1, one can roughly estimate energy levels, E_n, from the eigenvalues λ_n at $t \gg 1$, and these are guides for

Table 5.1. Current operators J_i for constructing interpolating operators $\bar{Q}(\mathbf{x}, t) J_i q(\mathbf{x}, t)$ for the charm-strange mesons in this study for each of the indicated irreps of the octahedral group (with spatial inversions): O_h. All interpolating fields used here are constructed by the same way as introduced in Chap. 4.

A_1^-	T_1^-	T_2^+
$\gamma_5 \cdot S_{a,c}$	$\gamma_i \cdot S_{a,b,c}$	$\lvert\varepsilon_{ijk}\rvert\, \gamma_j \nabla_k$
$\gamma_t\gamma_5 \cdot S_{a,c}$	$\gamma_t\gamma_i \cdot S_{a,b,c}$	$\lvert\varepsilon_{ijk}\rvert\, \gamma_t\gamma_j \nabla_k$
$\gamma_5\gamma_i \cdot \nabla_i$	$\boldsymbol{I} \cdot \nabla_i$	
$\gamma_t\gamma_5\gamma_i \cdot \nabla_i$	$\gamma_t \cdot \nabla_i$	
	$\varepsilon_{ijk}\gamma_5\gamma_j \nabla_k$	
	$\varepsilon_{ijk}\gamma_t\gamma_5\gamma_j \nabla_k$	

the eigenvalue fitting. Second, one can identify the principal state with definite quantum number from the eigenvalue E_n. To see how this works, consider the effective mass formulas given as

$$E_{\rm eff}^{(k)}(t) = \log\left[\lambda^{(k)}(t+1)/\lambda^{(k)}(t)\right] \quad \text{Nonoscillating states} \tag{5.20}$$

$$E_{\rm eff}^{(k)}(t) = \log\left[-\lambda^{(k)}(t+1)/\lambda^{(k)}(t)\right] \quad \text{Oscillating states}. \tag{5.21}$$

In either case, we find it helpful to smooth the result:

$$\mathcal{E}_{\rm eff}^{(k)} = \frac{1}{4}\left[E_{\rm eff}^{(k)}(t+1) - 2E_{\rm eff}^{(k)}(t) + E_{\rm eff}^{(k)}(t-1)\right]. \tag{5.22}$$

where the oscillating (nonoscillating) states are averaged out, if we use Eq. (5.20) (Eq. (5.21)).

In fact, including all interpolating operators in many cases permits a clean isolation of the parity partners. That is, for a given eigenvalue, often only the oscillating or nonoscillating component is robust, and the partner component is too weak to obtain a statistically significant effective mass.

Figure 5.1 shows the resultant effective masses. We set the reference time $t_0 = 3$ (4 in the case of T_2^+), where the reference times are chosen large enough to suppress other redundant states, but small enough to get statistically good signals for the eigenvalues. In the variational calculation, we include all operators in the respective columns of Table 5.1, and we examine results for all six channels $A_1^\pm$, $T_1^\pm$, and $T_2^\pm$. These single-time-slice operators generate states of both parities. The parity indicated in Table 5.1 is for the nonoscillating state. The resulting effective energies (masses in our zero-momentum case) for both parities are plotted in Fig. 5.1 as a function of t and tabulated in Table 5.2.

As mentioned in the previous section, we set the ordering convention of the eigenvalues so that they are in decreasing order according to their magnitudes $|\lambda_n(t,t_0)| > |\lambda_{n+1}(t,t_0)|$ for large t and t_0. As a result, for the eigenvalues of A_1^- channel, the ground and the second excited states appear as $J^P = A_1^-$ (nonoscillating states), and the first excited state is $J^P = A_1^+$ (oscillating state). For the eigenvalues of T_1^- channel, the ground, the third, and the fourth states appear as $J^P = T_1^-$ (nonoscillating states) and the first and the second excited states appear as $J^P = T_1^+$ (oscillating states). Finally, for the eigenvalues of T_2^+ channel, the quantum number of the ground state is $J^P = T_2^+$ (nonoscillating) and the first excited state is $J^P = T_2^-$ (oscillating).

Finally, we can tentatively assign a continuum quantum number according to Table 3.1. J^P of the nonoscillating states extracted from A_1^-, T_1^-, and T_2^+ are assigned to 0^-, 1^-, and 2^+, respectively, and J^P of the oscillating states are assigned to the same total angular

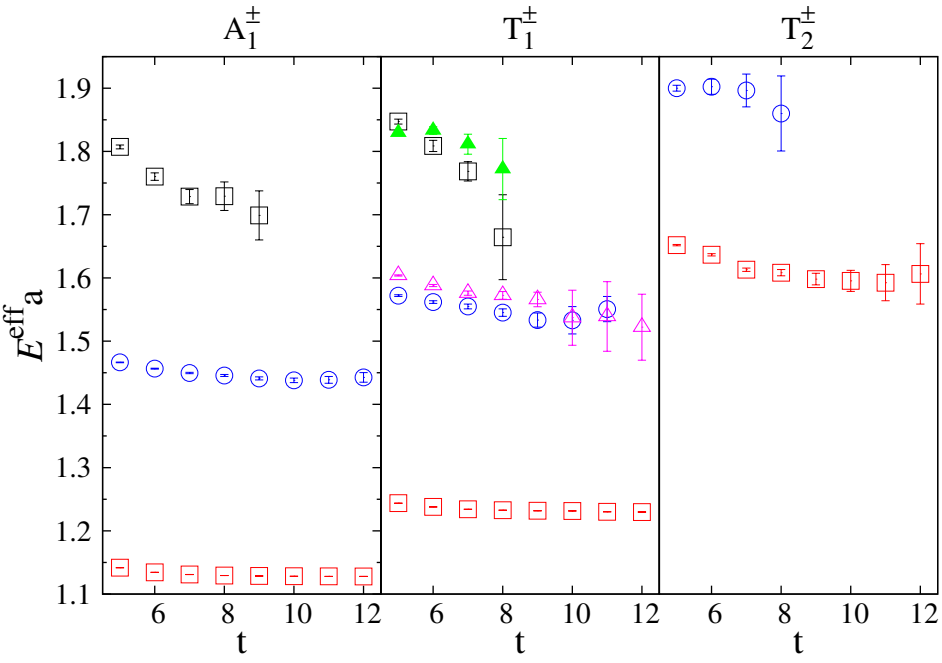

Figure 5.1. Smoothed effective masses $\mathcal{E}_{\rm eff}$ from the the eigenvalues in the $A_1^{\pm}$, $T_1^{\pm}$, and $T_2^{\pm}$ charm-strange channels as a function of t. All interpolating operators listed in Table 5.1 are used. The reference times are $t_0 = 3$ for $A_1^{\pm}$, $T_1^{\pm}$, and $t_0 = 4$ for $T_2^{\pm}$, which are about 0.45 fm and 0.6 fm, respectively. For all channels, the red squares represent the nonoscillating ground states, the blue circles represent the oscillating first excited states (the purple triangle for the oscillating second excited in $T_1^{\pm}$ channels), and the black squares represent nonoscillating further higher excited state. One additional nonoscillating excited state is shown as green filled dots in $T_1^{\pm}$ channels.

momentum, but opposite parities. See the fourth column of Table 5.2 for the assignment, and the next column shows the the corresponding hadronic states assigned according to their quantum numbers.

5.2.3 Results

Even though we are working at only one lattice spacing with quark masses close, but not finely tuned, to their physical values, and we have not considered effects of two-meson channels, it is tempting to compare our results with the experimentally known masses [5]. This is done in Table 5.3 and Fig. 5.2, including tentative assignments. To extract the energy levels, we use the all interpolating operators listed in Table 5.1 for all channels. The resultant values of fit parameters, a_n, b_n, c_n, d_n, E_n, $\bar{E}_n$, E'_n, and $\bar{E}'_n$ defined in Eq. (5.16) are displayed in Table 5.4 and the fit information is displayed in Table 5.5.

Our study also had an interesting result. The traditional folklore is that staggered

Table 5.2. Classification of states identified from their effective masses shown in Fig. 5.1. Listed are the eigenvalue indices, whether the principal state is obtained from the oscillating (O) or nonoscillating (NO) effective mass, the plot symbol, the inferred O_h irreducible representation and continuum spin/parity, and the assigned hadronic state [5], if obvious.

n	NO/O	plot symbol	J^P	assignment
		$A_1^\pm$		
0	NO	red squares	A_1^-, 0^-	D_s
1	O	blue circles	A_1^+, 0^+	$D_{s0}^*(2317)$
2	NO	black squares	A_1^-, 0^-	?
		$T_1^\pm$		
0	NO	red squares	T_1^-, 1^-	D_s^*
1	O	blue circles	T_1^+, 1^+	$D_{s1}(2460)$
2	O	purple triangles	T_1^+, 1^+	$D_{s1}(2536)$
3	NO	black squares	T_1^-, 1^-	$D_{s1}^*(2700)$
4	NO	green triangles	T_1^-, 1^-	?
		$T_2^\pm$		
0	NO	red squares	T_2^+, 2^+	$D_{s2}^*(2573)$
1	O	blue circles	T_2^-, 2^-	?

Table 5.3. Mass splittings in the D_s spectrum. The experimental splittings are calculated relative to the spin-averaged D_s $1S$ state, based on values in Ref. [5].

	Experiment [MeV]	Lattice [MeV]
$D_s^* - D_s$	143.8 ± 0.4	134.77 ± 0.51
$D_s - \overline{1S}$	-107.9 ± 0.5	-101.08 ± 0.38
$D_s^* - \overline{1S}$	35.9 ± 0.6	33.69 ± 0.13
$D_{s1}^*(2700) - \overline{1S}$	632.7 ± 4	698.9 ± 38.4
$D_{s0}(2317) - \overline{1S}$	241.5 ± 0.7	302.6 ± 6.3
$D_{s1}(2460) - \overline{1S}$	383.3 ± 0.7	436.2 ± 15.0
$D_{s1}(2536) - \overline{1S}$	458.8 ± 0.4	478.5 ± 13.1
$D_{s2}(2573) - \overline{1S}$	496.3 ± 1.0	508.9 ± 18.3

fermion correlators always have both parity partners whenever they exist. However, with the variational method, we can isolate them, given a large enough variational basis. In the rest of this section, we examine the progressive isolation as the dimension N of the interpolating operator basis is increased or as the reference time t_0 is increased. To do this, we fit the eigenvalues to our preferred model Eq. (5.16), and, for each eigenvalue, we study the effect on the principal amplitude $1 - a_n$ and mass M_n. However, here, we just summarize the study. The detailed discussion can be found in Ref. [97].

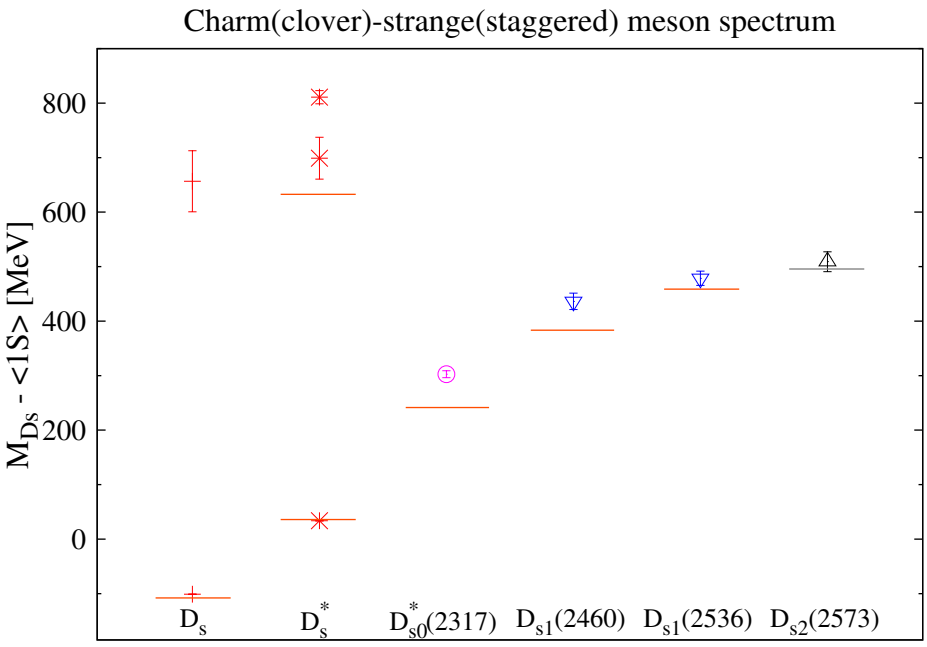

Figure 5.2. Comparison of our crude theoretical charm-antistrange meson spectrum (symbols with errors) with experimental values (short horizontal lines) with tentative assignments of the levels. Mass splittings are shown relative to the spin-averaged D_s $1S$ state, namely $\overline{1S} = \frac{1}{4}(D_s + 3D_s^*)$.

For both $A_1^\pm$ and $T_1^\pm$ channels, in panels (A,C) shown in Figs. 5.3 and 5.4, they show progressive improvement in the isolation of parity partner eigenstates with the increasing dimension N of the interpolating operator basis and with the increasing reference time t_0. We find, as expected, that as N increases in this way with fixed $t_0 = 3$, the amplitude $1 - a_n$ approaches 1 and the mass M_n stabilizes. Also, as t_0 increases at fixed N, the amplitude $1 - a_n$ also approaches 1, and the mass M_n stabilizes. In this case, we can be more quantitative. From Eqs. (5.13), (5.13), and (5.14), we see that the coefficient a_n in Eq. (5.16) all tend to decrease exponentially with t_0 at fixed N as

$$e^{-(E_{N+1}-E_n)t_0} A_{n,n,N+1}\,, \tag{5.23}$$

whereas the coefficients b_n, c_n, and d_n decrease exponentially according to

$$e^{-2(E_{N+1}-E_n)t_0} A^2_{n,m,N+1}\,. \tag{5.24}$$

We note that at fixed N, the coefficient $A^2_{n,m,N+1}$ is constant. Indeed, as shown in Figs. 5.3 and 5.4 panel C, the coefficient $1-a_n$ can be fit with the exponential form $1-r_n \exp(-\Delta M_n t_0)$, where r_n and ΔM_n are adjusted to their best fit values.

Table 5.4. Fit results for the eigenvalues of the $A_1^{\pm}$, $T_1^{\pm}$, and $T_2^{\pm}$ channels with all A_1^-, T_1^-, and T_2^+ operators in Table 5.1, respectively. For $A_1^{\pm}$ and $T_1^{\pm}$ channels, we use reference time $t_0 = 3$ and for $T_2^{\pm}$ channel, $t_0 = 4$. The fit parameters a_n, b_n, c_n, d_n, E_n, $\bar{E}_n$, E'_n, and $\bar{E}'_n$ are defined in Eq. (5.16). The fit information is displayed in Table 5.5. Note that only for the ground state of the A_1^- channel, we use the further additional exponential term, $\tilde{b}_n\tilde{E}_n$, not shown in Eq. (5.16), which is classified by nonoscillating state.

$A_1^{\pm}$ channel

n	$1-a_n$	E_n	b_n	$\bar{E}_n$	$\tilde{b}_n$	$\tilde{E}_n$	c_n	E'_n
0	0.889(4)	1.1274(3)	0.0144(4)	1.40(26)	0.089(11)	1.99(11)	−0.0010(9)	1.67(30)
1	0.810(31)	1.4361(46)	0.173(3)	1.855(87)	–	–	−0.0039(18)	1.67(17)
2	0.558(51)	1.723(18)	0.441(6)	2.66(28)	–	–	−0.081(19)	2.005(86)

$T_1^{\pm}$ channel

n	$1-a_n$	E_n	b_n	$\bar{E}_n$	c_n	E'_n	d_n	$\bar{E}'_n$
0	0.872(2)	1.2305(3)	0.0856(3)	1.879(35)	−0.0108(8)	1.586(28)	–	–
1	0.774(80)	1.538(12)	0.187(6)	1.94(19)	−0.012(3)	1.59(10)	–	–
2	0.761(47)	1.569(10)	0.256(17)	2.44(66)	−0.0020(29)	1.27(25)	−0.06(19)	2.6(1.8)
3	0.529(90)	1.739(31)	0.482(4)	2.34(12)	−0.017(3)	1.556(68)	–	–
4	0.720(23)	1.8248(89)	0.504(3)	4.11(55)	−0.22(5)	2.323(91)	–	–

$T_2^{\pm}$ channel

n	$1-a_n$	E_n	b_n	$\bar{E}_n$	c_n	E'_n	d_n	$\bar{E}'_n$
0	1.01(11)	1.594(16)	0.338(6)	2.17(27)	−0.34(15)	1.890(18)	–	–
1	1.34(3)	1.903(12)	–	–	−0.35(4)	2.11(7)	–	–

Unlike the $A_1^{\pm}$ channel, the $T_1^{\pm}$ channel has two fairly closely spaced T_1^+ states. Therefore, the oscillating term in λ_0 with fewer interpolators could represent a mixture of both. Including more interpolating operators helps partly in separating the states, but λ_0 for that set still has a strong oscillating component. A nearly complete separation occurs only after nine or more operators are included. Then, λ_0 contains only the nonoscillating state and the two oscillating states appear separately in λ_1 and λ_2.

On the other hand, for $T_2^{\pm}$ channel, because there are only a few interpolating operators, the parity partners are not well separated even at $t_0 = 4$. Thus, even at reasonably low t_0, the multiexponential fit again helps to compensate for contamination from other unsuppressed exponential contributions.

Table 5.5. Fit information for the eigenvalues of the $A_1^{\pm}$, $T_1^{\pm}$, and $T_2^{\pm}$ channels. The sum of amplitudes of exponentials used for fitting, Σ_n, represents $1 - a_n + b_n + c_n + d_n$ as in Eq. (5.17). The next column shows its prior central value and width for the Σ_n. We found that it is close to 1, as expected from the sum rule of Eq. (5.17), as long as N is large enough.

	n	NO/O	Σ_n	prior $\pm$ width	fit type	fit range	χ^2/d.o.f
A_1^-	0	NO	0.992(3)	1 ± 0.1	4-exp	4-20	5.5/9
	1	O	0.978(5)	1 ± 0.1	3-exp	4-18	7.3/9
	2	NO	0.944(87)	1 ± 0.1	3-exp	4-11	3.3/2
T_1^-	0	NO	0.962(2)	1 ± 0.1	3-exp	4-20	11.2/11
	1	O	0.952(11)	1 ± 0.1	3-exp	4-17	5.2/8
	2	O	0.948(58)	1 ± 0.1	4-exp	4-13	0.9/2
	3	NO	0.994(19)	1 ± 0.02	3-exp	4-10	2.2/1
	4	NO	0.991(99)	1 ± 0.1	3-exp	4-11	1.3/2
T_2^+	0	NO	1.009(60)	1 ± 0.08	3-exp	5-15	4.1/5
	1	O	0.99(1)	–	2-exp	5-13	4.5/5

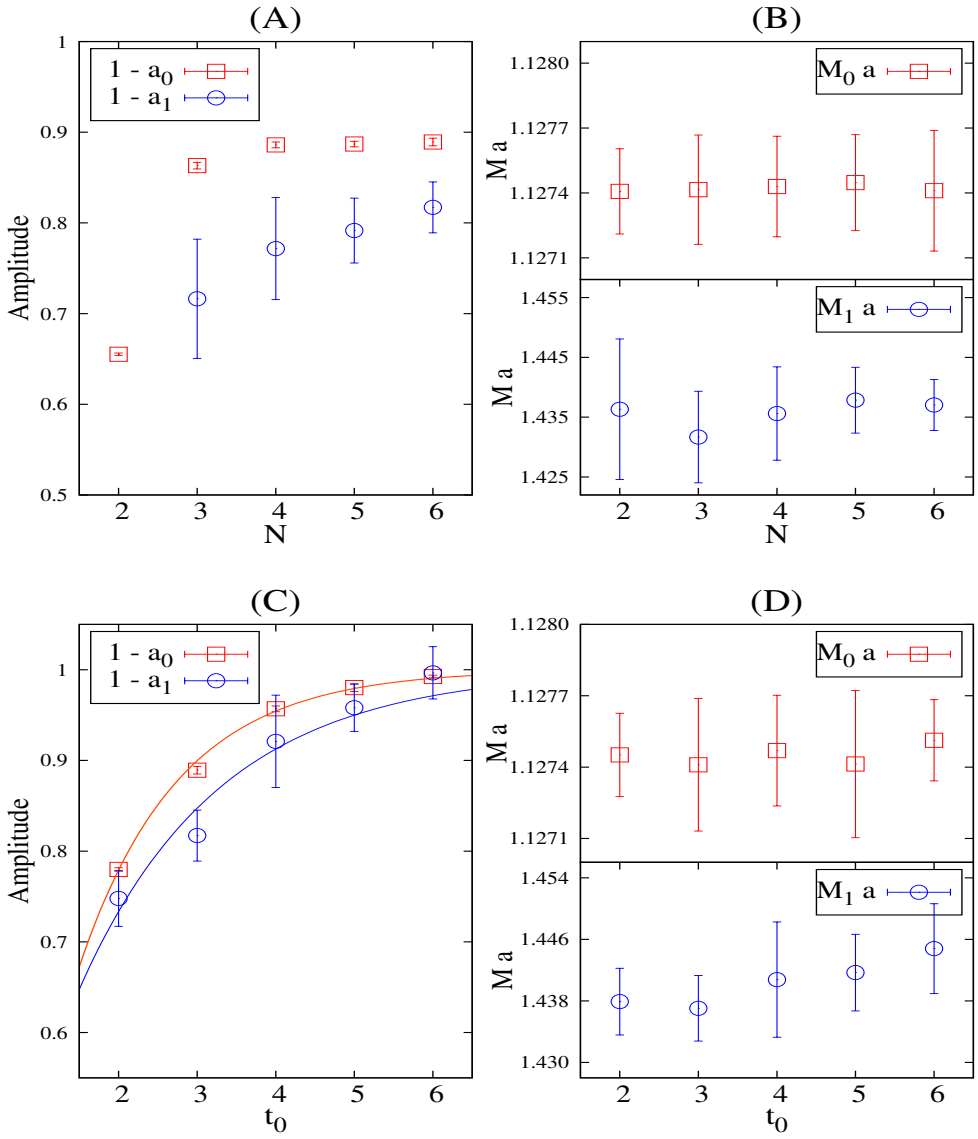

Figure 5.3. Progressive isolation of the parity partner eigenstates with the increasing dimension N of the interpolating operator basis. Improvement is demonstrated for the two leading eigenvalues λ_0 and λ_1 in the $A_1^{\pm}$ channels by examining the principal coefficients and masses from a fit to Eq. (5.16). Panels A and C show the principal fit coefficients $1-a_0$ and $1-a_1$ and panels B and D, the masses $M_0 = E_0$ and $M_1 = E_1$ as a function of (A,B) the number of interpolating operators N and (C,D) the reference time t_0. The solid lines represent a fit to the function $1 r_n e^{-\Delta M_n t_0}$, adjusting both r_n and M_n.

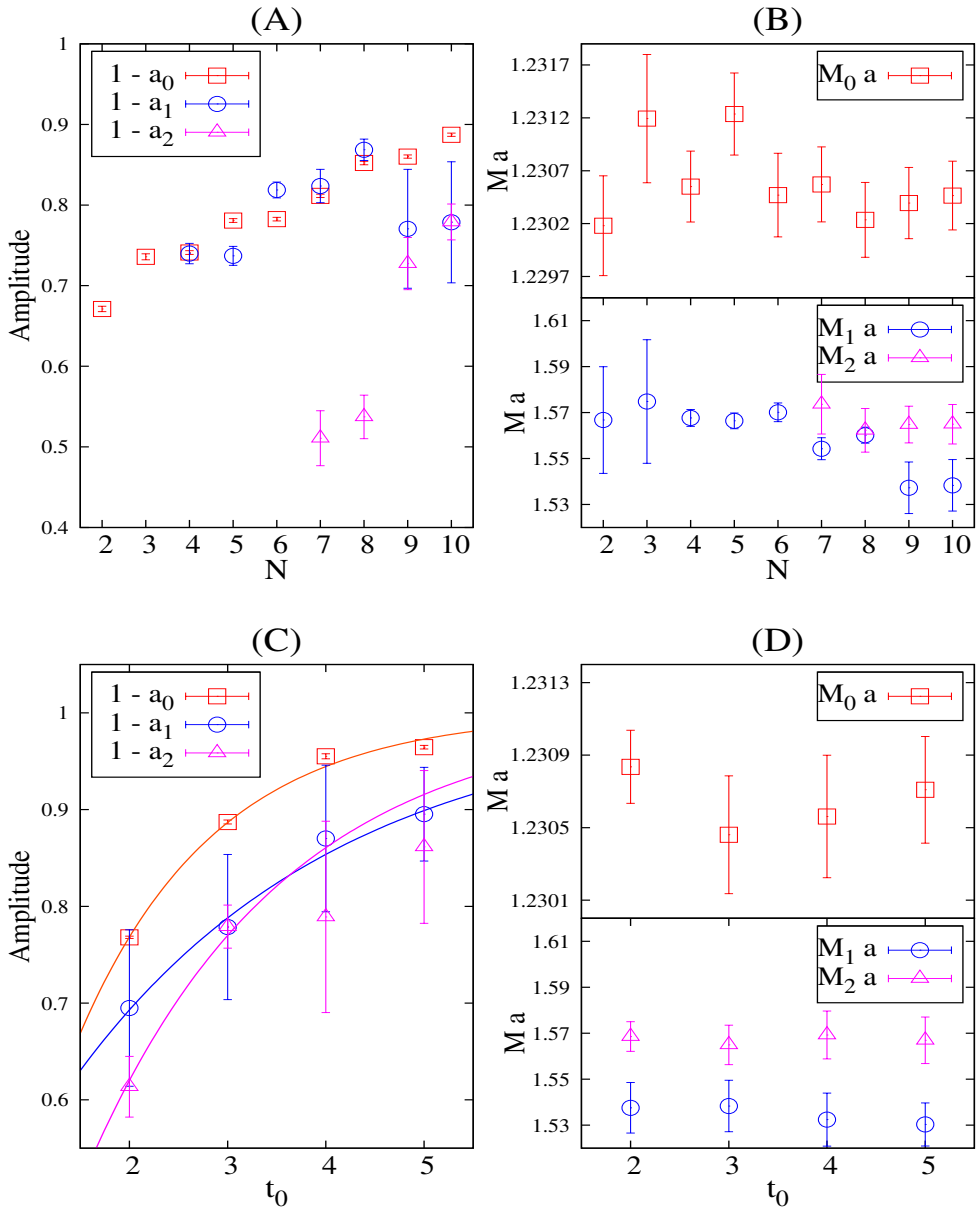

Figure 5.4. As in Fig. 5.3, but for the lowest two states in the $T_1^{\pm}$ channels. The operator sets are defined in the text.

CHAPTER 6

X(3872)

In this chapter, I briefly introduce the charmonium-like state $X(3872)$ and report on our lattice calculation results and analysis for the $X(3872)$ state. The main objective of the analysis is not to calculate the precise theoretical value to match with experimental $X(3872)$ rest masses, but to understand its nature.

6.1 Introduction

As introduced in Chap. 2, the quark model predicts that the minimal baryon configuration is qqq with the SU(3) multiplet representation **1**, **8**, and **10**, whereas the minimal meson configuration is $q\bar{q}$ with the representation **1** and **8**. However, in QCD, the color confinement involving the gluons enables the hadrons to have more complex configurations like tetraquarks ($qq\bar{q}\bar{q}$). Since the first introduction of the tetraquarks by Jaffe [105], many exotic mesons have been found experimentally which cannot be explained by the conventional quark model. For example, in the light quark sector, the scalar mesons $f_0(980)$ and $a_0(980)$ have been proposed to be $K\bar{K}$ molecular states. However, it is challenging to distinguish them from conventional $\bar{q}q$ states because the widths are large and their resonant peaks often overlap conventional states. For rather easier sectors, there are excited charmonium states above or near the threshold. Since excited charmonium states can decay into pairs of D and $\bar{D}$ mesons if their masses are above the threshold for that process, in general, $c\bar{c}$ states near the threshold will undergo mixing with DD (or $D\bar{D}^*$, D^*D^*) molecular or tetraquark states, through creation and annihilation of light quark-antiquark pairs (see Fig. 6.1). Here, the $D\bar{D}$ threshold is often called the "open-charm threshold".

6.2 Charmonium-like states above the open-charm threshold

Many excited states have been discovered that cannot be explained within the conventional quark model. Among those charmonium states, the so-called XYZ mesons are

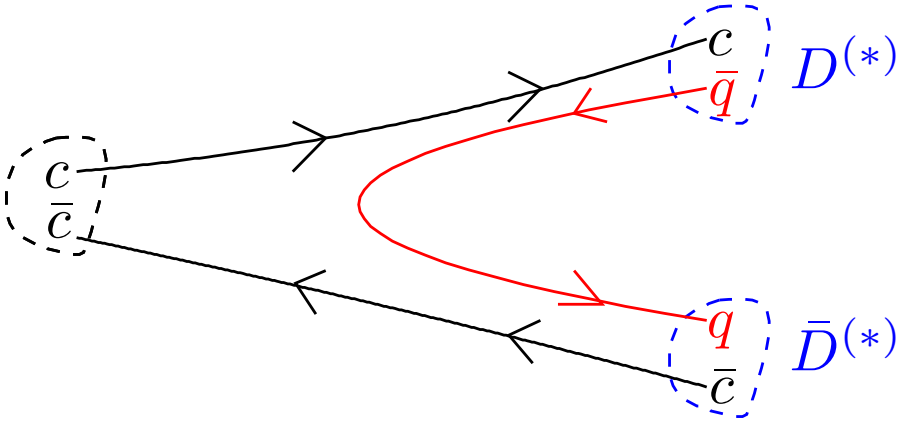

Figure 6.1. A schematic drawing of "open meson" process. $c\bar{c}$ is a charmonium state above the threshold. $c\bar{q}$ ($q\bar{c}$) is D ($\bar{D}$) or D^* ($\bar{D}^*$).

unusual mesons discovered during the last decade that contain heavy $c\bar{c}$ pairs and are above the open-charm threshold. Some of them are

- $X(3872)$, discovered by the Belle Collaboration [106, 107] in 2003 and confirmed by CDF [108] and studied with more precison by CDF [109], D0 [110], BABAR [111,112], and LHCb [113]. Its mass is remarkably close to the $D\bar{D}^*$ threshold – within 1 MeV – and recently, the quantum numbers have been confirmed as $J^{\mathrm{PC}} = 1^{++}$ by LHCb [114]. It decays into both $J/\psi + \rho$ and $J/\psi + \omega$ with comparable branching fraction, which implies a violation of isospin symmetry.

- $Y(4140)$, discovered by the CDF Collaboration in 2009 [115] and studied with more precision by CMS [116], D0 [117], and BaBar [118]. It decays into $J/\psi + \phi$, a promising signature for a spin-exotic hadron with hidden strangeness, leading to the interpretation that $Y(4140)$ might be a $D_s^* D_s^*$ molecule or tetraquark state with valence content $c\bar{c}s\bar{s}$.

- $Z_c^{\pm}(3900)$, observed by the BESIII collaboration [119] in 2013 as an intermediate resonance in an analysis of e^+e^- annihilation into $J\psi\pi^+\pi^-$ at center-of-mass energy $\sqrt{s} = 4260$ MeV. This observation has been confirmed by the Belle Collaboration [120] and by Xiao et al. using data from the CLEO-c detector [121]. However, it has not been observed in exclusive photoproduction of $J/\psi + \pi$ on protons [122] or in conjunction with B_0 decays [123, 124]. It is a charged, isospin-one charmonium-like

state and decays into $J/\psi\pi^+$, which implies that it must include at least four quarks, *i.e.,* a tetraquark or hadronic molecular state with constituents $c\bar{c}u\bar{d}$.

It has been more than a decade since the discovery of the $X(3872)$. However, there is no compelling explanation about its constituents. Theoretical models for the $X(3872)$ mesons can be classified according to their constituents and how they are clustered within the meson.

- *conventional quarkonium*, which consists of a color singlet heavy quark-antiquark pair: $(Q\bar{Q})_1$,
- *quarkonium hybrid*, which consists of a color octet heavy quark-antiquark pair with an excited gluonic degree of freedom: $(Q\bar{Q})_8 + g$,
- *meson molecule*, which consists of two color singlet mesons bound by the strong interaction: $(Q\bar{q})_1 + (\bar{Q}q)_1$,
- *tetraquark*, which consists of a $Q\bar{Q}$ pair and a light quark q and antiquark $\bar{q}$, bound by inter-quark potentials into a color singlet: $(Q\bar{Q}q\bar{q})_1$,
- *diquarkonium*, which consists of a color-antitriplet Qq diquark and a color-triplet $\bar{Q}\bar{q}$ diquark bound by the QCD color force: $(Qq)_{\bar{3}} + (\bar{Q}\bar{q})_3$,
- *quarkonium color-adjoint meson*, which consists of a color-octet $Q\bar{Q}$ pair to which a light quark-antiquark pair is bound: $(Q\bar{Q})_8 + (q\bar{q})_8$.

In this list, the sub-indices 1, 3, and 8 represent the color-singlet, -triplet, and -octet combinations, respectively. As an example, Fig. 6.2 shows a pictorial representation of a meson-molecule state and a tetraquark. All theoretical models listed above could be an explanation of the unusual neutral mesons and the last four of the $Z_c^{\pm}(3900)$.

The goal of this study is to reveal the nature of the $X(3872)$ state by using lattice QCD which is nonperturbative, *ab-initio* method. That is, our study attempts to answer the question - "Is the $X(3872)$ state a the weakly bound state of $D\bar{D}^*$ or not?" Due to the proximity of its mass to the $D\bar{D}^*$ threshold, very often the $X(3872)$ state has been conjectured to be a weakly bound state of $D\bar{D}^*$, and its wave function has a significant molecular component made out of mesons rather than out of quarks. Therefore, we have been studying the $X(3872)$ state on the lattice by allowing the mixing of $c\bar{c}$ and $D\bar{D}^*$ interpolating operators.

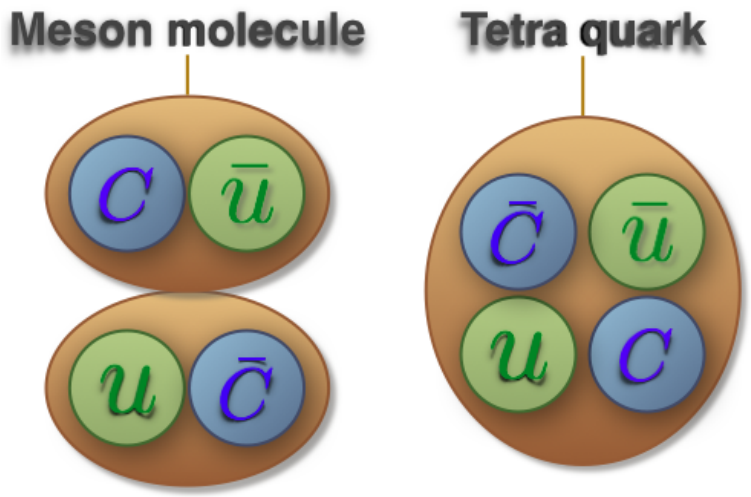

Figure 6.2. Cartoons for the meson molecule and tetraquark state explained in the text.

On a finite volume, all states are discrete, so, on the lattice, bound states are difficult to identify due to finite volume effects. In the case of infinite volume, a bound state is well defined because the bound state spectrum is discrete and scattering states are a continuum. There is no continuum state below the threshold. However, in a finite box on the lattice, all states are discrete – even the lowest energy levels of the elastic scattering state can appear below the threshold if an interaction is attractive between two particles. Therefore, it is difficult to distinguish between the bound state and the lowest scattering state at finite volume. To overcome these difficulties, we implement the finite-volume method [49, 50] introduced in Sec. 3.6 and the effective range formula.

The organization of this chapter is as follows:

- I introduce the gauge configuration details used for this study,
- I describe how we construct the mixing correlation matrix, $c\bar{c}$, $D\bar{D}^*$ for the interpolating operators, namely, the two-, three-, and four-point correlation functions on the lattice,
- I discuss the spectrum results which are extracted from the eigenvalues of the GEVP, based on both the standard and staggered variational method, introduced in Chap 3 and 5, respectively,
- I perform the analysis to determine the nature of the $X(3872)$ by using scattering theory and implementing the finite volume method.

6.3 Simulation setup

We work with the two MILC ensembles, both with lattice spacings approximately 0.15 fm. Both ensembles are generated with highly improved staggered sea quarks (HISQ). The ensembles include degenerate up and down sea quarks. For both ensembles, strange and charm sea quarks have their physical masses [125]. One, ensemble "A", has lattice dimensions $16^3 \times 48$, and the other, ensemble "B", $32^3 \times 48$. On ensemble "A", the light quark masses are approximately 1/5 the strange quark mass and, on ensemble "B", physical light quark masses have their physical values, approximately 1/27 the strange quark mass. When the time separation is large enough for the correlation in a gauge configuration to become negligible, more than one source time can be used for a full set of correlators. Thus, to gain the necessary statistics, we use multiple time sources on each ensemble. We put sources on each of eight time slices per gauge configuration on ensemble "A", and with help of the larger volume advantage, only four time slices on ensemble "B", so in total, there are approximately 8000 and 4000 sources for each ensemble, respectively. We use clover charm quarks within the Fermilab interpretation [86] and HISQ valence light quarks with the masses matching the sea quark masses.

Table 6.1 shows the parameters for both ensembles. On ensemble (A), the charm-quark hopping parameter κ_c has been tuned so that the kinetic mass of the D_s meson is equal to its physical value. On ensemble (B), we use a different charm-quark tuning scheme. It is tuned so that the splitting between the $D + D^*$ and η_c rest masses, $M_D + M_{D^*} - M_{\eta_c}$, is approximately equal to its experimental value, Fig. 6.3. These different tuning schemes result in different charm-quark masses, due to the discretization effects. In the continuum limit, $a \to 0$, however, the charm-quark masses will be consistent, no matter what the tuning scheme is.

As in Chap. 4 and 5, we use (smeared) stochastic wall sources on the source positions for all correlators to gain better statistics and construct charmed heavy-light mesons with nonzero momentum. In addition, we use stochastic sources on the sinks to construct the box diagrams shown in the lower-right corner of Fig. 6.4. We will discuss how we construct the box diagram in Sec. 6.4.3.

6.4 Correlation matrix calculation

To study the $X(3872)$ with $J^{PC} = 1^{++}$, we choose interpolating operators O_i that couple to $c\bar{c}$ as well as $D\bar{D}^*$ scattering states. For $D\bar{D}^*$ interpolating operators, we include states with momentum quanta $(0,0,0)$, and $(0,0,\pm 1)$. See Eq. (6.8) for the zero momentum, and Eq. (6.9) for the nonzero momentum $D\bar{D}^*$ interpolating operators. The quark-line

Table 6.1. Simulation parameters for two ensembles used for $X(3872)$ study. The meaning of each column have been described Chap. 4. Due to the larger volume advantage, we use fewer sources on ensemble (B) than on ensemble (A).

	a(fm)	β	am_l/am_s	$N_s^3 \times N_t$	κ_c	$N_{\text{conf}} \times$ src
Ensemble (A)	~ 0.15	5.80	0.013/0.065	$16^3 \times 48$	0.1220	1020×8
Ensemble (B)	~ 0.15	5.80	0.00235/0.0647	$32^3 \times 48$	0.1256	1040×4

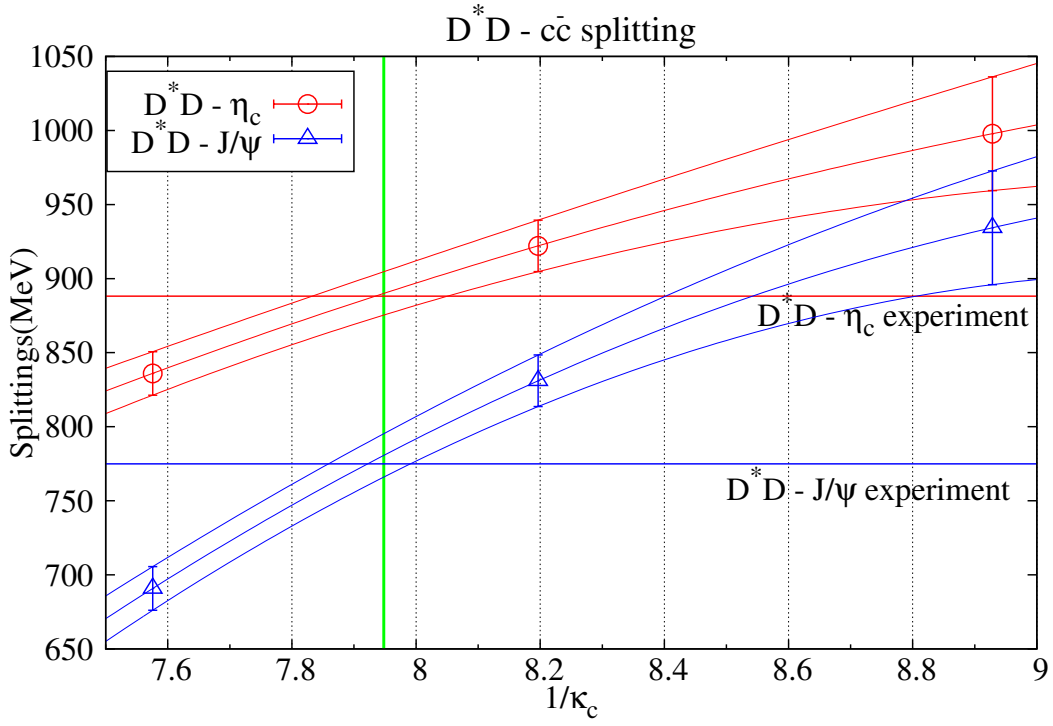

Figure 6.3. The rest mass splitting $M_D + M_{D^*} - M(\eta_c)$ as a function of $1/\kappa_c$, used for tuning the charm quark mass in ensemble (B). The circles and triangles are the lattice data of the splittings between $D\bar{D}^*$ and η_c, and between $D\bar{D}^*$ and J/ψ, respectively. From the left, data are calculated for $\kappa_c = 0.1320$, 0.1220, and 0.1120, respectively. The green vertical line indicates our choice of charm-quark hopping parameter, $\kappa_c = 0.1256^{+0.0021}_{-0.0014}$.

diagrams of the whole mixing correlation matrix included in our calculation are shown in Fig. 6.4. The different smearing levels are omitted for convenience. Black lines represent charm quark propagators (Fermilab) and red lines light quark propagators (HISQ). The prefactors are due to the degeneracy of light-quark (up and down) on lattice. The upper-left corner contains $c\bar{c}$ sectors, the lower-right $D\bar{D}^*$ scattering sectors, and the off-diagonals elements encode the explicit mixing between $c\bar{c}$ and $D\bar{D}^*$. In our simulation, we exclude

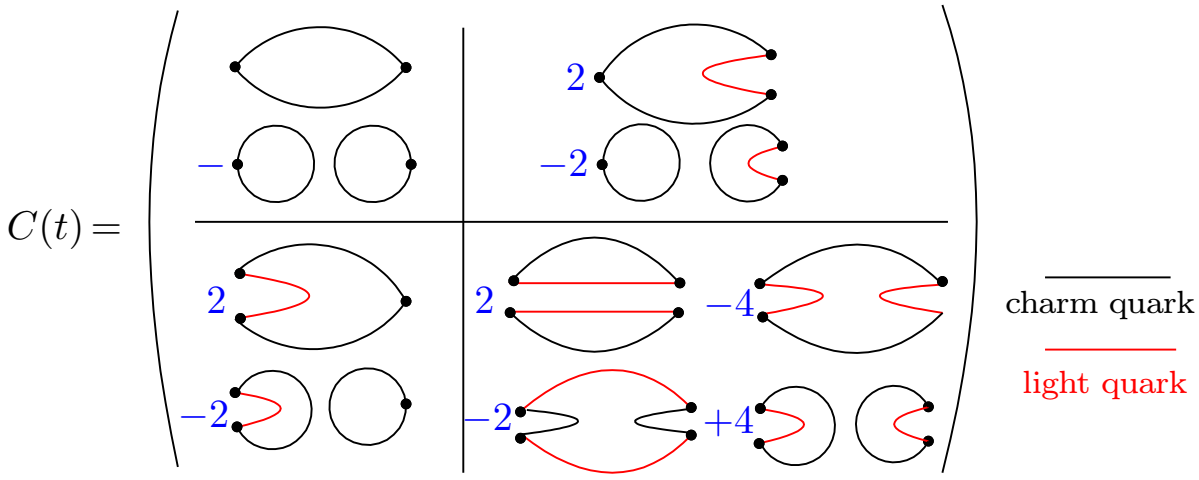

Figure 6.4. $X(3872)$ quark-line diagrams for the hadronic correlator matrix in this simulation. Red lines represent light-quark propagators and black lines, charm-quark propagators. Each prefactor is due to the iso-spin symmetry of up- and down-quarks on the lattice. We do not calculate the charm-quark-annihilation diagrams on the second rows of each sector, because charm-quark annihilation is known to be negligible at our level of precision [10]. According to Wick's theorem introduced in subsection 3.3.1, we denote the upper-left correlation sub-matrix as "two-point correlation functions", the off-diagonal sub-matrices as "three-point correlation functions", and lower-right as "four-point correlation functions". For the four-point correlation functions, there are two types of diagrams. The left one is called the "disconnected diagram", and the right one, the "box diagram", named by their shapes.

charm-quark-annihilation diagrams on the second row of each matrix element, because they are negligible at our level of precision [10]. In this section, we will explicitly show how we construct each correlation matrix - $C_{c\bar{c}\to c\bar{c}}$, $C_{D\bar{D}^*\to c\bar{c}}$ and $C_{D\bar{D}^*\to D\bar{D}^*}$.

6.4.1 Two-point correlation function

In this study, we construct two types of two-point correlators: one is for charmonium and the other heavy-light, D and D^* charmed meson correlators. As Fig. 6.4 shows, charmonium correlators are used in the mixing matrix directly. Heavy-light charmed meson correlators are used in the $D\bar{D}^* \to D\bar{D}^*$ correlator in the bottom right matrix element of Fig. 6.4, and we also need them to measure the kinetic masses of D and D^*.

6.4.1.1 Charmonium correlators

The construction of the charmonium correlation matrix is identical to the one described in Chap. 4. So, in this section, I briefly display the interpolating operators used for this study and mention the physical meaning.

Table 6.2 lists the charmonium interpolating operators used for the $X(3872)$ study. Most of the interpolating operators used in Chap. 4 are also implemented here. Only the Laplacian non-local operator, Δ, is newly introduced, where $\Delta = \nabla^2$, defined in Eq. (3.57), but summed over only spatial lattice sites, $\mu = 1, 2,$ and 3. All steps of the charmonium calculation are exactly the same as Chap. 4. Therefore, we skip the details of the construction of the correlators. Rather, to be consistent with later sections, we simply rewrite the charmonium correlator, $C_{c\bar{c}\to c\bar{c}}(t)$, with propagators :

$$C_{c\bar{c}\to c\bar{c}}(t-t_s) = -\frac{1}{N_R}\sum_{j=1}^{N_R}\sum_{\boldsymbol{x}_1\boldsymbol{x}_2\boldsymbol{y}} \mathrm{Tr}\langle W(t,\boldsymbol{y};t_s,\boldsymbol{x}_1)\xi_j(\boldsymbol{x}_1)\Gamma_{c\bar{c}}\xi_j^*(\boldsymbol{x}_2)W(t_s,\boldsymbol{x}_2;t,\boldsymbol{y})\Gamma_{c\bar{c}}\rangle\,. \quad (6.1)$$

where $\xi(\boldsymbol{x})$ is the stochastic source generated at $\boldsymbol{x}$ at time t_s and $\Gamma_{c\bar{c}}$ indicates the $c\bar{c}$ interpolator listed in Table 6.2. $W(t,\boldsymbol{y};t_s,\boldsymbol{x})$ is the clover charm-quark propagator propagating from the spacetime position, $(t_s,\boldsymbol{x})$, to $(t,\boldsymbol{y})$. Together, with the stochastic source, the propagator is defined through Eq. (3.103), where we suppress color and Dirac spinor indices in Eq. (6.1). In addition, the antiquark propagator propagating from $(t,\boldsymbol{y})$ to $(t_s,\boldsymbol{x})$ can be obtained from

$$W(t_s,\boldsymbol{x};t,\boldsymbol{y}) = \gamma_5 W(t,\boldsymbol{y};t_s,\boldsymbol{x})^\dagger\gamma_5\,. \quad (6.2)$$

The $\mathrm{Tr}\langle\cdots\rangle$ means the trace with respect to the color and spin indices. All interpolators listed in Table 6.2 are used throughout the $C_{c\bar{c}\to c\bar{c}}(t)$ correlators calculations.

6.4.1.2 Heavy-light meson correlators

In this section, we discuss the single D and D^* heavy-light two-point correlator functions. As introduced in Sec. 5.2, we construct the meson correlator in which staggered (light) and Wilson (heavy) fermions are involved in both source and sink positions. However, unlike Sec. 5.2, we do not implement the full-set of the interpolators. It is sufficient to use only a plain stochastic source and covariant Gaussian smeared-quark source field for the D and D^* correlators, because we focus more on extracting ground states with definite momentum, rather than extracting higher excited states.

In Sec. 5.2, to obtain a unique spin-taste assignment, we use the stochastic sources in which quark source fields reside on only the "corner subset" on the lattice, which means the even corner sites sites with x_i even. However, for the case of two particles in the finite box, mainly due to the box-diagram in Fig. 6.4, one cannot project each particle to definite momentum with just the corner subset quark field. Due to this reason and to construct consistent correlators over all diagrams in Fig. 6.4, we use the "full subset" stochastic wall sources for D and D^* two-point correlation functions as well as the three-point and

Table 6.2. Charmonium interpolators used for $X(3872)$ study. Except for Laplacian operator, all operators listed in this study were used in low-lying charmonium study in Chap. 4. A_1^{-+} and T_1^{--} channels are used for getting 1S average mass, $M(\overline{1S}) = (M(A_1^{-+}) + 3M(T_1^{--}))/4$.

A_1^{-+}	T_1^{--}	T_1^{++}
$\gamma_5 \cdot S_{p,g}(x)$	$\gamma_i \cdot S_{p,g}(x)$	$\gamma_5\gamma_i \cdot S_{p,g}(x)$
$\gamma_4\gamma_5 \cdot S_{p,g}(x)$	$\gamma_4\gamma_i \cdot S_{p,g}(x)$	$\epsilon_{ijk}\gamma_j\nabla_k$
$\gamma_4\gamma_5\gamma_i\nabla_i$	∇_i	$\epsilon_{ijk}\gamma_4\gamma_j\nabla_k$
$\Delta\gamma_5\Delta$	$\epsilon_{ijk}\gamma_5\gamma_j\nabla_k$	$\lvert\epsilon_{ijk}\rvert\,\gamma_5\gamma_j\mathcal{D}_k$
$\Delta\gamma_4\gamma_5\Delta$	$\lvert\epsilon_{ijk}\rvert\,\gamma_j\mathcal{D}_k$	$\Delta\gamma_5\gamma_i\Delta$
$\nabla_i\gamma_5\nabla_i$	$\lvert\epsilon_{ijk}\rvert\,\gamma_4\gamma_j\mathcal{D}_k$	$\nabla_k\gamma_5\gamma_i\nabla_k$
$\nabla_i\gamma_4\gamma_5\nabla_i$	$\Delta\gamma_i\Delta$	
	$\Delta\gamma_4\gamma_i\Delta$	
	$\nabla_k\gamma_i\nabla_k$	
	$\nabla_k\gamma_4\gamma_i\nabla_k$	

four-point correlator functions, where the full subset means all lattice sites at the specific time slice.

To see how it works, we start from meson correlator,

$$C_{\mathrm{AB}}(x,y) = \operatorname*{Tr}_{cs}\left[\Gamma_A W(x,y)\Gamma_B N(y,x)\right] , \tag{6.3}$$

where $W(x,y)$ is the Wilson-clover propagator, and $N(y,x)$ is the naive propagator introduced in Eq. (5.2). We insert $1 = \Gamma^\dagger(y)\Gamma(y)$ into Eq. (6.3), where $\Gamma(y)$ is introduced as $\Omega(x)$ in Eq. (3.65),

$$\Gamma(y) = \gamma_1^{y_1}\gamma_2^{y_2}\gamma_3^{y_3}\gamma_4^{y_4} \tag{6.4}$$

and use the identity,

$$\delta_{\epsilon'\epsilon}\delta_{\mu'\mu} = \frac{1}{4}\sum_T (\Gamma_T)_{\epsilon'\mu}\left(\Gamma_T^\dagger\right)_{\epsilon\mu'} . \tag{6.5}$$

Then, the staggered-Wilson propagator C_{AB} becomes

$$C_{\mathrm{AB}}(x,y) = \frac{1}{4}\sum_T \operatorname*{Tr}_{cs}\left[\Gamma_A\left(\Gamma(x)\Gamma(y)^\dagger W(x,y)\right)\Gamma_T^\dagger S(y,x)\right]\operatorname*{Tr}_{s}\left[\Gamma(y)\Gamma_B\Gamma^\dagger(y)\Gamma_T\right] . \tag{6.6}$$

Note that with full-subset random sources, the staggered-to-naive conversion factor $\Gamma(x)\Gamma(y)^\dagger$ applies to the Wilson propagator, while the spin-taste operator, $\mathrm{Tr}_s\left[\Gamma(y)\Gamma_B\Gamma^\dagger(y)\Gamma_T\right]$ appears on the source position denoted as y. We get a nonzero value only for $\Gamma_T = \Gamma_B$. To avoid unwanted taste-mixing, we require that accompanying smearing occurs with even displacements. This method also allows us to construct staggered-Wilson correlators for three-point and four-point correlators.

With this prescription, we construct the heavy-light meson correlator in which staggered (light) and Wilson (heavy) fermions are involved in both source and sink positions. Its multiexponential expansion is the same as in Eq. (5.1) up to a normalization factor.

In Sec. 6.6, we perform Lüscher's finite volume analysis; thus, we need to determine the kinetic masses M_2 of D and D^* to extract their interacting momentum from the $D\bar{D}^*$ scattering states. One can achieve this by calculating the heavy-light two-point functions having various momentum.

To extract the interacting momentum $\boldsymbol{p}$ (or $\boldsymbol{q}$) in Eq. (3.160), we first need to calculate the kinetic masses of charmed mesons from the heavy quark dispersion relation. This can be done by employing the general form of the lattice dispersion relation from [126]

$$E(p) = M_1 + \frac{\boldsymbol{p}^2}{2M_2} - \frac{a^3 w_4}{6}\sum_i p_i^4 - \frac{(\boldsymbol{p}^2)^2}{8M_4^3} + \cdots , \tag{6.7}$$

where $\boldsymbol{p} = 2\pi \boldsymbol{n}/L$ for a given spatial extent L. As seen in Fig. 6.5, the momentum square quadratic terms, $(\boldsymbol{p}^2)^2$ and p_i^4, do not affect the fit very much. The curvature of the fitting line is almost negligible. Among them, the rotational breaking terms, with coefficient w_4, can be ignored without loss of the signal quality [70]. Therefore, we determine M_2 by neglecting the rotational-symmetry-breaking terms and fitting M_1, M_2, and M_4 only. We implement six different momenta as independent variables, $\boldsymbol{n} = (0,0,0)$, $(0,0,1)$, $(1,1,0)$, $(1,1,1)$, $(0,0,2)$, and $(2,1,0)$.

The plots for the fits are shown in Fig. 6.5, and the quantitative fit results are displayed in Table 6.3. Here, note that on ensemble (B), the kinetic masses are lighter than their experimental values because we have used a different tuning method for the charm-quark hopping parameter. We discuss the implications later.

6.4.2 Three-point correlation function

The quark-line diagrams contributing to $DD^* \to c\bar{c}$ and $c\bar{c} \to DD^*$ are shown in the off-diagonal panels of Fig. 6.4. We start from a fifteen-dimensional operator basis containing seven $c\bar{c}$ interpolators listed in Table 6.2 with $J^{\mathrm{PC}} = T_1^{++}$ and eight $D\bar{D}^*$ scattering state interpolators differing by their smearing levels and momentum. For the $D\bar{D}^*$ interpolators, the smearings are done only for clover quarks; hence, the implementation is quite the same as for charmonium. To construct the generic $D\bar{D}^*$ scattering-state interpolator satisfying $J^{\mathrm{PC}} = T_1^{++}$, we need to arrange D and D^* interpolators appropriately. For zero relative momentum of $D\bar{D}^*$ interpolators, we can write it as

$$(DD^*)(\mathbf{0},t) = \frac{i}{2}\left[D^*(t,-\mathbf{0})\bar{D}(t,\mathbf{0}) - \bar{D}^*(t,-\mathbf{0})D(t,\mathbf{0})\right] + \frac{i}{2}\left[u \longleftrightarrow d\right] . \tag{6.8}$$

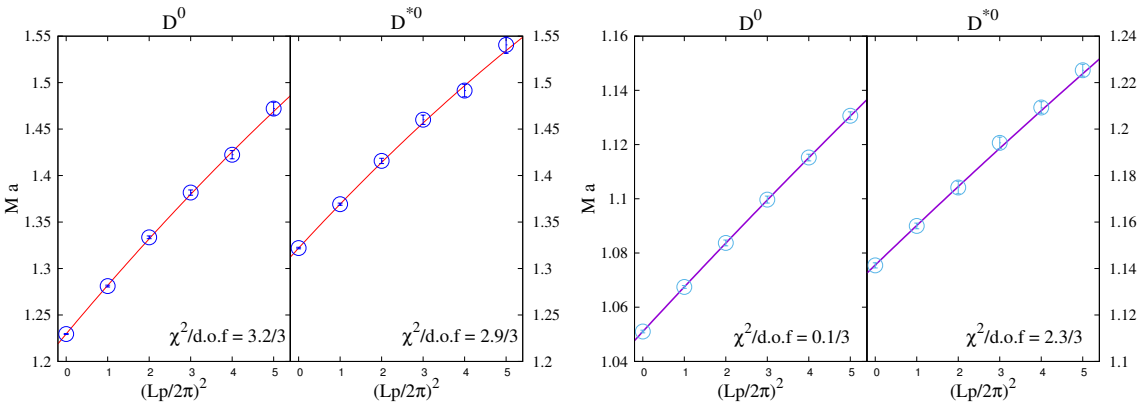

Figure 6.5. Measured energies of D and D^* as a function of $n^2 = (Lp/2\pi)^2$ and a fit using the dispersion relation Eq. (6.7) without the symmetry-breaking-terms involving w_4. The left panel shows the results for ensemble (A) and right one for ensemble (B).

Table 6.3. Measured masses of D and D^* from fits on ensembles (A) and (B). Experimental values represent 1S average.

		M_1	M_2	M_4	M_2[GeV]	Exp[GeV] [5]
ensemble (A)	D	1.2296(5)	1.445(21)	1.39(13)	1.853(27)	1.868
	D^*	1.3220(8)	1.591(31)	1.36(16)	2.040(40)	2.009
ensemble (B)	D	1.0510(5)	1.162(11)	1.10(14)	1520(15)	”
	D^*	1.1556(9)	1.310(28)	1.16(28)	1713(37)	”

where $i/2$ is a normalization factor. The imaginary phase i keeps the correlation matrix $C(t)$ hermitian. Each D and D^* interpolator involves both staggered and clover fermions described by Eq. (5.18). Due to our assumed degeneracy of the u and d light quark masses, the effect of the $[u \longleftrightarrow d]$ part just results in the prefactor 2 as noted in Fig. 6.4.

To assign a nonzero relative momentum of $D\bar{D}^*$ interpolators, we use a light quark source with Fourier factor $e^{-i\mathbf{0}\cdot\boldsymbol{x}} = 1$, and a charm quark source with factors $e^{-2\pi i\mathbf{1}\cdot\boldsymbol{x}/L}$ and $e^{2\pi i\mathbf{1}\cdot\boldsymbol{x}/L}$ for D and D^* creation operators, respectively (and vice versa),

$$\begin{aligned}(DD^*)(\mathbf{1},t) \;=\; & \frac{i}{2\sqrt{2}}\big[D^*(t,-\mathbf{1})\bar{D}(t,\mathbf{1}) - \bar{D}^*(t,-\mathbf{1})D(t,\mathbf{1}) \\ & + D^*(t,\mathbf{1})\bar{D}(t,-\mathbf{1}) - \bar{D}^*(t,\mathbf{1})D(t,-\mathbf{1})\big] + \frac{i}{2\sqrt{2}}\,[u \longleftrightarrow d]\;. \qquad (6.9)\end{aligned}$$

where $\mathbf{0} = (0,0,0)$ and $\mathbf{1} = (0,0,1)$. As with $(DD^*)(\mathbf{0},t)$, the $[u \longleftrightarrow d]$ part results in the prefactor 2. The quark-line diagrams for the three-point functions are shown in Fig. 6.6 for only $D\bar{D}^* \to c\bar{c}$ correlators. We have confirmed that the imaginary part of $DD^* \to c\bar{c}$ correlator values agrees with $c\bar{c} \to DD^*$ within statistics. This is what we

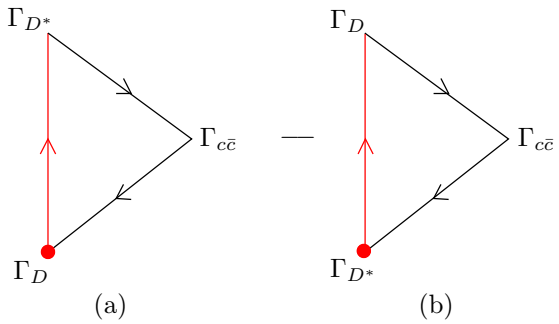

Figure 6.6. Schematic diagrams of the three-point correlation function representing the mixing of $D\bar{D}^*$ and $c\bar{c}$ interpolators.

expected from time-reversal symmetry, and need to confirm it to ensure the hermiticity of the correlation matrix. However, the statistical uncertainty of the latter is large for large t and the calculation is more expensive. Hence, in this study, we use $c\bar{c} \to DD^*$ in place of $DD^* \to c\bar{c}$ to reduce the uncertainties and save the cost. The vertices refer to the D, D^* or charmonium state with the momentum specified in the diagrams. The red-filled circle represents the lattice points where stochastic sources are used. The time runs to the right in the diagrams. The off-diagonal three-point correlation function, $C^{(a)}_{D\bar{D}^*\to c\bar{c}}(t)$ labeled as (a) in Fig. 6.6, can be written as

$$C^{(a)}_{D\bar{D}^*\to c\bar{c}}(t-t_s) = -\frac{1}{N_R}\sum_{j}^{N_R}\sum_{\boldsymbol{w}_1\boldsymbol{w}_2\boldsymbol{x}\boldsymbol{y}} \mathrm{Tr}\langle \xi_j^*(\boldsymbol{w}_2)e^{i\boldsymbol{p}\cdot\boldsymbol{w}_2}W(t_s,\boldsymbol{w}_2;t,\boldsymbol{y})\Gamma_{c\bar{c}}W(t,\boldsymbol{y};t_s,\boldsymbol{x})e^{-i\boldsymbol{p}\cdot\boldsymbol{x}} \times\Gamma_{D^*}N(t_s,\boldsymbol{x};t_s,\boldsymbol{w}_1)\Gamma_D\xi_j(\boldsymbol{w}_1)\rangle \tag{6.10}$$

where, again, W is the Wilson-clover charm-quark propagator, and N is the naive light-quark propagator. The expression of the correlator, $C^{(b)}_{D\bar{D}^*\to c\bar{c}}(t)$, labeled as (b) in Fig. 6.6, can be obtained by interchanging Γ_D and Γ^*_D. We calculate all possible diagrams from the Wick contractions for the zero-relative-momentum as well as nonzero-momentum correlators.

Before presenting the four-point correlation functions, I discuss briefly the physical significance of the off-diagonal three-point correlation functions. Notice that when sea quarks are included as they are in our calculation, physical eigenstates, such as the χ_{c1} and χ_{c2}, contain light sea quark-antiquark pairs as well as charm valence quarks. This means states generated from the interpolator, $c\gamma_5\gamma_i\bar{c}$, develop intrinsic $c\gamma_5\bar{q}\bar{c}\gamma_i q$ contributions (implicit mixing [127,128]). These processes happen through quark-antiquark pair creation and annihilation. We know such processes are weak [127]. This means that we can treat

this as a perturbation. We can decompose the physical Hamiltonian $H = H_0 + \lambda H_1 + \cdots$, into a part H_0 with $c\bar{c}$ and $D\bar{D}^*$ eigenstates, without pair creation. The small perturbation λH_1 is then responsible for the mixing, which appears in the off-diagonal elements. To first order in λ, the $X(3872)$ state vector would be

$$|X(3872)\rangle = |c\bar{c}\rangle + \lambda \frac{\langle D\bar{D}^*|H_1|c\bar{c}\rangle}{E^{(0)}_{c\bar{c}} - E^{(0)}_{D\bar{D}^*}} |D\bar{D}^*\rangle \,, \tag{6.11}$$

where the superscript (0) represents unperturbed energies. Assuming that the mixing strength is not sensitive to the light quark masses, we can expect that if $E^{(0)}_{c\bar{c}}$ is nearly degenerate with $E^{(0)}_{D\bar{D}^*}$, then the $D\bar{D}^*$ component of the $X(3872)$ state must be large; otherwise it becomes small. We will see this difference in the spectrum of the full mixing correlation matrix on ensembles (A) and (B) in Sec. 6.5.

6.4.3 Four-point correlation function

The four-point $D\bar{D}^*$ quark line diagrams contributing to $D\bar{D}^* \to D\bar{D}^*$ are shown in bottom-right panel of Fig. 6.4. From the quark-field contractions, the four-point correlation functions can be classified in two parts – the box and the disconnected diagrams, as shown in Fig. 6.7. All vertices represent D or D^*, and at a fixed time slice, we make the total momentum zero.

First let us consider the disconnected diagrams, which are relatively easier to construct than box diagrams. The disconnected diagrams can be constructed by using two different stochastic sources at a fixed time slice t_s, as shown in Fig. 6.7 (a′) - (d′). One of the correlators, *e.g.,* $C^{(a')}_{D\bar{D}^*\to D\bar{D}^*}(t-t_s)$ can be written as

$$\begin{aligned} C^{(a')}_{D\bar{D}^*\to D\bar{D}^*}(t-t_s) \;=\; & \sum_{j\neq k}^{N_R} \sum_{\boldsymbol{z}\boldsymbol{w}_1\boldsymbol{w}_2} \mathrm{Tr}\langle W(t,\boldsymbol{z};t_s,\boldsymbol{w}_1) e^{i\boldsymbol{p}\cdot\boldsymbol{w}_1} \xi_j(\boldsymbol{w}_1) \Gamma_{D^*} \xi^*_j(\boldsymbol{w}_2) N(t_s,\boldsymbol{w}_2;t,\boldsymbol{z}) \\ & \times e^{-i\boldsymbol{p}'\cdot\boldsymbol{z}} \Gamma_D \rangle \sum_{\boldsymbol{y}\boldsymbol{x}_1\boldsymbol{x}_2} \mathrm{Tr}\langle W(t,\boldsymbol{y};t_s,\boldsymbol{x}_1) e^{-i\boldsymbol{p}\cdot\boldsymbol{x}_1} \xi_k(\boldsymbol{x}_1) \Gamma_{D^*} \xi^*_k(\boldsymbol{x}_2) \\ & \times N(t_s,\boldsymbol{x}_2;t,\boldsymbol{y}) \Gamma_D e^{i\boldsymbol{p}'\cdot\boldsymbol{y}} \rangle \end{aligned} \tag{6.12}$$

where ξ is the stochastic sources generated independently at the source time slices. The spatial lattice sites $\boldsymbol{w}_i$, $\boldsymbol{x}_i$ are located at the sources and $\boldsymbol{y}$, $\boldsymbol{z}$ at the sinks. We first calculate N two-point correlation functions given by Eq. (6.6) with different stochastic sources ξ_j, where $j = 1, 2, ..., N_R$ Then, we multiply the two-point correlator calculated from source ξ_j by the hermitian conjugate of other correlators, calculated from ξ_k for $k \neq j$. If we perform this procedure for all of N two-point correlation functions, then we have in total $N(N-1)/2$ terms. Finally, we add all these terms and divide it by $N(N-1)/2$, For example, if we use

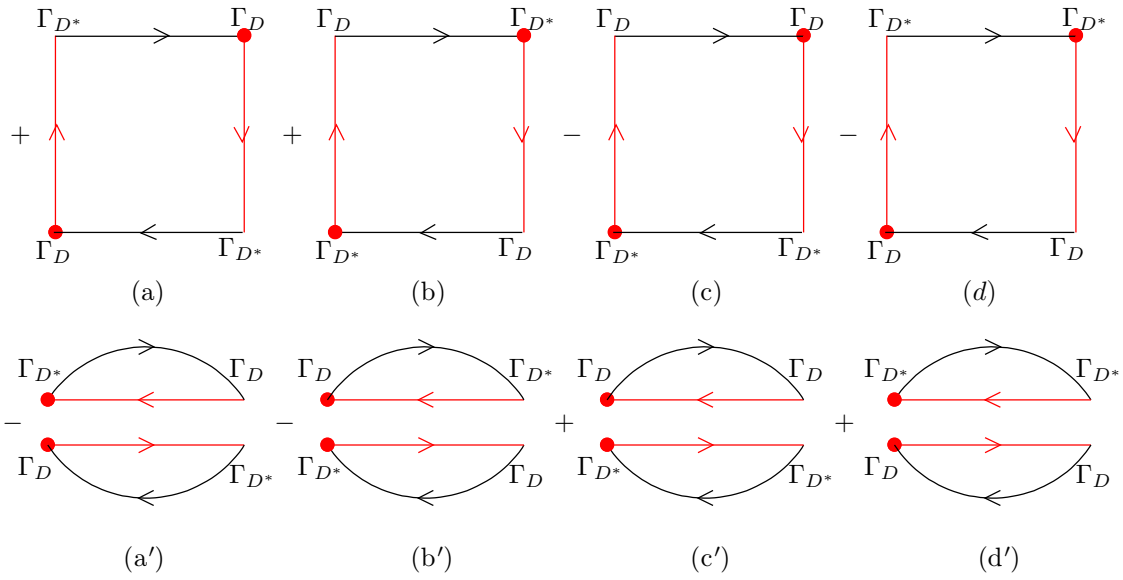

Figure 6.7. Schematic diagrams of four-point correlation function.

three different stochastic sources, ξ_j, where $j = 1, 2, 3$, then the disconnected diagram can be calculated as

$$\frac{1}{3}\left[C_{2pt}(\xi_1)\cdot C_{2pt}(\xi_2)^\dagger + C_{2pt}(\xi_1)\cdot C_{2pt}(\xi_3)^\dagger + C_{2pt}(\xi_2)\cdot C_{2pt}(\xi_3)^\dagger\right] \tag{6.13}$$

where $C_{2pt}(\xi_j)$ means two-point correlation function using stochastic source ξ_j. All other disconnected correlators can be obtained by exchanging Γ_D and Γ_D^*, as displayed in Fig. 6.7 (b′), (c′) and (d′).

Next, consider the box diagrams shown in Fig. 6.7 (a) - (d). Unlike the disconnected diagrams, the box diagrams require another quark propagator connecting the same time slice at the source and sink, which makes the evaluation of these diagrams extremely difficult and expensive. To overcome this difficulty, we construct the correlators with a different approach. Figure 6.8 shows how we construct a box diagram. First, we generate one stochastic source on the source, $\xi(\boldsymbol{w}_1)$, and the other, on the sink, $\eta(\boldsymbol{y}_1)$, which are represented as magenta-filled and blue-filled circles in Fig. 6.8, respectively. From these stochastic sources, we calculate two light-quark propagators – so one at the source time slice (t_s) with stochastic sources $\xi(\boldsymbol{w}_1)$, labeled as (1) in Fig. 6.8, and the other at the sink time slice (t) with $\eta(\boldsymbol{y}_1)$, labeled as (1′) in Fig. 6.8, respectively. Then, we extract two quark-source fields from each propagator at the same respective time slices, $E(\boldsymbol{x})$ at t_s and $E(\boldsymbol{z})$ at t, to make the light quark-antiquark annihilation / creation diagrams. From the extracted Dirac quark fields, $E(\boldsymbol{x})$ and $E(\boldsymbol{z})$, we calculate the clover charm-quark

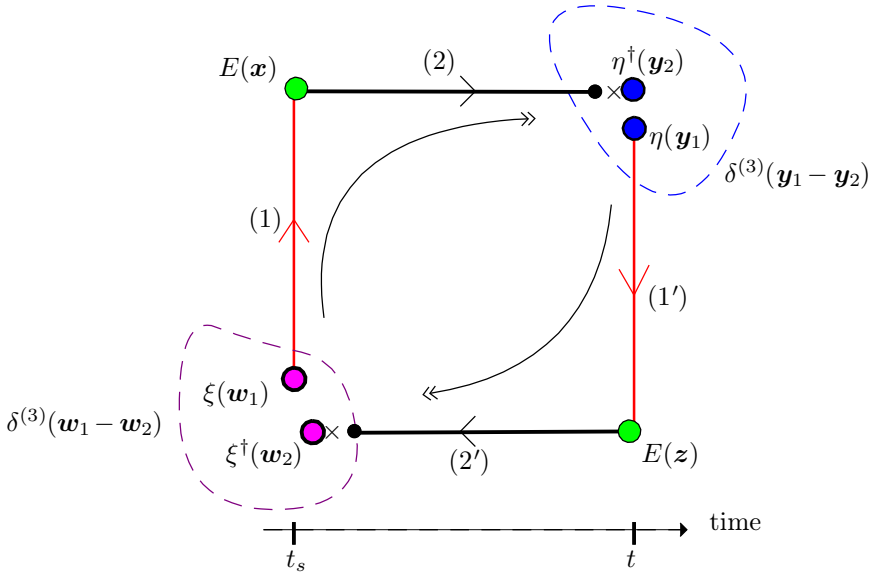

Figure 6.8. Schematic diagrams for the box-diagram construction. Red-thick vertical lines, labeled as (1) and (1′), represent naive propagators, and black-thick horizontal lines, labeled as (2) and (2′), clover propagators. The magenta-filled and blue-filled circles are represent the stochastic sources on the source and the sink, respectively. And the green-filled circles represent the extended sources, $E(\boldsymbol{x})$ and $E(\boldsymbol{z})$. $E(x)$ is generated from the naive propagator, (1), and $E(z)$, from the naive propagator, (2), respectively.

propagators, labeled as (2) and (2′), for all time slices. Now, for the charm propagators starting from time slice t_s and stochastic source ξ, we multiply by $\eta^\dagger(\boldsymbol{y}_2)$ at t. On the other hand, for the propagators starting from time slice t and stochastic source η, we multiply by $\xi^\dagger(\boldsymbol{w}_2)$ at t_s. Then, we sum each propagator over all the lattice spatial sites separately. This operation results in the propagators having a $4\times4\otimes N_R\times3$ tensor structure, where 4 is the Dirac-spinor dimension, N_R is the number of stochastic sources, and 3 is the number of colors. Because both stochastic sources, ξ and η, satisfy Eq. (3.101), if we perform a tensor product of these two propagators and average over stochastic sources, then we get the box diagram correlator $C(t_s,t)$. The resultant correlator can be expressed as

$$\begin{aligned} C^{(a)}_{D\bar{D}^*\to D\bar{D}^*}(t-t_s) \;=\; & -\frac{1}{N_R^2}\,\mathrm{Tr}\Big\langle \sum_{jk}^{N_R}\sum_{\boldsymbol{w}_2\boldsymbol{y}_1\boldsymbol{z}} \xi^\dagger_j(\boldsymbol{w}_2)e^{i\boldsymbol{p}\cdot\boldsymbol{w}_2}W(t_s,\boldsymbol{w}_2;t,\boldsymbol{z})e^{-i\boldsymbol{p}'\cdot\boldsymbol{z}}\Gamma_{D^*}N(t,\boldsymbol{z};t,\boldsymbol{y}_1) \\ & \times\eta_k(\boldsymbol{y}_1)\Gamma_D\sum_{\boldsymbol{w}_1\boldsymbol{x}\boldsymbol{y}_2}\eta^\dagger_k(\boldsymbol{y}_2)e^{i\boldsymbol{p}'\cdot\boldsymbol{y}_2}W(t,\boldsymbol{y}_2;t_s,\boldsymbol{x})e^{-i\boldsymbol{p}\cdot\boldsymbol{x}}\Gamma_{D^*}N(t_s,\boldsymbol{x};t_s,\boldsymbol{w}_1) \\ & \times\xi_j(\boldsymbol{w}_1)\Gamma_D\Big\rangle\,, \end{aligned} \tag{6.14}$$

where the spatial lattice sites $\boldsymbol{w}_1,\boldsymbol{w}_2,\boldsymbol{x}$ reside on the source time slice and $\boldsymbol{y}_1,\boldsymbol{y}_2,\boldsymbol{z}$ on the sink time slice. As with the disconnected diagrams, we can obtain all other box diagrams

by exchanging Γ_D and Γ_{D^*} as displayed in Fig. 6.7 (b),(c) and (d). Note that spin-color trace $\mathrm{Tr}\langle\cdots\rangle$ is the last step of the calculation.

We can extend this single-time-slice box diagram correlator to multiple time slices by using lattice time-translation symmetry. For example, consider time slices $(0, 1, 2)$ for the sources and $(4, 7, 11)$ for the sink. By using time-translation symmetry on the lattice, we can perform the same operation as above for all listed times slices. When we take all pairs of the source and sink times, we construct the box diagram correlator for all time separations from $2 = 4 - 2$ to $11 = 11 - 0$. Because we always calculate the correlators by using several different time sources per gauge configuration, we can further reduce the number of inversions and get correlators at more time slices.

The correlator $C_{D\bar{D}^*\to D\bar{D}^*}(t)$ plays a important role in the analysis. In the case of the disconnected diagram, the two charmed heavy-light meson correlators are disconnected, and we can expect that the leading interactions are mostly exchanging gluons or η' mesons from the valence light-quark lines (see the left column in Fig. 6.9). These are short-range interactions. Thus, we expect that they must be small. On the other hand, the box diagram contains valence light-quark annihilation / creation process. Thus, it can contain one-pion exchange (long-range) and multiple-pion exchange (short-range) interactions as well as all other possible interactions. (See the right column in Fig. 6.9.) Thus, we see that the box diagrams are actually the charmonium correlators with explicit mixing with $D\bar{D}^*$.

6.5 Spectrum

In the previous sections, we have discussed how to construct the mixing correlation matrix shown in Fig. 6.4. We analyze this mixing correlation matrix by dividing it into four parts - $c\bar{c}$ only (the upper-left submatrix), $c\bar{c} + D\bar{D}^*_{I=0}$ (the whole matrix), $D\bar{D}^*_{I=0}$ (the lower-right submatrix) and $D\bar{D}^*_{I=1}$ (the lower-right submatrix without the box diagram). For each submatrix, we construct the corresponding generalized eigenvalue problem and get the corresponding eigenvalues. In this section, I provide the resulting spectrum and the interpretation.

Figures 6.10 and 6.11 show the resulting energy levels extracted from the eigenvalues for the ensembles (A) and (B), respectively. In the figures, the red and blue lines represents the energy splittings between E_n and $M(\overline{1S}) = \frac{1}{4}[M(\eta_c) + 3M(J/\psi)]$, the spin-averaged ground state charmonium mass, where the E_ns are the energy levels from the variational analysis. The thickness of the lines represent the statistical errors estimated from a single-elimination jack-knife. To get $\overline{1S}$, we use the A_1^{-+} and T_1^{--} interpolating operators listed in Table 6.2 and use the standard variational method. The green lines in Figs. 6.10 and 6.11 indicate

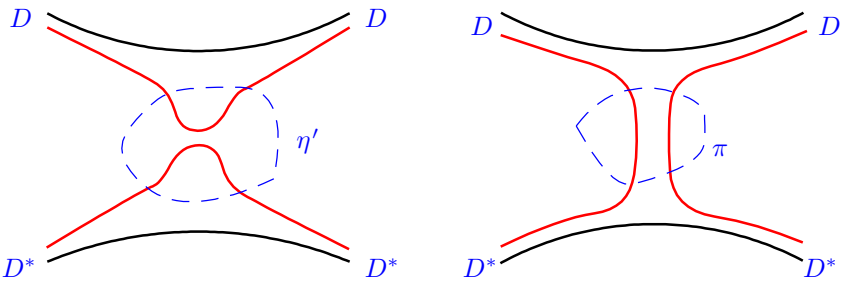

Disconnected diagram Box diagram

Figure 6.9. Schematic diagrams of the leading meson-exchange interaction for the disconnected diagram (left) and the box diagram (right).

the $D\bar{D}^*$ noninteracting energies – the lower line with relative momentum $\boldsymbol{p} = 0$, and the upper line, $\boldsymbol{p} = 1$. For all channels, we use the reference time $t_0 = 2$. The fitting details are shown in Tables 6.4 and 6.5 for ensembles (A) and (B), respectively.

For the $c\bar{c}$-only subset (T_1^{++}), the correlation matrix dimension is 7×7 which coincides with the number of pure $c\bar{c}$ interpolators listed in Table 6.2. Because this channel does not include any of the staggered fermion interpolators, the correlation matrix $C_{c\bar{c}\to c\bar{c}}(t)$ includes no oscillating states, so we use the standard variational method expressed in Eq. (3.117), and fit the eigenvalue data to the form given by Eq. (3.118).

For all the other channels, $c\bar{c} + D\bar{D}^*_{I=0}$, $D\bar{D}^*_{I=0}$, and $D\bar{D}^*_{I=1}$, the correlation matrices involve oscillating states, because we use HISQ light quarks to construct the D and D^* mesons. Thus, we implement the staggered variational method described in Chap. 5, and the generalized eigenvalue equation is given in Eq. (5.9), where the fitting formula is given in Eq. (5.16).

First, we discuss the ensemble (A) spectrum (Fig. 6.10). In the $D\bar{D}^*_{I=1}$ channel (fourth column), both levels are slightly pushed up from their noninteracting levels. This indicates that in this channel, the interaction is weak, and both states are repulsive scattering states. We find no extra states in addition to the scattering states in this channel – thus no candidate state for an isotriplet $X(3872)$. For the $c\bar{c}$-only subset (first column), our choice of quark masses resulted in an accidental degeneracy between the first excited state and the $D\bar{D}^*$ threshold. The ground state is simply the conventional $\chi_{c1}(1P)$, and the first excited state may be the conventional $\chi_{c1}(2P)$ state that implicitly mixes with the $D\bar{D}^*$ components. For the $D\bar{D}^*_{I=0}$ subset (third column), the first excited state energy level sits at the $D\bar{D}^*$ threshold within its uncertainty, and thus we find no $X(3872)$ candidate state, either. Note

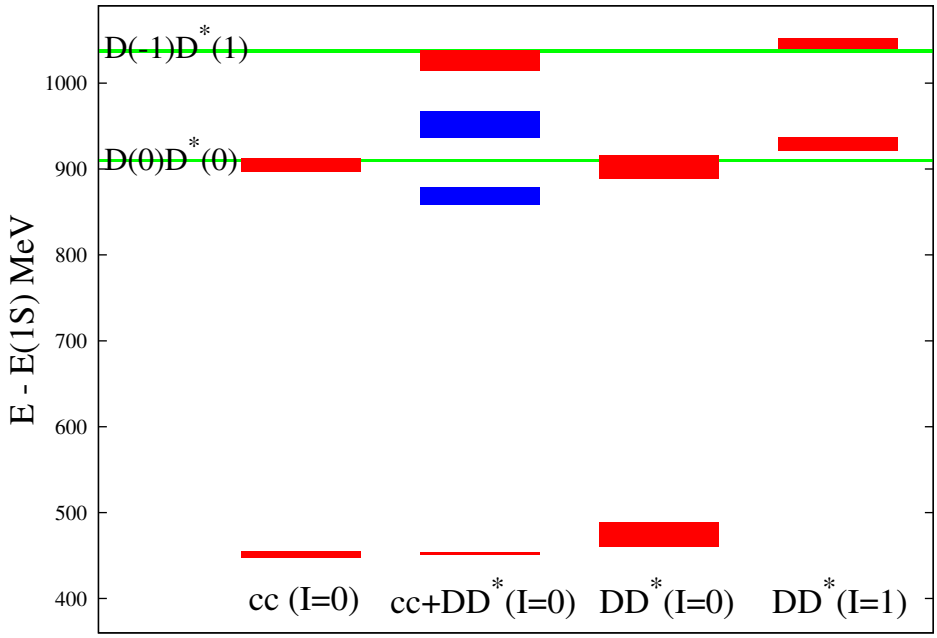

Figure 6.10. Spectrum results for the simulation on ensemble (A) listed in Table 6.1. Each bar represents energy splitting between E_n and $\overline{1S} = \frac{1}{4}(M_{\eta_c} + 3M_{J/\psi})$, the spin-averaged $1S$ charmonium masses. The thickness of the lines represent statistical uncertainty. The lower and upper green lines indicate $D\bar{D}^*(\mathbf{0})$ and $D\bar{D}^*(\mathbf{1})$ threshold energies, respectively. Left panel: the unmixed $\chi_{c1}(1P)$ and $\chi_{c1}(2P)$ states. Middle panel: mixed $c\bar{c}$ and $D\bar{D}^*$ states resulting in a possible $X(3872)$ and $D\bar{D}^*$ scattering states. Right panel: the unmixed $D\bar{D}^*$ states with isospin 0. The lower blue bar represents the $X(3872)$ candidate.

that the $\chi_{c1}(1P)$ state appears without the assistance of explicit $c\bar{c}$ interpolators, because the box diagram contains $c\bar{c}$ explicitly. For the $c\bar{c} + D\bar{D}^*_{I=0}$ channel (second column), while the ground state remains the same, compared with only $c\bar{c}$ channel, the first and second excited states, represented as two blue bars, are shifted from the threshold by about 40 MeV.

By contrast, the spectrum for the ensemble (B), shown in Fig. 6.11, develops no significant energy shifts. For the $D\bar{D}^*_{I=0}$ (third column) and $D\bar{D}^*_{I=1}$ (fourth column) subsets, the energy level trends are not much different from the ensemble (A) cases. Note that, in the $c\bar{c}$-only subset, the first excited state is much above the $D\bar{D}^*$ threshold. Thus, we expect that $c\bar{c} + D\bar{D}^*$ mixing effect must be much smaller than in the ensemble (A) case (refer to Eq. (6.11)). That is the energy shifts must be tiny when all explicit mixings are turned on. Indeed, all energy shifts in the second panel are small, compared with those in ensemble (A).

Note that we perform a simulation on $n_F = 2 + 1 + 1$ HISQ ensembles. As we have

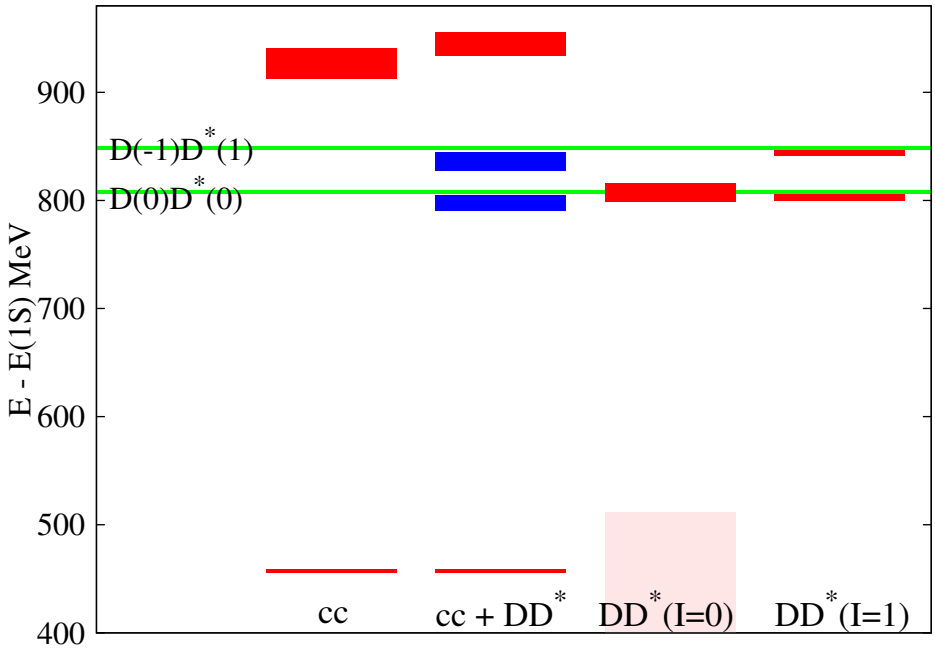

Figure 6.11. Spectrum results for the simulation on ensemble (B) listed in Table 6.1. Refer to the caption of Fig. 6.10 for notations. Unlike the lower blue bar on ensemble (A), it is ambiguous to interpret the first excited state in the second panel as $X(3872)$ candidate. See the text for detailed discussion.

remarked, when the sea quarks are included, physical eigenstates, generated from the $c\bar{c}$ interpolator, contain light quark-antiquark contributions as well as charm valence quarks. Likewise, in the $D\bar{D}^*_{I=0}$ sector, obviously it contains $c\bar{c}$ contributions. Therefore, the spectrum should be same for all $I = 0$ sectors, $c\bar{c}$, $c\bar{c} + D\bar{D}^*(I = 0)$, and $D\bar{D}^*_{I=0}$. However, as seen in Figs. 6.10 and 6.11, the spectra look different. The correct way to look at this is that there is only one spectrum for $I = 0$. The reason that columns 1, 2, and 3 look different is that we cannot see the energy splitting, with a too-small basis of interpolators, namely the $c\bar{c}$-only subset or the $D\bar{D}^*_{I=0}$-only subset. The figure is misleading! Instead, we see just an average of two physical eigenstates, where the weighting of the average may favor one or the other, because the interpolators involved have very poor overlap with one or the other eigenstate. However, when the full set of operators is used, the splitting is revealed.

Then, a question arises: what is the physical nature of these two states? Can we interpret one of the states represented by the blue bars as a weakly bound state of $D\bar{D}^*$? To answer this question, we need to perform a further analysis by using the finite volume method introduced in Sec. 3.6 to extract the scattering parameters, such as the scattering length

Table 6.4. Ensemble (A) fit results for the eigenvalues over the various mixing channels for the correlation matrix shown in Fig. 6.4. The $D\bar{D}^*$ threshold with the relative momentum $\boldsymbol{p} = \mathbf{0}$ is $aM_D + aM_{D^*} = 2.5514(10)$ and with $\boldsymbol{p} = \mathbf{1}$ is $aE_D(\mathbf{1}) + aE_{D^*}(-\mathbf{1}) = 2.6503(16)$ represented by the green lines in in Fig. 6.10. The corresponding spectrum results are shown in Fig. 6.10. The reference time is $t_0 = 2$ throughout all channels.

channel	level	aE	fit range	$\chi^2/d.o.f$
$c\bar{c}$ only	e_0	2.1937(28)	3-20	8.8/14
	e_1	2.5467(63)	3-9	3.7/3
$c\bar{c} + D\bar{D}^*$	e_0	2.1943(11)	3-20	8.7/12
	e_1	2.5186(78)	3-13	3.2/3
	e_2	2.5841(116)	4-11	3.8/2
	e_3	2.6401(112)	3-11	1.8/3
$D\bar{D}^*(I = 0)$	e_0	2.2121(99)	4-20	14.3/9
	e_1	2.5453(124)	3-15	8.0/5
$D\bar{D}^*(I = 1)$	e_0	2.5657(58)	3-16	2.9/4
	e_1	2.6576(81)	4-17	1.6/4

and effective range. We discuss this analysis in the next section.

6.6 Effective range and scattering length

To interpret the spectrum results involving multiple particles in a finite volume, it is essential to extract scattering parameters with the finite-volume method. As mentioned in the beginning of this chapter, the spectrum in a finite volume is discrete, whether the state is bound or part of the continuum. Therefore, we need further analysis to enable us to interpret the resulting spectrum.

Let us start from the definition of the S-wave scattering length introduced in Sec. 3.6,

$$a_0 = \lim_{p \to 0} \frac{\tan \delta(p)}{p} \,. \tag{6.15}$$

If there is a bound state, the scattering amplitude, given by Eq. (3.133), has a pole at $p = i\kappa$, where $\kappa > 0$. Therefore, at close to $p = 0$, one can rewrite the scattering amplitude as

$$f = \frac{1}{\frac{1}{a_0} + \kappa} \,. \tag{6.16}$$

Thus, for small p, to get a bound-state pole, the scattering length a_0 should be negative. To go further, in the case of $p \ll 1/R$, where R is an interaction range, one can expand

Table 6.5. Ensemble (B) fit results for the eigenvalues over the various mixing channels for the correlation matrix shown in Fig. 6.4. The $D\bar{D}^*$ threshold with the relative momentum $\boldsymbol{p} = \boldsymbol{0}$ is $aM_D + aM_{D^*} = 2.2060(12)$ and with $\boldsymbol{p} = \boldsymbol{1}$ is $aE_D(\boldsymbol{1}) + aE_{D^*}(-\boldsymbol{1}) = 2.2375(12)$ represented by the green lines in in Fig. 6.11. The corresponding spectrum results are shown in Fig. 6.11. The reference time is $t_0 = 2$ throughout all channels.

channel	level	aE	fit range	$\chi^2/d.o.f$
$c\bar{c}$ only	e_0	1.9384(10)	3-19	18.9/13
	e_1	2.2972(115)	3-8	2.7/2
$c\bar{c} + D\bar{D}^*$	e_0	1.9390(6)	3-20	19.7/12
	e_1	2.2006(35)	4-16	4.6/5
	e_2	2.2301(59)	4-13	2.4/2
	e_3	2.3110(68)	4-12	5.8/3
$D\bar{D}^*(I = 0)$	e_0	1.9174(520)	6-19	8.2/8
	e_1	2.2056(76)	3-12	2.3/2
$D\bar{D}^*(I = 1)$	e_0	2.2075(11)	3-19	13.4/9
	e_1	2.2342(17)	3-17	5.7/7

$p \cot \delta_0(p)$ in p^2,

$$p \cot \delta_0(p) = \frac{1}{a_0} + \frac{1}{2} r_0 p^2 + O(p^4) \,. \tag{6.17}$$

This is called effective range approximation. The parameter r_0 is the effective range, which must be positive [129]. Then, the quadratic equation to get a bound-state pole is

$$\kappa^2 - \frac{2}{r_0}\kappa - \frac{2}{r_0 a_0} = 0 \,, \tag{6.18}$$

and the solutions are given by

$$\kappa = \frac{1}{r_0}\left(1 \pm \sqrt{1 + \frac{2r_0}{a_0}}\right) \,, \tag{6.19}$$

where we may exclude the case "+", because it could not fit our assumption that $p \ll 1/R$. Then, we can classify three cases as follows:

- case 1. $a_0 < -2r_0$, in which $\kappa > 0$, and we get a weakly bound-state,
- case 2. $-2r_0 < a_0 < 0$, in which we get a resonant state, because κ becomes complex and the momentum is given by $p = (i + \alpha)/r_0$, where α is real,
- case 3. $a_0 > 0$, in which $\kappa < 0$, and we get a "virtual bound state".

Therefore, according to the scattering length we get from the finite volume method, we will be able to classify the states.

Now, let us look at how the lowest elastic scattering state depends on the scattering length. According to Eq. (3.163),

$$\Delta E_{q^2=0} \approx -\frac{2\pi a_0}{\mu L^3}\left[1 + c_1\frac{a_0}{L} + c_2\left(\frac{a_0}{L}\right)^2 + \mathcal{O}\left(\frac{1}{L^3}\right)\right],$$

where $\Delta E_{q^2=0}$ is the energy difference between the scattering state and the continuum threshold. This formula tells us that if $a_0 < 0$, then $\Delta E_{q^2=0} > 0$, and the lowest scattering state energy is above the threshold. If $a_0 > 0$, the energy level is below the threshold. Therefore, the signature of bound state formation at finite volume depends on the shape of the spectrum and the sign of scattering length. One such bound state scenario is that $a_0 < 0$ and $\Delta E_{q^2=0} < 0$, which indicates that the state is not the lowest elastic scattering state. In contrast, if $a_0 > 0$, one cannot distinguish the scattering and bound states in the finite volume, because even the lowest elastic scattering state could be below the threshold.

As shown in Figs. 6.10 and 6.11, two states near the $D\bar{D}^*$ threshold appear to have shifted in opposite directions relative to the threshold on both ensembles. Then, the remaining task is to extract the scattering lengths. For convenience, we calculate $p\cot\delta_0(p)$, rather than the scattering phase shift itself by using the inverse expression of Eq. (3.160),

$$p\cot\delta(\boldsymbol{p}) = \frac{2\mathcal{Z}_{00}(1;q^2)}{\sqrt{\pi}L} \tag{6.20}$$

where p is the interacting momentum and q is the scaled momentum, $Lp/2\pi$. On both ensembles (A) and (B), we extract the interacting momentum from the two states near the threshold – the first and second excited states shown in the second panels of Figs 6.10 and 6.11. To achieve this, we employ the lattice dispersion relation [126], *i.e.,* Eq. (6.7) for two particles:

$$E(p) = M_{1,D+D^*} + \frac{\boldsymbol{p}^2}{2M_{2,D}} + \frac{\boldsymbol{p}^2}{2M_{2,D^*}} - \frac{(\boldsymbol{p}^2)^2}{8M_{4,D}^3} - \frac{(\boldsymbol{p}^2)^2}{8M_{4,D^*}^3}, \tag{6.21}$$

where the masses M_1, M_2, and M_4 of D and D^* are given in Table 6.3 for both ensembles (A) and (B). Finally, we insert these interacting momenta into Eq. (6.20), and by using the zeta function expression given in Eq. (3.162), we get $p\cot\delta(\boldsymbol{p})$. Table 6.6 lists all the relevant values.

Now, by inserting p and $p\cot\delta_0(p)$ of E_1 and E_2 listed in Table 6.6 into Eq. (6.17), we get the scattering length (a_0), and effective range (r_0) of $D\bar{D}^*$,

$$\text{Ensemble (A):} \qquad a_0 = -1.37 \pm 0.34\text{fm}, \quad r_0 = 0.22 \pm 0.13\text{fm} \tag{6.22}$$

Table 6.6. Energy shifts relative to $D\bar{D}^*$ threshold, interacting momentum, and the corresponding $p\cot\delta(p)$ from Eq. (6.20).

ensemble	level	$E_n - M_{1,D+D^*}$ [GeV]	p^2 [GeV^2]	$p\cdot\cot\delta(p)$ [GeV]
(A)	1	$-0.042(10)$	$-0.082(20)$	$-0.189(32)$
	2	0.042(15)	0.082(30)	$-0.100(76)$
(B)	1	$-0.011(7)$	$-0.017(12)$	$-0.082(45)$
	2	0.028(9)	0.045(15)	0.10(15)

$$\text{Ensemble (B):} \qquad a_0 = -6.36 \pm 7.35\text{fm}, \quad r_0 = 1.19 \pm 0.69\text{fm}\,. \tag{6.23}$$

Note that on ensemble (B), although the central value of the scattering length is plausible for the $X(3872)$, [1] the uncertainty in the scattering length is larger than the central value.

On ensemble (A), we get a negative scattering length, $a_0 < -2r_0$, which fits the bound-state scenario discussed at the beginning of this section (first case listed above). That is, the lower blue bar state in Fig. 6.10 is the $X(3872)$ candidate as a weakly bound state of $D\bar{D}^*$ and the upper blue bar state is the lowest scattering state with positive energy shift.

On ensemble (B), given the uncertainty in a_0, there could be three possible interpretations. If $a_0 < -2r_0$, the weakly bound state scenario can be applied to this ensemble result, too, so that the lower blue bar state is the $X(3872)$ candidate. Then, this would be the more reliable lattice calculation than the results on the ensemble (A), in that the ensemble size is larger, and valence- and sea-light quark masses coincide with the physical light quark masses. By contrast, if $-2r_0 < a_0 < 0$, rather than the bound state, we may able to relate the state to a resonance. The final case is $a_0 > 0$, where, within statistics, the maximum a_0 is 1 fm, which is slightly less than the effective range r_0. In this case, we may able to relate the state to a virtual bound state, or the lowest scattering state according to Eq. (3.163).

Despite this ambiguity on ensemble (B), let us assume that it is a bound state and find the pole mass. According to Eq. (3.133), in the infinite volume limit, the bound state pole can be found at $p\cot\delta_0(p) = ip$. Then, inserting Eqs. (6.22) and (6.23) into Eq. (6.17), we interpolate the pole position to satisfy the condition $p\cot\delta_0(p) = ip$. We find the $D\bar{D}^*$ bound state pole positions at $p^2_{BS} = -0.025 \pm 0.012$ GeV^2 on ensemble (A) and $p^2_{BS} = -0.0012 \pm 0.0029$ GeV^2 on ensemble (B), respectively. Figs. 6.12 and 6.13 show the

[1] One can crudely estimate the scattering length of the $X(3872)$ from experimental data $M_{X(3872)} - (M_{D^{*0}} + M_{D^0}) =\sim 0.26$ MeV, and, using a small binding energy, $E_B = 1/(2\mu a_0^2)$ where μ is the reduced mass of the $D\bar{D}^*$. [130], we get $a_0 \sim 8$ fm.

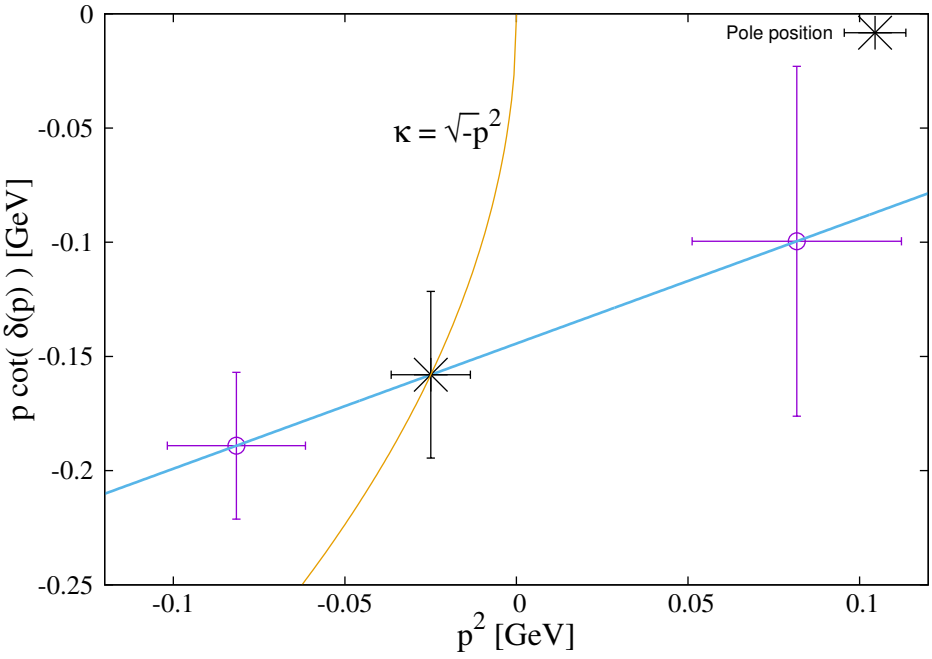

Figure 6.12. The bound state pole position on ensemble (A). The star symbol represents the interpolated pole position satisfying $\cot\delta_0(p) = i$. Two circles with $x - y$ error bars represent the values of $p\cot\delta_0(p)$ over p^2. The curve shows $\kappa = \sqrt{-p^2}$. The two curves intersect at the pole position.

resultant interpolated pole positions in the infinite volume limit. The corresponding bound state energies, E_B, are $E_B = 13 \pm 6$ MeV on ensemble (A) and $E_B = 0.62 \pm 1.53$ MeV on ensemble (B).

6.7 Conclusion and outlook

We conclude that the $X(3872)$ may be a weakly bound state of $D\bar{D}^*$, because the emergence of both pushed-down and -up states from the threshold and the corresponding negative scattering lengths are the indications of weakly bound state on the lattice. This scenario coincides with the previous deuteron simulation [131, 132] and also the $X(3872)$ study of Prelovsek and Leskovec [74] on the lattice. In the $c\bar{c} + D\bar{D}^*(I = 0)$ channel, we estimate the binding energies as 13 ± 6 MeV and 0.62 ± 1.53 MeV below the $D\bar{D}^*$ threshold on ensembles (A) and (B), respectively. In addition, we also get the corresponding scattering lengths -1.37 ± 0.34 fm and -6.36 ± 7.35 fm, respectively.

For the results on ensemble (A), however, our lattice size, ~ 2.4 fm, is much smaller than the expected rms separation of $D\bar{D}^*$ (~ 6 fm) [130]; therefore, significant finite volume effects are expected. In addition, because the light quark masses, $\sim 0.2m_s$, are heavier than

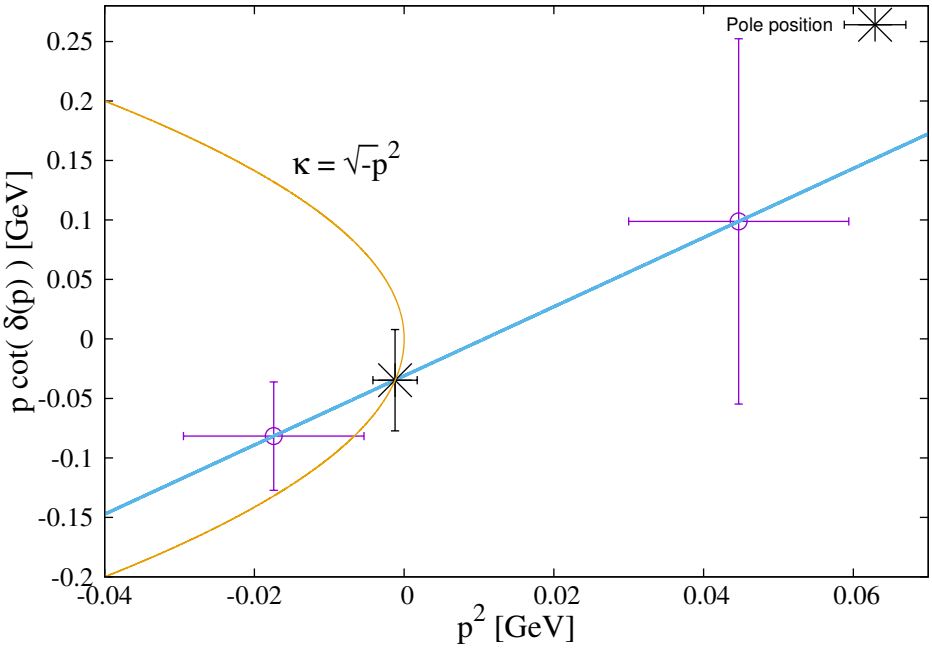

Figure 6.13. The bound state pole position on ensemble (B). See the caption in Fig. 6.12 for an explanation.

physical, we expect only a qualitative result for the binding energy and the scattering length.

On the other hand, for the results on ensemble (B), the lattice size is much larger than ensemble (B), and the light quark masses are all physical. Nevertheless, due to the small splitting of the pushed-down state to the threshold, the uncertainty of both binding energy and scattering length are larger than the central values. Although they are statistically consistent, to draw any conclusions about the $X(3872)$ state, we need to increase the statistics to reduce the statistical errors.

Because in this and previous $X(3872)$ lattice studies [74, 75, 133], all have been done at a single volume, one cannot control finite size effects. To gain better control, one needs simulations on the multiple volumes. Then, if the $X(3872)$ candidate state is true bound state, the pole position will not change; otherwise, the values of splittings will decay exponentially as the volume increase [134].

However, simulations with $D\bar{D}^*$ multiparticle interpolating operators on larger lattice volumes are challenging due to the expensive nature of the box diagram calculation. In fact, it is even almost impossible to get a good signal-to-noise-ratio if the splittings are tiny as they are in ensemble (B).

Instead, we propose another method to achieve this without the box-diagram. Note

that due to the proximity of $X(3872)$ mass to the $D\bar{D}^*$ threshold, we may be able to assume that the mixing parameter, $\langle \chi_{c1}(2P)|H_{int}|D\bar{D}^*\rangle$, must be small enough to use a perturbative approach. Because the interacting Hamiltonian, H_{int}, is completely unknown, the lattice calculation would be the key to reveal this mixing parameter. Note the Eq. (6.11) in Sec. 6.4.2,

$$|X(3872)\rangle = |c\bar{c}\rangle + \lambda \frac{\langle D\bar{D}^*|H_{int}|c\bar{c}\rangle}{E^{(0)}_{c\bar{c}} - E^{(0)}_{D\bar{D}^*}} |D\bar{D}^*\rangle \,.$$

We can extract $E^{(0)}_{c\bar{c}}$ and $E^{(0)}_{DD^*}$ easily from the two-point correlation functions. The three-point correlation functions depends on these two unperturbed energies and the mixing parameter. Therefore, if we calculate the three-point functions, we can finally extract the mixing parameter between $c\bar{c}$ and $D\bar{D}^*$. Without the box diagrams, the cost to perform these simulations is much less than the full analysis. Thus, the next step is to do a calculation to get these mixing parameters on multiple lattices with different sizes.

REFERENCES

[1] Wikipedia, "Standard model," 2006. [Online]. Available: https://en.wikipedia.org/wiki/Standard_Model

[2] E. Follana, Q. Mason, C. Davies, K. Hornbostel, P. Lepage, and H. Trottier, "Further improvements to staggered quarks," *Nucl. Phys. Proc. Suppl.*, vol. 129, pp. 447–449, 2004, [,447(2003)]. [Online]. Available: http://arxiv.org/abs/hep-lat/0311004

[3] R. A. Soltz, C. DeTar, F. Karsch, S. Mukherjee, and P. Vranas, "Lattice QCD thermodynamics with physical quark masses," *Ann. Rev. Nucl. Part. Sci.*, vol. 65, pp. 379–402, 2015. [Online]. Available: http://arxiv.org/abs/1502.02296

[4] E. Follana, Q. Mason, C. Davies, K. Hornbostel, G. P. Lepage, J. Shigemitsu, H. Trottier, and K. Wong, "Highly improved staggered quarks on the lattice, with applications to charm physics," *Phys. Rev.*, vol. D75, p. 054502, 2007. [Online]. Available: http://arxiv.org/abs/hep-lat/0610092

[5] K. A. Olive *et al.*, "Review of particle physics," *Chin. Phys.*, vol. C38, p. 090001, 2014.

[6] T. Barnes, "The XYZs of charmonium at BES," *Int. J. Mod. Phys.*, vol. A21, pp. 5583–5591, 2006. [Online]. Available: http://arxiv.org/abs/hep-ph/0608103

[7] M. B. Oktay and A. S. Kronfeld, "New lattice action for heavy quarks," *Phys. Rev.*, vol. D78, p. 014504, 2008. [Online]. Available: http://arxiv.org/abs/0803.0523

[8] D. Mohler, A. S. Kronfeld, J. N. Simone, C. DeTar, S.-h. Lee, and L. Levkova, "Low lying charmonium states at the physical point," *PoS*, vol. LATTICE2014, p. 085, 2015. [Online]. Available: http://arxiv.org/abs/1412.1057

[9] C. DeTar, A. S. Kronfeld, S.-h. Lee, L. Levkova, D. Mohler, and J. N. Simone, "Splittings of low-lying charmonium masses at the physical point," *Preparing for Submission*, 2016.

[10] L. Levkova and C. DeTar, "Charm annihilation effects on the hyperfine splitting in charmonium," *Phys. Rev.*, vol. D83, p. 074504, 2011. [Online]. Available: http://arxiv.org/abs/1012.1837

[11] C. W. Bernard, T. Burch, K. Orginos, D. Toussaint, T. A. DeGrand, C. E. DeTar, S. A. Gottlieb, U. M. Heller, J. E. Hetrick, and B. Sugar, "The static quark potential in three flavor QCD," *Phys. Rev.*, vol. D62, p. 034503, 2000. [Online]. Available: http://arxiv.org/abs/hep-lat/0002028

[12] A. Bazavov *et al.*, "B- and D-meson decay constants from three-flavor lattice QCD," *Phys. Rev.*, vol. D85, p. 114506, 2012. [Online]. Available: http://arxiv.org/abs/1112.3051

[13] M. Gell-Mann, "A schematic model of baryons and mesons," *Phys. Lett.*, vol. 8, pp. 214–215, 1964.

[14] G. Zweig, "An SU_3 model for strong interaction symmetry and its breaking; Version 2," no. CERN-TH-412, p. 80 p, Feb 1964, version 1 is CERN preprint 8182/TH.401, Jan. 17, 1964. [Online]. Available: https://cds.cern.ch/record/570209

[15] J. F. Donoghue, E. Golowich, and B. R. Holstein, "Dynamics of the standard model," *Camb. Monogr. Part. Phys. Nucl. Phys. Cosmol.*, vol. 2, pp. 1–540, 1992.

[16] S. Coleman, *Aspects of symmetry: selected erice lectures*. Cambridge University Press, 1988. [Online]. Available: https://books.google.com/books?id=PX2Al8LE9FkC

[17] M. E. Peskin and D. V. Schroeder, *An introduction to quantum field theory*, 1995. [Online]. Available: http://www.slac.stanford.edu/spires/find/books/www?cl=QC174.45%3AP4

[18] D. J. Gross and F. Wilczek, "Ultraviolet behavior of nonabelian gauge theories," *Phys. Rev. Lett.*, vol. 30, pp. 1343–1346, 1973.

[19] H. D. Politzer, "Reliable perturbative results for strong interactions?" *Phys. Rev. Lett.*, vol. 30, pp. 1346–1349, 1973.

[20] T. Nakano and K. Nishijima, "Charge independence for V-particles," *Prog. Theor. Phys.*, vol. 10, pp. 581–582, 1953.

[21] K. G. Wilson, "Confinement of quarks," *Phys. Rev.*, vol. D10, pp. 2445–2459, 1974.

[22] R. P. Feynman and A. R. Hibbs, *Quantum mechanics and path integrals*, ser. International series in pure and applied physics. New York, St. Louis, San Francisco: McGraw-Hill, 1965. [Online]. Available: http://opac.inria.fr/record=b1080711

[23] R. Gupta, "Introduction to lattice QCD: course," in *Probing the standard model of particle interactions. Proceedings, Summer School in Theoretical Physics, NATO Advanced Study Institute, 68th session, Les Houches, France, July 28-September 5, 1997. Pt. 1, 2*, 1997, pp. 83–219. [Online]. Available: http://alice.cern.ch/format/showfull?sysnb=0284452

[24] T. DeGrand and C. E. DeTar, *Lattice methods for quantum chromodynamics*, 2006.

[25] C. B. Lang and H. Nicolai, "Monte Carlo simulation of SU(2) gauge theory with fermions on a four-dimensional lattice," *Nucl. Phys.*, vol. B200, p. 135, 1982.

[26] A. Hasenfratz, Z. Kunszt, P. Hasenfratz, and C. Lang, "Hopping parameter expansion for the meson spectrum in su(3) lattice qcd," *Physics Letters B*, vol. 110, no. 34, pp. 289 – 294, 1982. [Online]. Available: http://www.sciencedirect.com/science/article/pii/0370269382912552

[27] A. Hasenfratz, P. Hasenfratz, Z. Kunszt, and C. B. Lang, "Hopping parameter expansion for the baryons and p wave mesons," *Phys. Lett.*, vol. B117, p. 81, 1982.

[28] J. B. Kogut and L. Susskind, "Hamiltonian formulation of Wilson's lattice gauge theories," *Phys. Rev.*, vol. D11, pp. 395–408, 1975.

[29] L. Susskind, "Lattice fermions," *Phys. Rev.*, vol. D16, pp. 3031–3039, 1977.

[30] T. Banks, S. Raby, L. Susskind, J. B. Kogut, D. R. T. Jones, P. N. Scharbach, and D. K. Sinclair, "Strong coupling calculations of the hadron spectrum of quantum chromodynamics," *Phys. Rev.*, vol. D15, p. 1111, 1977.

[31] K. Symanzik, "Continuum limit and improved action in lattice theories. 1. Principles and phi**4 Theory," *Nucl. Phys.*, vol. B226, p. 187, 1983.

[32] ——, "Continuum limit and improved action in lattice theories. 2. O(N) nonlinear sigma model in perturbation theory," *Nucl. Phys.*, vol. B226, p. 205, 1983.

[33] M. Lüscher and P. Weisz, "On-shell improved lattice gauge theories," *Commun. Math. Phys.*, vol. 97, p. 59, 1985, [Erratum: Commun. Math. Phys.98,433(1985)].

[34] B. Sheikholeslami and R. Wohlert, "Improved continuum limit lattice action for QCD with Wilson fermions," *Nucl. Phys.*, vol. B259, p. 572, 1985.

[35] K. Orginos and D. Toussaint, "Testing improved actions for dynamical Kogut-Susskind quarks," *Phys. Rev.*, vol. D59, p. 014501, 1999. [Online]. Available: http://arxiv.org/abs/hep-lat/9805009

[36] J. F. Lagae and D. K. Sinclair, "Improved staggered quark actions with reduced flavor symmetry violations for lattice QCD," *Phys. Rev.*, vol. D59, p. 014511, 1999. [Online]. Available: http://arxiv.org/abs/hep-lat/9806014

[37] K. Orginos, R. Sugar, and D. Toussaint, "Improved flavor symmetry in Kogut-Susskind fermion actions," *Nucl. Phys. Proc. Suppl.*, vol. 83, pp. 878–880, 2000. [Online]. Available: http://arxiv.org/abs/hep-lat/9909087

[38] C. Bernard, T. Burch, C. E. DeTar, S. Gottlieb, L. Levkova, U. M. Heller, J. E. Hetrick, R. Sugar, and D. Toussaint, "QCD equation of state with 2+1 flavors of improved staggered quarks," *Phys. Rev.*, vol. D75, p. 094505, 2007. [Online]. Available: http://arxiv.org/abs/hep-lat/0611031

[39] E. Follana, C. Davies, A. Hart, P. Lepage, Q. Mason, and H. Trottier, "Improvement and taste symmetry breaking for staggered quarks," *Nucl. Phys. Proc. Suppl.*, vol. 129,130, pp. 384–386, 2004. [Online]. Available: http://arxiv.org/abs/hep-lat/0406021

[40] T. Blum, C. E. DeTar, S. A. Gottlieb, K. Rummukainen, U. M. Heller, J. E. Hetrick, D. Toussaint, R. L. Sugar, and M. Wingate, "Improving flavor symmetry in the Kogut-Susskind hadron spectrum," *Phys. Rev.*, vol. D55, pp. 1133–1137, 1997. [Online]. Available: http://arxiv.org/abs/hep-lat/9609036

[41] R. C. Johnson, "Angular momentum on a lattice," *Phys. Lett.*, vol. B114, p. 147, 1982.

[42] H. A. van der Vorst, "BI-CGSTAB: A fast and smoothly converging variant of bi-CG for the solution of nonsymmetric linear systems," *SIAM J. Sci. Stat. Comput.*, vol. 13, no. 2, pp. 631–644, 1992. [Online]. Available: http://dx.doi.org/10.1137/0913035

[43] P. de Forcrand, "Progress on lattice QCD algorithms," *Nucl. Phys. Proc. Suppl.*, vol. 47, pp. 228–235, 1996. [Online]. Available: http://arxiv.org/abs/hep-lat/9509082

[44] N. Metropolis, A. W. Rosenbluth, M. N. Rosenbluth, A. H. Teller, and E. Teller, "Equation of state calculations by fast computing machines," *J. Chem. Phys.*, vol. 21, pp. 1087–1092, 1953.

[45] D. J. E. Callaway and A. Rahman, "The microcanonical ensemble: a new formulation of lattice gauge theory," *Phys. Rev. Lett.*, vol. 49, p. 613, 1982.

[46] ——, "Lattice gauge theory in microcanonical ensemble," *Phys. Rev.*, vol. D28, p. 1506, 1983.

[47] M. Lüscher and U. Wolff, "How to calculate the elastic scattering matrix in two-dimensional quantum field theories by numerical simulation," *Nucl.Phys.*, vol. B339, p. 222, 1990.

[48] B. Blossier, M. Della Morte, G. von Hippel, T. Mendes, and R. Sommer, "On the generalized eigenvalue method for energies and matrix elements in lattice field theory," *JHEP*, vol. 0904, p. 094, 2009. [Online]. Available: http://arxiv.org/abs/0902.1265

[49] M. Lüscher, "Volume dependence of the energy spectrum in massive quantum field theories. 1. stable particle states," *Commun. Math. Phys.*, vol. 104, p. 177, 1986.

[50] ——, "Two particle states on a torus and their relation to the scattering matrix," *Nucl. Phys.*, vol. B354, pp. 531–578, 1991.

[51] T. Yamazaki *et al.*, "I = 2 pi pi scattering phase shift with two flavors of O(a) improved dynamical quarks," *Phys. Rev.*, vol. D70, p. 074513, 2004. [Online]. Available: http://arxiv.org/abs/hep-lat/0402025

[52] Z. Fu, "Lattice study on πK scattering with moving wall source," *Phys. Rev.*, vol. D85, p. 074501, 2012. [Online]. Available: http://arxiv.org/abs/1110.1422

[53] M. Guagnelli, E. Marinari, and G. Parisi, "Scattering lengths from fluctuations," *Phys. Lett.*, vol. B240, p. 188, 1990.

[54] S. R. Sharpe, R. Gupta, and G. W. Kilcup, "Lattice calculation of I = 2 pion scattering length," *Nucl. Phys.*, vol. B383, pp. 309–356, 1992.

[55] R. Gupta, A. Patel, and S. R. Sharpe, "I = 2 pion scattering amplitude with Wilson fermions," *Phys. Rev.*, vol. D48, pp. 388–396, 1993. [Online]. Available: http://arxiv.org/abs/hep-lat/9301016

[56] M. Fukugita, Y. Kuramashi, M. Okawa, H. Mino, and A. Ukawa, "Hadron scattering lengths in lattice QCD," *Phys. Rev.*, vol. D52, pp. 3003–3023, 1995. [Online]. Available: http://arxiv.org/abs/hep-lat/9501024

[57] S. Aoki *et al.*, "I=2 pion scattering length with the Wilson fermion," *Phys. Rev.*, vol. D66, p. 077501, 2002. [Online]. Available: http://arxiv.org/abs/hep-lat/0206011

[58] ——, "I = 2 pion scattering length with Wilson fermions," *Phys. Rev.*, vol. D67, p. 014502, 2003. [Online]. Available: http://arxiv.org/abs/hep-lat/0209124

[59] ——, "I=2 pion scattering length from two-pion wave functions," *Phys. Rev.*, vol. D71, p. 094504, 2005. [Online]. Available: http://arxiv.org/abs/hep-lat/0503025

[60] S. R. Beane, P. F. Bedaque, K. Orginos, and M. J. Savage, "I = 2 pi-pi scattering from fully-dynamical mixed-action lattice QCD," *Phys. Rev.*, vol. D73, p. 054503, 2006. [Online]. Available: http://arxiv.org/abs/hep-lat/0506013

[61] ——, "Nucleon-nucleon scattering from fully-dynamical lattice QCD," *Phys. Rev. Lett.*, vol. 97, p. 012001, 2006. [Online]. Available: http://arxiv.org/abs/hep-lat/0602010

[62] S. R. Beane, P. F. Bedaque, T. C. Luu, K. Orginos, E. Pallante, A. Parreno, and M. J. Savage, "pi K scattering in full QCD with domain-wall valence quarks," *Phys. Rev.*, vol. D74, p. 114503, 2006. [Online]. Available: http://arxiv.org/abs/hep-lat/0607036

[63] C. Liu, J.-h. Zhang, Y. Chen, and J. P. Ma, "Calculating the I = 2 pion scattering length using tadpole improved clover Wilson action on coarse anisotropic lattices," *Nucl. Phys.*, vol. B624, pp. 360–376, 2002. [Online]. Available: http://arxiv.org/abs/hep-lat/0109020

[64] C. Miao, X.-i. Du, G.-w. Meng, and C. Liu, "Lattice study on kaon pion scattering length in the I = 3/2 channel," *Phys. Lett.*, vol. B595, pp. 400–407, 2004. [Online]. Available: http://arxiv.org/abs/hep-lat/0403028

[65] G.-w. Meng, C. Miao, X.-n. Du, and C. Liu, "Lattice study on kaon nucleon scattering length in the I = 1 channel," *Int. J. Mod. Phys.*, vol. A19, pp. 4401–4412, 2004. [Online]. Available: http://arxiv.org/abs/hep-lat/0309048

[66] P. Hasenfratz, K. J. Juge, and F. Niedermayer, "New results on cut-off effects in spectroscopy with the fixed point action," *JHEP*, vol. 12, p. 030, 2004. [Online]. Available: http://arxiv.org/abs/hep-lat/0411034

[67] K. Yokokawa, S. Sasaki, T. Hatsuda, and A. Hayashigaki, "First lattice study of low-energy charmonium-hadron interaction," *Phys. Rev.*, vol. D74, p. 034504, 2006. [Online]. Available: http://arxiv.org/abs/hep-lat/0605009

[68] J. J. Dudek, R. G. Edwards, M. J. Peardon, D. G. Richards, and C. E. Thomas, "The phase-shift of isospin-2 pi-pi scattering from lattice QCD," *Phys. Rev.*, vol. D83, p. 071504, 2011. [Online]. Available: http://arxiv.org/abs/1011.6352

[69] J. J. Dudek, R. G. Edwards, and C. E. Thomas, "S and D-wave phase shifts in isospin-2 pi pi scattering from lattice QCD," *Phys. Rev.*, vol. D86, p. 034031, 2012. [Online]. Available: http://arxiv.org/abs/1203.6041

[70] D. Mohler, S. Prelovsek, and R. M. Woloshyn, "$D\pi$ scattering and D meson resonances from lattice QCD," *Phys. Rev.*, vol. D87, no. 3, p. 034501, 2013. [Online]. Available: http://arxiv.org/abs/1208.4059

[71] S. Prelovsek, L. Leskovec, C. B. Lang, and D. Mohler, "K π scattering and the K* decay width from lattice QCD," *Phys. Rev.*, vol. D88, no. 5, p. 054508, 2013. [Online]. Available: http://arxiv.org/abs/1307.0736

[72] D. Mohler, C. B. Lang, L. Leskovec, S. Prelovsek, and R. M. Woloshyn, "$D^*_{s0}(2317)$ meson and D-meson-kaon scattering from lattice QCD," *Phys. Rev. Lett.*, vol. 111, no. 22, p. 222001, 2013. [Online]. Available: http://arxiv.org/abs/1308.3175

[73] D. J. Wilson, J. J. Dudek, R. G. Edwards, and C. E. Thomas, "Resonances in coupled $\pi K, \eta K$ scattering from lattice QCD," *Phys. Rev.*, vol. D91, no. 5, p. 054008, 2015. [Online]. Available: http://arxiv.org/abs/1411.2004

[74] S. Prelovsek and L. Leskovec, "Evidence for X(3872) from DD* scattering on the lattice," *Phys. Rev. Lett.*, vol. 111, p. 192001, 2013. [Online]. Available: http://arxiv.org/abs/1307.5172

[75] S.-h. Lee, C. DeTar, H. Na, and D. Mohler, "Searching for the $X(3872)$ and $Z_c^+(3900)$ on HISQ lattices," 2014. [Online]. Available: http://arxiv.org/abs/1411.1389

[76] C. DeTar, A. S. Kronfeld, S.-H. Lee, L. Levkova, D. Mohler, and J. N. Simone, "Charmonium mass splittings at the physical point," *PoS*, vol. LATTICE2012, p. 257, 2012. [Online]. Available: http://arxiv.org/abs/1211.2253

[77] J. L. Richardson, "The heavy quark potential and the upsilon, J/psi systems," *Phys. Lett.*, vol. B82, p. 272, 1979.

[78] E. Eichten, K. Gottfried, T. Kinoshita, K. D. Lane, and T.-M. Yan, "Charmonium: comparison with experiment," *Phys. Rev.*, vol. D21, p. 203, 1980.

[79] H. Leutwyler, "How to use heavy quarks to probe the QCD vacuum," *Phys. Lett.*, vol. B98, p. 447, 1981.

[80] V. B. Berestetskii, E. M. Lifshitz, and L. P. Pitaevskii, *Quantum electrodynamics*, ser. Course of Theoretical Physics. Oxford: Pergamon Press, 1982, vol. 4. [Online]. Available: http://www-spires.fnal.gov/spires/find/books/www?cl=QC680.B42

[81] E. Eichten and F. Feinberg, "Spin dependent forces in QCD," *Phys. Rev.*, vol. D23, p. 2724, 1981.

[82] N. Brambilla, A. Pineda, J. Soto, and A. Vairo, "Effective field theories for heavy quarkonium," *Rev. Mod. Phys.*, vol. 77, p. 1423, 2005. [Online]. Available: http://arxiv.org/abs/hep-ph/0410047

[83] T. Barnes, S. Godfrey, and E. S. Swanson, "Higher charmonia," *Phys. Rev.*, vol. D72, p. 054026, 2005. [Online]. Available: http://arxiv.org/abs/hep-ph/0505002

[84] J. J. Dudek, R. G. Edwards, M. J. Peardon, D. G. Richards, and C. E. Thomas, "Toward the excited meson spectrum of dynamical QCD," *Phys. Rev.*, vol. D82, p. 034508, 2010. [Online]. Available: http://arxiv.org/abs/1004.4930

[85] A. Bazavov *et al.*, "Nonperturbative QCD simulations with 2+1 flavors of improved staggered quarks," *Rev. Mod. Phys.*, vol. 82, pp. 1349–1417, 2010. [Online]. Available: http://arxiv.org/abs/0903.3598

[86] A. X. El-Khadra, A. S. Kronfeld, and P. B. Mackenzie, "Massive fermions in lattice gauge theory," *Phys. Rev.*, vol. D55, pp. 3933–3957, 1997. [Online]. Available: http://arxiv.org/abs/hep-lat/9604004

[87] T. Burch, C. Hagen, M. Hetzenegger, and A. Schafer, "Low and high spin mesons from N(f) = 2 Clover-Wilson lattices," *Phys. Rev.*, vol. D79, p. 114503, 2009. [Online]. Available: http://arxiv.org/abs/0903.2358

[88] R. G. Petry, D. Harnett, R. Lewis, and R. M. Woloshyn, "Exploring the meson spectrum with twisted mass lattice QCD," *Phys. Rev.*, vol. D78, p. 074502, 2008. [Online]. Available: http://arxiv.org/abs/0803.4141

[89] C. Gattringer, L. Ya. Glozman, C. B. Lang, D. Mohler, and S. Prelovsek, "Derivative sources in lattice spectroscopy of excited mesons," *Phys. Rev.*, vol. D78, p. 034501, 2008. [Online]. Available: http://arxiv.org/abs/0802.2020

[90] T. Burch, C. Gattringer, L. Ya. Glozman, R. Kleindl, C. B. Lang, and A. Schaefer, "Spatially improved operators for excited hadrons on the lattice," *Phys. Rev.*, vol. D70, p. 054502, 2004. [Online]. Available: http://arxiv.org/abs/hep-lat/0405006

[91] P. Lacock, C. Michael, P. Boyle, and P. Rowland, "Orbitally excited and hybrid mesons from the lattice," *Phys. Rev.*, vol. D54, pp. 6997–7009, 1996. [Online]. Available: http://arxiv.org/abs/hep-lat/9605025

[92] J. J. Dudek, R. G. Edwards, N. Mathur, and D. G. Richards, "Charmonium excited state spectrum in lattice QCD," *Phys. Rev.*, vol. D77, p. 034501, 2008. [Online]. Available: http://arxiv.org/abs/0707.4162

[93] M. Albanese *et al.*, "Glueball masses and string tension in lattice QCD," *Phys. Lett.*, vol. B192, pp. 163–169, 1987.

[94] M. E. Peskin, "Aspects of the dynamics of heavy quark systems," in *Dynamics and spectroscopy at high-energy: Proceedings, 11th SLAC summer institute on particle physics (SSI 83), Stanford, Calif., 18-29 Jul 1983*, 1983. [Online]. Available: http://www-public.slac.stanford.edu/sciDoc/docMeta.aspx?slacPubNumber=SLAC-PUB-3273

[95] T. Burch, C. DeTar, M. Di Pierro, A. X. El-Khadra, E. D. Freeland, S. Gottlieb, A. S. Kronfeld, L. Levkova, P. B. Mackenzie, and J. N. Simone, "Quarkonium mass splittings in three-flavor lattice QCD," *Phys. Rev.*, vol. D81, p. 034508, 2010. [Online]. Available: http://arxiv.org/abs/0912.2701

[96] U. Wolff, "Monte Carlo errors with less errors," *Comput. Phys. Commun.*, vol. 156, pp. 143–153, 2004, [Erratum: Comput. Phys. Commun.176,383(2007)]. [Online]. Available: http://arxiv.org/abs/hep-lat/0306017

[97] C. DeTar and S.-H. Lee, "Variational method with staggered fermions," *Phys. Rev.*, vol. D91, no. 3, p. 034504, 2015. [Online]. Available: http://arxiv.org/abs/1411.4676

[98] D. Mohler and R. M. Woloshyn, "D and D_s meson spectroscopy," *Phys.Rev.*, vol. D84, p. 054505, 2011. [Online]. Available: http://arxiv.org/abs/1103.5506

[99] G. Bali, S. Collins, S. Durr, Z. Fodor, R. Horsley, C. Hoelbling, S. D. Katz, I. Kanamori, S. Krieg, T. Kurth, L. Lellouch, T. Lippert, C. McNeile, Y. Nakamura, D. Pleiter, P. Perez-Rubio, P. Rakowh, A. Schafer, G. Schierholz, K. K. Szabo, F. Winter, and J. Zanotti, "Spectra of heavy-light and heavy-heavy mesons containing charm quarks, including higher spin states for N_f=2+1," *PoS LATTICE2011*, 2011. [Online]. Available: http://arxiv.org/abs/1108.6147

[100] G. Bali, S. Collins, and P. Perez-Rubio, "Charmed hadron spectroscopy on the lattice for $N_f = 2 + 1$ flavours," *J.Phys.Conf.Ser.*, vol. 426, p. 012017, 2013. [Online]. Available: http://arxiv.org/abs/1212.0565

[101] G. Moir, M. Peardon, S. M. Ryan, C. E. Thomas, and L. Liu, "Excited spectroscopy of charmed mesons from lattice QCD," *JHEP*, vol. 05, p. 021, 2013. [Online]. Available: http://arxiv.org/abs/1301.7670

[102] D. Mohler, C. B. Lang, L. Leskovec, S. Prelovsek, and R. M. Woloshyn, "$D^*_{s0}(2317)$ meson and D-meson-kaon scattering from lattice QCD," *Phys.Rev.Lett.*, vol. 111, p. 222001, 2013. [Online]. Available: http://arxiv.org/abs/1308.3175v3

[103] A. Bazavov *et al.*, "Charmed and light pseudoscalar meson decay constants from four-flavor lattice QCD with physical light quarks," *Phys. Rev.*, vol. D90, no. 7, p. 074509, 2014. [Online]. Available: http://arxiv.org/abs/1407.3772

[104] ——, "Lattice QCD ensembles with four flavors of highly improved staggered quarks," *Phys. Rev.*, vol. D87, no. 5, p. 054505, 2013. [Online]. Available: http://arxiv.org/abs/1212.4768

[105] R. L. Jaffe, "Multiquark hadrons. 1. The phenomenology of (2 quark 2 anti-quark) mesons," *Phys. Rev.*, vol. D15, p. 267, 1977.

[106] S. Choi *et al.*, "Observation of a narrow charmonium - like state in exclusive B+- —¿ K+- pi+ pi- J / psi decays," *Phys.Rev.Lett.*, vol. 91, p. 262001, 2003. [Online]. Available: http://arxiv.org/abs/hep-ex/0309032

[107] I. Adachi *et al.*, "Study of $X(3872)$ in B meson decays," 2008. [Online]. Available: http://arxiv.org/abs/0809.1224

[108] D. Acosta *et al.*, "Observation of the narrow state $X(3872) \to J/\psi\pi^+\pi^-$ in $\bar{p}p$ collisions at $\sqrt{s} = 1.96$ TeV," *Phys.Rev.Lett.*, vol. 93, p. 072001, 2004. [Online]. Available: http://arxiv.org/abs/hep-ex/0312021

[109] T. Aaltonen *et al.*, "Precision measurement of the $X(3872)$ mass in $J/\psi\pi^+\pi^-$ decays," *Phys.Rev.Lett.*, vol. 103, p. 152001, 2009. [Online]. Available: http://arxiv.org/abs/0906.5218

[110] V. Abazov *et al.*, "Observation and properties of the $X(3872)$ decaying to $J/\psi\pi^+\pi^-$ in $p\bar{p}$ collisions at $\sqrt{s} = 1.96$ TeV," *Phys.Rev.Lett.*, vol. 93, p. 162002, 2004. [Online]. Available: http://arxiv.org/abs/hep-ex/0405004

[111] B. Aubert *et al.*, "Study of the $B \to J/\psi K^-\pi^+\pi^-$ decay and measurement of the $B \to X(3872)K^-$ branching fraction," *Phys.Rev.*, vol. D71, p. 071103, 2005. [Online]. Available: http://arxiv.org/abs/hep-ex/0406022

[112] ——, "A study of $B \to X(3872)K$, with $X_{3872} \to J/\Psi\pi^+\pi^-$," *Phys.Rev.*, vol. D77, p. 111101, 2008. [Online]. Available: http://arxiv.org/abs/0803.2838

[113] R. Aaij *et al.*, "Observation of $X(3872)$ production in pp collisions at $\sqrt{s} = 7$ TeV," *Eur.Phys.J.*, vol. C72, p. 1972, 2012. [Online]. Available: http://arxiv.org/abs/1112.5310

[114] ——, "Determination of the X(3872) meson quantum numbers," *Phys.Rev.Lett.*, vol. 110, p. 222001, 2013. [Online]. Available: http://arxiv.org/abs/1302.6269

[115] T. Aaltonen *et al.*, "Evidence for a narrow near-threshold structure in the $J/\psi\phi$ mass spectrum in $B^+ \to J/\psi\phi K^+$ decays," *Phys. Rev. Lett.*, vol. 102, p. 242002, 2009. [Online]. Available: http://arxiv.org/abs/0903.2229

[116] S. Chatrchyan *et al.*, "Observation of a peaking structure in the $J/\psi\phi$ mass spectrum from $B^{\pm} \to J/\psi\phi K^{\pm}$ decays," *Phys. Lett.*, vol. B734, pp. 261–281, 2014. [Online]. Available: http://arxiv.org/abs/1309.6920

[117] V. M. Abazov *et al.*, "Search for the $X(4140)$ state in $B^{+} \to J/\psi\phi K^{+}$ decays with the D0 detector," *Phys. Rev.*, vol. D89, no. 1, p. 012004, 2014. [Online]. Available: http://arxiv.org/abs/1309.6580

[118] J. P. Lees *et al.*, "Study of $B^{\pm,0} \to J/\psi K^{+}K^{-}K^{\pm,0}$ and search for $B^{0} \to J/\psi\phi$ at BABAR," *Phys. Rev.*, vol. D91, no. 1, p. 012003, 2015. [Online]. Available: http://arxiv.org/abs/1407.7244

[119] M. Ablikim *et al.*, "Observation of a charged charmoniumlike structure in $e^{+}e^{-}$ to $\pi^{+}\pi^{-}$ J/ψ at $\sqrt{s} = 4.26$GeV," *Phys.Rev.Lett.*, vol. 110, p. 252001, 2013. [Online]. Available: http://arxiv.org/abs/1303.5949

[120] Z. Liu *et al.*, "Study of $e^{+}e^{-} \to \pi^{+}\pi^{-}J/\psi$ and observation of a charged charmoniumlike state at Belle," *Phys.Rev.Lett.*, vol. 110, p. 252002, 2013. [Online]. Available: http://arxiv.org/abs/1304.0121

[121] T. Xiao, S. Dobbs, A. Tomaradze, and K. K. Seth, "Observation of the charged hadron $Z_c^{\pm}(3900)$ and evidence for the neutral $Z_c^{0}(3900)$ in $e^{+}e^{-} \to \pi\pi J/\psi$ at $\sqrt{s} = 4170$ MeV," *Phys.Lett.*, vol. B727, pp. 366–370, 2013. [Online]. Available: http://arxiv.org/abs/1304.3036

[122] C. Adolph *et al.*, "Search for exclusive photoproduction of $\mathrm{Z}_c^{\pm}(3900)$ at COMPASS," *Phys.Lett.*, vol. B742, pp. 330–334, 2015. [Online]. Available: http://arxiv.org/abs/1407.6186

[123] K. Chilikin *et al.*, "Observation of a new charged charmoniumlike state in $\bar{B}^{0}J/\psi K^{-}K^{+}$ decays," *Phys.Rev.*, vol. D90, no. 11, p. 112009, 2014. [Online]. Available: http://arxiv.org/abs/1408.6457

[124] R. Aaij *et al.*, "Measurement of the resonant and CP components in $\overline{B}^{0} \to J/\psi\pi^{+}\pi^{-}$ decays," *Phys.Rev.*, vol. D90, no. 1, p. 012003, 2014. [Online]. Available: http://arxiv.org/abs/1404.5673

[125] A. Bazavov *et al.*, "Scaling studies of QCD with the dynamical HISQ action," *Phys. Rev.*, vol. D82, p. 074501, 2010. [Online]. Available: http://arxiv.org/abs/1004.0342

[126] C. Bernard *et al.*, "Tuning Fermilab heavy quarks in 2+1 flavor lattice QCD with application to hyperfine splittings," *Phys. Rev.*, vol. D83, p. 034503, 2011. [Online]. Available: http://arxiv.org/abs/1003.1937

[127] C. W. Bernard, T. A. DeGrand, C. E. DeTar, P. Lacock, S. A. Gottlieb, U. M. Heller, J. Hetrick, K. Orginos, D. Toussaint, and R. L. Sugar, "Zero temperature string breaking in lattice quantum chromodynamics," *Phys. Rev.*, vol. D64, p. 074509, 2001. [Online]. Available: http://arxiv.org/abs/hep-lat/0103012

[128] G. S. Bali, H. Neff, T. Duessel, T. Lippert, and K. Schilling, "Observation of string breaking in QCD," *Phys. Rev.*, vol. D71, p. 114513, 2005. [Online]. Available: http://arxiv.org/abs/hep-lat/0505012

[129] Landau, L.D. and Lifshits, E.M., *Quantum mechanics: non-relativistic theory*, ser. Butterworth Heinemann. Butterworth-Heinemann, 1977. [Online]. Available: https://books.google.com/books?id=J9ui6KwC4mMC

[130] E. Braaten, "Effective field theories for the X(3872)," *PoS*, vol. EFT09, p. 065, 2009.

[131] T. Yamazaki, Y. Kuramashi, and A. Ukawa, "Two-nucleon bound states in quenched lattice QCD," *Phys. Rev.*, vol. D84, p. 054506, 2011. [Online]. Available: http://arxiv.org/abs/1105.1418

[132] S. R. Beane *et al.*, "Nucleon-nucleon scattering parameters in the limit of SU(3) flavor symmetry," *Phys. Rev.*, vol. C88, no. 2, p. 024003, 2013. [Online]. Available: http://arxiv.org/abs/1301.5790

[133] M. Padmanath, C. B. Lang, and S. Prelovsek, "X(3872) and Y(4140) using diquark-antidiquark operators with lattice QCD," *Phys. Rev.*, vol. D92, no. 3, p. 034501, 2015. [Online]. Available: http://arxiv.org/abs/1503.03257

[134] S. Sasaki and T. Yamazaki, "Signatures of S-wave bound-state formation in finite volume," *Phys. Rev.*, vol. D74, p. 114507, 2006. [Online]. Available: http://arxiv.org/abs/hep-lat/0610081